DESIGN OF SOLID OXIDE FUEL CELL–MOLTEN CARBONATE FUEL CELL COMBINED SYSTEM FOR POWER GENERATION AND CARBON DIOXIDE EMISSION REDUCTION

Mr. Prathak Jienkulsawad

จุฬาลงกรณ์มหาวิทยาลัย
CHULALONGKORN UNIVERSITY

A Dissertation Submitted in Partial Fulfillment of the Requirements
for the Degree of Doctor of Engineering in Chemical Engineering
Department of Chemical Engineering
Faculty of Engineering
Chulalongkorn University
Academic Year 2018
Copyright of Chulalongkorn University

การออกแบบระบบร่วมระหว่างเซลล์เชื้อเพลิงชนิดออกไซด์แข็งและเซลล์เชื้อเพลิงชนิดคาร์บอเนต
หลวเพื่อการผลิตไฟฟ้าและลดการปล่อยคาร์บอนไดออกไซด์

นายประทักษ์ เจียรกุลสวัสดิ์

Thesis Title	DESIGN OF SOLID OXIDE FUEL CELL–MOLTEN CARBONATE FUEL CELL COMBINED SYSTEM FOR POWER GENERATION AND CARBON DIOXIDE EMISSION REDUCTION
By	Mr. Prathak Jienkulsawad
Field of Study	Chemical Engineering
Thesis Advisor	Assistant Professor Amornchai Arpornwichanop, D.Eng.

Accepted by the Faculty of Engineering, Chulalongkorn University in Partial Fulfillment of the Requirement for the Doctor of Engineering

.... Dean of the Faculty of Engineering
(Associate Professor Supot Teachavorasinskun, D.Eng.)

DISSERTATION COMMITTEE

.... Chairman
(Professor Sarawut Rimdusit, Ph.D.)

.... Thesis Advisor
(Assistant Professor Amornchai Arpornwichanop, D.Eng.)

.... Examiner
(Associate Professor Kasidit Nootong, Ph.D.)

.... Examiner
(Assistant Professor Apinan Soottitantawat, D.Eng.)

.... External Examiner
(Assistant Professor Yaneeporn Patcharavorachot, D.Eng.)

จุฬาลงกรณ์มหาวิทยาลัย

CHULALONGKORN UNIVERSITY

iii

ประทักษ์ เจียรกุลสวัสดิ์ :

การออกแบบระบบร่วมระหว่างเซลล์เชื้อเพลิงชนิดออกไซด์แข็งและเซลล์เชื้อเพลิงชนิดคาร์บอเนตเหลวเพื่อการผลิตไฟฟ้าและลดการปล่อยคาร์บอนไดออกไซด์. (DESIGN OF SOLID OXIDE FUEL CELL–MOLTEN CARBONATE FUEL CELL COMBINED SYSTEM FOR POWER GENERATION AND CARBON DIOXIDE EMISSION REDUCTION) อ.ที่ปรึกษาหลัก : ผศ. ดร.อมรชัย อาภรณ์วิชานพ

งานวิจัยนี้นำเสนอการออกแบบและวิเคราะห์เชิงสมรรถนะของระบบร่วมระหว่างเซลล์เชื้อเพลิงชนิดออกไซด์แข็งและเซลล์เชื้อเพลิงชนิดคาร์บอเนตหลอมเหลวที่ใช้มีเทนเป็นเชื้อเพลิง เนื่องจาก เซลล์เชื้อเพลิงชนิดออกไซด์แข็งไม่สามารถใช้เชื้อเพลิงได้หมด ดังนั้น จึงมีเชื้อเพลิงเหลือออกจากระบบและแก๊สที่ออกจากเซลล์เชื้อเพลิงชนิดออกไซด์แข็งสามารถป้อนเข้าเซลล์เชื้อเพลิงชนิดคาร์บอเนตหลอมเหลวได้โดยตรงระบบร่วมดังกล่าวให้ประสิทธิภาพทางไฟฟ้า 55.22% ซึ่งมากกว่าระบบเซลล์เชื้อเพลิงเดี่ยวๆ การใช้เชื้อเพลิงของทั้งสองเซลล์, อุณหภูมิของเซลล์เชื้อเพลิงชนิดออกไซด์แข็งส่งผลต่อสมรรถนะของระบบร่วมอย่างมาก ขั้นตอนต่อไปโครงสร้างสี่โครงสร้างถูกนำเสนอเพื่อทดสอบและเปรียบเทียบสมรรถนะของระบบร่วมในเชิงของการผลิตไฟฟ้าที่ได้, การใช้คาร์บอนไดออกไซด์, ภาระทางความร้อน และโอกาสเกิดนิกเกิลออกไซด์เพื่อหาโครงสร้างที่เหมาะสมสำหรับระบบร่วมดังกล่าว พบว่าโครงสร้างแบบซีรีย์ (ข) เหมาะสมที่สุดกับการพัฒนาการผลิตไฟฟ้าโดยไม่พบนิกเกิลออกไซด์

อย่างไรก็ตามกลยุทธ์ในการควบคุมระบบนั้นจำเป็นต้องพิจารณาเพื่อดำเนินการให้มีประสิทธิภาพ การออกแบบโครงสร้างตัวควบคุมถูกดำเนินการภายใต้การออปติไมเซชันเชิงเศรษฐศาสตร์เพื่อเลือกตัวแปรปรับ, ตัวแปรควบคุม และโครงสร้างตัวควบคุม ฟังก์ชันวัตถุประสงค์ (ค่าใช้จ่าย) นั้นพิจารณาค่าภาษีในปล่อยคาร์บอนไดออกไซด์ออกจากระบบเพื่อใช้ในถ่วงน้ำหนักระหว่างการผลิตไฟฟ้าและการปล่อยคาร์บอนไดออกไซด์ และอยู่ภายใต้การดำเนินการที่ปลอดภัย การวิเคราะห์ความสามารถในการควบคุมด้วยค่ารีเลทีฟเกนอาเรย์ถูกนำมาใช้เพื่อเลือกคู่ตัวแปรปรับตัวแปรควบคุม และควบคุมระบบด้วยตัวควบคุมพีไอดี

เนื่องจากความต้องการไฟฟ้าสามารถแผรผันและคาดการไม่ได้ ดังนั้น มีความจำเป็นที่จะต้องดำเนินงานร่วมกับระบบเก็บพลังงานระบบกังหันแก๊สและระบบเก็บพลังงานแบบอัดอากาศถูกเอามาใช้ในการทำงานร่วมกับระบบเซลล์เชื้อเพลิง เพื่อเพิ่มความยืดหยุ่นของระบบ พบว่าการใช้กังหันแก๊สและระบบเก็บพลังงานแบบอัดอากาศร่วมกับระบบร่วมเซลล์เชื้อเพลิงสามารถทำให้ระบบจัดการกับความผันผวนของความต้องการไฟฟ้าได้

สาขาวิชา	วิศวกรรมเคมี	ลายมือชื่อนิสิต ....
ปีการศึกษา	2561	ลายมือชื่อ อ.ที่ปรึกษาหลัก ....

5471417521 : MAJOR CHEMICAL ENGINEERING

KEYWORD: CONTROL STRUCTURE DESIGN, SOLID OXIDE FUEL CELL, MOLTEN CARBONATE FUEL CELL, GAS TURBINE, COMPRESSED AIR ENERGY STORAGE, INTEGRATED SYSTEM

Prathak Jienkulsawad : DESIGN OF SOLID OXIDE FUEL CELL–MOLTEN CARBONATE FUEL CELL COMBINED SYSTEM FOR POWER GENERATION AND CARBON DIOXIDE EMISSION REDUCTION. Advisor: Asst. Prof. Amornchai Arpornwichanop, D.Eng.

This research concentrates on the design and performance analysis of a solid oxide fuel cell (SOFC) and a molten carbonate fuel cell (MCFC) integrated system with using methane as fuel. Because SOFCs cannot completely use their fuel, there is remaining fuel leaving the system. In addition, the exhaust gas from an SOFC can be directly fed into an MCFC. The integrated fuel cell system shows an electrical efficiency of 55.22%, which is higher than a single fuel cell system. Fuel utilization of both fuel cells, SOFC temperature dramatically affect the performance of the integrated system. Four configurations were next proposed to be investigated and compared the performance in terms of power generation, CO_2 utilization, heat duty and NiO formation to determine the suitable design of the integrated fuel cell system. The results showed that system (B) is suitable for power generation improvement consideration with no NiO formation possibility found.

However, the control strategy of such a system needs to be considered for the efficient operation. A control structure design is performed based on economic optimization to select manipulated variables, controlled variables and control loop configurations. The objective (cost) function includes a carbon tax to get an optimal trade-off between power generation and carbon dioxide emission, and constraints include safe operation. The relative gain array (RGA) is applied to select input-output pairings. PID controllers are implemented to control the integrated system.

As electricity demand can vary considerably and unpredictably, it is necessary to integrate energy storage with power generation systems. The gas turbine (GT) and advanced adiabatic compressed air energy storage (AA-CAES) system are implemented into the integrated fuel cell system to enhance the system flexibility. The results showed that the implementation of the GT and AA-CAES into the integrated fuel cell system allows the system to cope with the variations in power demand.

Field of Study:	Chemical Engineering	Student's Signature
		....
Academic Year:	2018	Advisor's Signature
		....

ACKNOWLEDGEMENTS

Prathak Jienkulsawad

TABLE OF CONTENTS

จุฬาลงกรณ์มหาวิทยาลัย

CHULALONGKORN UNIVERSITY

LIST OF TABLES

จุฬาลงกรณ์มหาวิทยาลัย

CHULALONGKORN UNIVERSITY

LIST OF FIGURES

จุฬาลงกรณ์มหาวิทยาลัย
CHULALONGKORN UNIVERSITY

CHAPTER 1
INTRODUCTION

1.1   Research background and motivation

Fuel cells are the electrochemical device that can convert the chemical energy of a fuel directly to electrical energy. The attractive features of fuel cells include no moving parts, quiet operation, low pollution and high efficiency. In general, fuel cells are classified primarily by the type of electrolyte corresponding to their operating temperature range (Adamson, 2007). Among the currently available fuel cell technologies, the solid oxide fuel cell (SOFC) is the most advanced and efficient power generation. SOFC is generally operated over a wide temperature range from 1073–1273 K, which leads to a high energy conversion efficiency, the flexibility of using various fuel types and the prospect for combined heat and power systems. However, the high-temperature operation causes some difficulties, such as the requirement for high performance of materials, sealing problems caused by thermal expansion, high manufacturing cost and difficulties in thermal management (Yang et al., 2009).

The structure of SOFC consists of a dense ceramic electrolyte sandwiched by porous anode and cathode and an interconnect. Due to none liquid components, the SOFC can be fabricated into various shapes. The planar type of SOFC has been received much attention due to its compactness, high power density (short current path making low-internal electrical resistances) and ease of mass production (Hu et al., 2008). The most important design feature of the planar SOFC relates to gas flow configurations: co-flow, counter-flow and cross-flow. The co-flow configuration gives a uniform current density distribution among the three flow configurations (Hu et al., 2008). In addition, it provides more efficiency than counter-flow for indirect internal reforming (Aguiar et al., 2002). SOFC can also be designed either with electrolyte support or electrode support (Xin et al., 2006). The Ni/YSZ anode support is capable of achieving very high-power density with a wide range of operating current density than other supports (Patcharavorachot et al., 2008; Singhal, 2002).

Since SOFC is operated at high temperatures, various types of fuel, such as methane, methanol, ethanol and other hydrocarbons, can be directly used on the anode to replace pure hydrogen which is expensive and difficult to store (Baldinelli et al., 2016; Doyle et al., 2014; Saebea et al., 2013). As methane can be easily obtained during many production processes, such as petrochemical, refining and fermentation processes, it is widely used as a fuel for HTFCs (Martín and Davis, 2015; Mustapha et al., 2017; Yang et al., 2017). The methods for converting hydrocarbon fuels into a hydrogen-rich gas are steam reforming, partial oxidation and autothermal processes. Steam reforming process is an interesting strategy because this reaction can produce the highest H_2 yield and cleanest exhaust (O'Hayre et al., 2009). The steam reforming of fuel can be carried out in an external reformer or directly within the SOFC stack (internal reforming). For an internal reforming SOFC (IR-SOFC), the total heat produced in the fuel cell can be used for the endothermic steam reforming reaction, eliminating the requirement of a separate fuel reformer. This leads to a more attractive and efficient SOFC system design (Aguiar et al., 2002). In general, the internal reforming within a fuel cell can be divided into an indirect or integrated (IIR) and a direct (DIR) internal reforming. In the first approach, the reformer section is separated but adjacent to the fuel cell anode and in close thermal contact with it. In the latter, the reforming takes place directly on the anode and the fuel are supplied directly into the cell. One advantage of IIR is much easier to design the SOFC system and to develop dispersed catalysts which do not promote carbon deposition on the nickel anode. However, the conversion of methane to hydrogen is not promoted to the same extent as with direct internal reforming which hydrogen is consumed by electrochemical reaction. For the DIR configuration, part of the steam required for the reforming reaction can be obtained from the fuel cell electrochemical oxidation of hydrogen and, because of the continuing hydrogen consumption, the equilibrium of the reforming reaction may be further shifted to the product side, increasing the methane conversion and leading to a more evenly distributed a load of hydrogen (Aguiar et al., 2002). However, carbon deposition on the anode and subsequent electrocatalyst deactivation can be found in DIR-SOFC, leading to loss of cell performance and poor durability. To avoid this problem, the DIR cell operation requires a large amount of steam in addition to the fuel (Laurencin et al., 2008; Yang

et al., 2009). However, the power density is decreasing while steam content is increasing because of dilution in fuel channel (Janardhanan et al., 2007). A partial reforming of fuels called external pre-reformer can be used to avoid these problems (Adams II et al., 2013; Arpornwichanop et al., 2010; Cocco and Tola, 2009a).

When more hydrogen is consumed by the electrochemical reactions, the fuel stream at the SOFC fuel channel is diluted by steam. A hydrogen deficiency causes a larger buildup of nickel oxide at the anode, a process that leads to long-term cell degradation (Nehter, 2007; Parhizkar and Roshandel, 2017). Hence, SOFC operated in moderate fuel utilization is reasonable (commonly 60−80%). Therefore, the exhaust gas from the anode of SOFC is still valuable because of remaining fuels, such as hydrogen and carbon monoxide. Therefore, SOFCs should be integrated with other systems so that the fuel remaining in the anode as off-gas can also be utilized.

In general, the exhaust gas from the anode and cathode are mixed and burnt in an afterburner to generate heat that is required for upstream preheating and/or steam generation (Zhang et al., 2017). The second way to improve the performance is the use of exhaust gas recycling like many typical chemical processes; with this approach, anode and/or cathode off-gases are recycled. These methods can eliminate or reduce the needed external steam and improve excess heat recovery (Zhang et al., 2017). The electrical and thermal efficiencies are mainly influenced by fuel utilization and anode off-gas recirculation ratio. The high fuel utilization and recirculation ratio are needed to avoid carbon formation; however, higher values of fuel utilization and recirculation ratio can also decrease the electrical efficiency (Peters et al., 2013). The hybrid system, which is the SOFC in conjunction with a gas turbine (SOFC-GT), is used to improve the electrical efficiency because an additional gas turbine cycle produces more electricity. Another benefit of the hybrid system is the elimination of parasitic electric loads on the power system from cathode air blower requirements. This method can be achieved at higher efficiency using a gas turbine than a bottoming steam cycle (McLarty et al., 2014). However, the efficiency of the fuel cell is theoretically higher than that of the combustion engine or gas turbine. Several researchers have investigated the integration of the SOFC and other fuel cell types. For the SOFC integrated with low-temperature fuel cells, such as a polymer electrolyte membrane fuel cell (PEMFC), a hydrogen-rich fuel feed with low

temperatures, an additional water-gas-shift reactor and large heat exchanger units are required (Dicks et al., 2000). However, for the SOFC integrated with high-temperature fuel cells, use of the water-gas-shift reactor and a large heat exchanger network may not be necessary, leading to a lower cost of construction. The high-temperature fuel cells include SOFC and molten carbonate fuel cell (MCFC). The integration of several SOFC units called a multi-staged fuel cell system can improve the performance of the system as well (Araki et al., 2006; Musa and De Paepe, 2008; Patcharavorachot et al., 2010). When considering the use of MCFC in the SOFC system, a source of carbon dioxide is required to run the MCFC. This could be a potential solution to mitigating the emissions of carbon dioxide Carter and Wing (2013) also stated that *"the MCFC could potentially mitigate the emissions of fossil-fuelled power plant"*. In addition, the MCFC also has some advantages over the SOFC: (1) the MCFC operating temperature is around 650 ℃, which is suitable for internal reforming and exploiting of useable heat, (2) due to liquid electrolyte of MCFC, low contact resistance and gas seal are easy to achieve in contrast to the SOFC and (3) technology of MCFC is more advanced than IT-SOFC (Tomczyk, 2006). Moreover, McPhail et al. (2011) had shown the opportunity for integrating SOFC with MCFC by analyzing overlapping aspects regarding materials, operating conditions and applications. Thus, the integrated SOFC with MCFC is interesting. There are a few researches that use the concept of integrated SOFC with MCFC by merging the electrolyte of SOFC and MCFC for direct carbon fuel cell technologies (Chien and Irvine, 2013; Nabae et al., 2008). However, that possibility looks into new fuel cell concepts and requires a long time to successfully synthesize a composite electrolyte. Thus, the integrated system proposed in this study uses the integrated idea to increase the overall performance and utilize the remaining fuel from the SOFC.

In this research, the performance of the SOFC and MCFC integrated system is studied and compared to a single SOFC and MCFC for each operating condition. As the configuration of the SOFC-MCFC integrated system is also important and affects the system performance. In addition, the performance of such an integrated fuel cell system with different configurations with and without feed separation and exhaust gas recirculation is investigated. The energy efficiency, CO_2 emission coefficient (CEC)

and NiO formation are used as parameters for comparing the different configuration performance.

It is normal for an integrated system that leads to a complicated process involving many controlled and manipulated variables and requires an efficient control system. Regarding the control of a fuel cell system, many researchers has been showing there are many possible control structures for a single fuel cell system to meet their desired operations (control objectives) related to its performance such as power, fuel utilization and etc. (Bizon et al., 2015; Braun et al., 2012; Chaisantikulwat et al., 2008; Huang et al., 2011). To date, control of fuel cells has mostly been focused on stabilizing control and less on economic control. In addition, depending on the objective of the control strategy, different manipulated variables possibly can be used to control the fuel cells. For example, the air flow rate can be used to control either the cell temperature or fuel utilization. Although the economic control for an SOFC was studied by Chatrattanawet et al. (2015), there are still some gaps when it is applied to the SOFC and MCFC integrated system such as the difference in SOFC operation. Moreover, the SOFC-MCFC integrated system operation might be changed to maximize total power. Thus, the control of such a system could require a different control structure to achieve the best profit.

The control part work focuses on a control structure design for the SOFC-MCFC integrated system using Skogestad (2004) stepwise. A carbon tax is also considered in the economic objective function because carbon dioxide emissions are currently an important concern for power plants (Aghaie et al., 2016). Constraints are included to ensure safe and feasible operation, e.g., a constraint to avoid NiO formation. Active constraint regions are identified, and self-optimizing controlled variables are selected for the remaining unconstrained variables. In addition, the throughput manipulator (TPM) is selected, and the pairing of controlled-manipulated variables are discussed. Finally, the control loops based on this analysis are proposed and implemented with PID using SIMC tuning method.

In general, the electricity demand varies according to the load. However, fuel cells prefer to be operated in a steady-state mode for a safe operation reason and thus, energy storage should be implemented within the fuel cell system for the use of load-following applications (Nease et al., 2016). To avoid energy loss in the energy

storage, an afterburner, in which the exhaust gas from the MCFC is burned to recover the useful energy and increase the CO_2 concentration, can be replaced with the combustion chamber of a gas turbine (GT) to generate more electrical energy. The additional generated power from a GT is captured by energy storage for later use. This approach can maintain a constant power generation from the integrated fuel cell system during operation.

The compressed air energy storage (CAES) system provides many benefits such as large power and energy capacities, a long-life cycle, and a fast response time (Guney and Tepe, 2017; Nease and Adams Ii, 2014). In addition, CAES is the cheapest energy storage system available to date (Sheng et al., 2017). Recently, thermal energy storage (TES) technology is adopted into CAES technology to extract heat from the compression process during the charging phase and to release this heat prior to expansion process. This is the second generation of CAES named advanced adiabatic compressed air energy storage (AA-CAES) systems, which eliminate the use of fuels to heat up the compressed air is avoided during the discharging mode (Mozayeni et al., 2017). Zhang et al. (2016) did the thermodynamic analysis to compare the energy storage systems (ESSs) with different working fluids, compressed air (AA-CAES), compressed carbon dioxide (CCES) and liquid carbon dioxide. The result revealed that the AA-CAES system provided the highest system efficiency; however, it requires a bigger storage volume than CCES requires. Although air requires more space than CO_2, the AA-CAES system seems to be more suitable for application to the fuel cell systems because air is used in both the fuel cell systems and the combustion process. Moreover, the extraction of CO_2 from the N_2-containing gas becomes difficult and requires additional units and energy. The hot air from the AA-CAES system can also be used in the integrated fuel cell system to reduce the heat duty of the preheater unit.

In the final part of this research, the afterburner of the integrated fuel cell system is replaced with a combustion chamber of GT to capture the generated power of the GT in an AA-CAES system for future power supply. The system is investigated to elucidate the amount of energy that can be further generated by using only the remaining fuel from the system to supply the load during high power demand.

Additional GT and AA-CAES air feed and pressure ratios are the parameters for designing this system.

1.2   Research objective

The objective of this research is to design the integrated of solid oxide fuel cell (SOFC) and molten carbonate fuel cell (MCFC) system by utilizing an exhaust gas of the SOFC to further improve the overall performance, to study the control structure design of the designed integrated system, and to design the integrated system for power demand variation case. The research scopes are as follows:

1. To investigate the performances of the SOFC-MCFC integrated system fed by methane under steady-state simulations with different operating conditions; degree of pre-reforming, fuel cell operating temperature and fuel utilization. The performances are also compared with a single SOFC and a MCFC.

2. To investigate the influence of the SOFC-MCFC integrated system configurations; series, parallel and combined series-parallel configuration, on the performance under steady-state simulations. The generated power per methane feed, carbon dioxide coefficient and NiO formation are used to justify which configuration offers the best performance in power improvement point of view.

3. To design control structure of the SOFC-MCFC integrated system based on Skogestad's control structure design in order to identify the necessary control variables and pairing of controlled-manipulated variables. Then, proposed control structure is implemented with PID controllers.

4. To study and design the SOFC-MCFC integrated system with GT without addition fuel feed. Then, the additional power generated from GT is stored in the AA-CAES for future power supply. This hybrid system is investigated under various pressure ratios to determine the suitable conditions.

1.3   Research Procedures

The procedures of this research are as follows:

1. Study the basic principle of fuel cell and survey literature of SOFC and MCFC model and related topic.

2. Validate the electrochemical models of a planar SOFC and MCFC fed according to experimental data from the literatures.

3. Simulate the validated model of SOFC and MCFC under steady state condition using Matlab. The effect of degree of pre-reforming, fuel cell operating temperature and fuel utilization to the SOFC-MCFC integrated fuel cell performance using MCFC at the downstream of the integrated system are investigated and compared with the single SOFC and MCFC system performance.

4. Investigate the influence of different configurations of the SOFC-MCFC integrated system on the power generation per unit fuel feed, carbon dioxide coefficient and NiO formation.

5. Perform Skogestad's control structure design on the configuration offering the best power generation improvement to identify the important variables that should be controlled and identify the pairing of controlled-manipulated variables.

6. Implement PID to the proposed control structure using SIMC tuning technique.

7. Design and investigate the SOFC-MCFC integrated system with GT to use up the remaining fuel.

8. Investigate power generation form the hybrid system at peak load when the power generated by the GT is stored in AA-CAES.

9. Discuss the results and make a conclusion.

10. Write-up the thesis.

1.4   Dissertation overview

This dissertation is organized as follows:

CHAPTER 1 presents the research background and motivation of this research. The research objective and dissertation overview are also presented.

CHAPTER 2 reviews literature for work related to the design and modeling of SOFC, MCFC, GT, CAES and control structure design.

CHAPTER 3 discusses a general basic principle of fuel cells, SOFC and MCFC, GT and CAES. The theory of control structure design is also described.

CHAPTER 4 explains a mathematical model of SOFC, MCFC, GT, CAES and control structure design.

CHAPTER 5 presents the performance investigation of the SOFC and MCFC integrated system. The effects of key operating conditions, such as temperature and fuel utilization, on the system performance, are investigated.

CHAPTER 6 presents the performance analysis of the SOFC and MCFC integrated system with different configurations. The suitable configuration for higher power generation is selected. The NiO formation possibility is also considered during the selection.

CHAPTER 7 focuses on control structure design of the SOFC and the MCFC integrated system. A procedure for selecting an active constraint and self-optimizing variables is presented. Moreover, the relative gain array (RGA) considered as a controllability index for the selection of input-output pairings is also implemented.

CHAPTER 8 presents the design of a hybrid SOFC-MCFC-GT system with AA-CAES system to cope with the variation of power demand. Power generation during charging and discharging phases are investigated

CHAPTER 9 gives the conclusions of this dissertation.

CHAPTER 2
LITERATURE REVIEW

In this chapter, literature reviews of Solid Oxide Fuel Cells (SOFCs), integrated SOFC system, Molten Carbonate Fuel Cells (MCFCs), control of fuel cell system, gas turbine (GT) and compressed air energy storage (CAES) are described. The design of SOFC and integrated SOFC are explained in section 2.1. The related MCFC design is explained in the next section. Section 2.3 explains the fuel cell control system case. Finally, GT and CAES in power demand variation applications is presented.

2.1 SOFC

There are three configurations of the SOFC that have been developed in several publications; tubular, planar and monolithic. Among of these configurations, the planar configuration is easier and cheaper to construct than others. Moreover, this configuration provides very high volumetric power densities and simpler to manufacture than tubular configuration (Kakaç et al., 2007). Laurencin et al. (2008) used a planar SOFC fed directly with methane to study the thermal and electrochemical behavior. The important design feature of the planar SOFC relates to gas flow configuration which can be arranged in several ways such as cross-flow, co-flow or counter-flow. Aguiar et al. (2004) studied the system behavior under co and counter-flow operations. The results showed that the co-flow configuration is better than the counter-flow because the counter-flow leads to steep temperature gradients with a consequent uneven current density distribution.

Because of the high operating temperatures of SOFCs, the materials used in the cell components are limited by chemical stability in oxidizing and reducing environments, chemical stability of contacting materials, etc. Therefore, the developing cells with compositions of oxide and metals that operate at intermediate temperatures have been investigated. A SOFC electrolyte is yttria-stabilised zirconia (YSZ), an oxide ion conductor at elevated temperatures. The anode is usually a nickel/zirconia cermet, which provides high electrochemical performance, good chemical stability, and low cost, and the cathode is a perovskite material, such as

strontium doped lanthanum manganite, often mixed with YSZ in the form of a composite (Aguiar et al., 2004). However, it is usually observed that the intermediate temperature operation causes an increase of internal resistance of cell. Therefore, there are several researchers analyzing the performance of a planar IT-SOFC with different support structures such as electrolyte-supported and electrode-supported. Patcharavorachot et al. (2008) studied the role of support structures which the result showed that an anode-supported SOFC is superior to an electrolyte-supported and cathode-supported SOFC. Chan et al. (2001) presented sensitivity tests to show the effect of the thickness of the respective fuel cell components on the drop in cell voltage. Results showed that the performance of an anode-supported fuel cell is superior to that using cathode as the support under elevated operating pressure in the cathode compartment.

The electrochemical modeling and parametric study of SOFCs relate to the structures and materials. Methane fed solid oxide fuel cells model and parameter were presented by Ni (2009). An important feature of this model is that the effects of electrode structural parameters on both the exchange current density and gas diffusion coefficients are fully taken into consideration. The simulation results of parametric analyses showed that all the overpotentials decreased with increasing temperature. At low current densities, low porosity and pore size are desirable to reduce the electrode total overpotentials as concentration overpotential is insignificant compared with activation overpotential. At high current densities, the total overpotentials can be minimized at optimal porosities and pore sizes. Chan et al. (2001) presented a complete polarization model of a solid oxide fuel cell (SOFC) that eliminates the ambiguity of the suitability of such model when used under different design and operating conditions. The Butler-Volmer equation is used in the model to describe the activation overpotential instead of using simplified expressions such as the Tafel equation and the linear current-potential equation. In the concentration overpotential, both ordinary and Knudsen diffusions are considered to cater for different porous electrode designs. Kulikovsky (2009) presented a model for anode performance of a planar anode-supported SOFC. The model includes Butler–Volmer relation for the hydrogen oxidation, Ohm's law for ionic current and equation of hydrogen mass balance in the anode channel. In the low-current regime, the anode polarization

voltage is proportional to cell current, which justifies the notion of anodic activation resistivity, R_a. In the high-current regime, polarization voltage depends on cell current logarithmically, with the effective Tafel slope being twice the kinetic value (doubling of Tafel slope).

Aguiar et al. (2004) developed a dynamic model of an anode-supported intermediate temperature direct internal reforming planar solid oxide fuel cell stack. The developed model consists of mass and energy balances, and an electrochemical model that relates the fuel and air gas composition and temperature to voltage, current density, and other relevant fuel cell variables. The electrochemical performance of the cell is analyzed for several temperatures and fuel utilizations. The steady-state performance of the cell and the impact of changes in fuel and air inlet temperatures, fuel utilization, average current density, and flow configuration are studied.

Because excessive steam will dilute the hydrogen concentration and cause hydrogen deficiency in the cell stack SOFCs and the same affect happens when it operates at a high fuel utilization rate. A hydrogen deficiency causes a collapse in the physical structure as NiO forms and corrosion occur at the anode of the SOFC (Nehter, 2007). The study by Parhizkar and Roshandel (2017) also confirmed that under the optimum operating conditions, the SOFC should be operated at a moderate fuel utilization to avoid a long-term cell degradation caused by microstructural changes of Ni particles in anode. Thus, SOFCs tend to operate at a moderate fuel utilization rate; the resulting exhaust gas from the SOFC anode is still valuable due to the quantity of remaining fuels.

Many researches have been carried out to enhance the SOFC system performance. The first option, the exhaust gases from the anode and cathode are mixed and burned in an afterburner to generate heat, which is required for upstream preheating or steam production as the work of Zhang et al. (2017). They proposed the hybrid SOFC system with a thermoelectric generator and thermoelectric cooler to recover the waste heat from SOFC. It is found that the efficiency of the proposed system allows 4.6% larger than that of the stand-alone SOFC. The second way to improve the performance of the system is by recycling the exhaust gases; the anode and/or cathode can also be recycled, eliminating or reducing the required external steam and improving the excess heat recovery. Zhang et al. (2017) used a multi-stage

exhaust energy recycling strategy to enhance the SOFC-CHP system efficiency; an anode off gas was recirculated to the reformer providing steam and heat for the reforming process. It is found that system with anode off gas recovery (AOGR) & exhaust gas combustion (EGC) modules leads to the best comprehensive performance with electrical efficiency of 59.3%.

The combined systems with SOFCs, such as an SOFC combined with a gas turbine (SOFC-GT) or combined with another fuel cell, are alternatively potential way to improve the electrical efficiency. For SOFC-GT, Sarmah and Gogoi (2017) designed the combined SOFC power system with gas turbine and steam turbine cycles by using the remaining fuel for a gas turbine cycle. They found that the system with single pressure ST cycle would be the most appropriate as it is less number of components and minimum total cost with 56.77% electrical efficiency. Many researchers also have theoretically studied on the integration of SOFCs with other fuel cells. The SOFC with other low temperature fuel cell types, several purifying units were required to treat the exhaust gas from SOFC before it can be fed to another lower operating temperature fuel cell. Yokoo and Take (2004) proposed a system with an SOFC and a polymer electrolyte fuel cell (SOFC-PEFC) provided an efficiency of 59%. In their design, the SOFC acted as a fuel processor for the PEFC and the PEFC acted as an air preheater for the SOFC. Obara (2010) proposed a combined SOFC and proton exchange membrane fuel cell (SOFC-PEM) system in which the SOFC is designed to correspond to base load operation and the PEM is designed to correspond to fluctuation load. The system provided an efficiency of 48% and a slight fuel consumption reduction. Two-staged SOFCs, low and high-temperature SOFCs, with a serial connection were studied by Araki et al. (2006). The high-temperature SOFC uses directly the exhaust gas of the low-temperature SOFC to increase overall power generation efficiency. The system provided an efficiency of 50.3% which is a little higher than the system provided by the high-temperature SOFC only. Patcharavorachot et al. (2010) investigated the performance of the oxygen-ion and proton-conducting electrolyte SOFC hybrid system. The proton-conducting electrolyte SOFC was integrated into the oxygen-ion-conducting electrolyte SOFC to produce more H_2 then to get more power because proton-conducting electrolyte

SOFC has a better theoretical performance. The system with a promising efficiency of 54.11% can be provided at the optimal operation.

2.2 MCFC

Antolini (2011) reviewed the stability of molten carbonate fuel cell electrodes. He also considered the electrodes that are used in internal reforming molten carbonate fuel cell (DIR-MCFC). For cathodes, He founded there are many different ways that have been tried to increase the stability of cathode in MCFC conditions, such as the increase of the basicity of the electrolyte, the addition of basic oxides to NiO, the development of new stable cathode materials and the protection of the Ni-based cathode by an electrochemically active oxide layer with low solubility. All these methods are effective to reduce NiO dissolution into electrolyte. He claimed that the addition of a low amount (63 mol%) of La_2O_3 to the electrolyte or to the cathode is the best method to reduce NiO dissolution considering the very low NiO dissolution in the electrolyte and the simple method of preparation. In addition, DIR-MCFC anode on the electrolyte matrix should avoid K_2CO_3 in electrolyte and should substitute Na_2CO_3. For anodes, Metal addition such as Au, Ag and Cu to Ni can improve the resistance to coke formation. Thus, to increase the resistance to alkali poisoning and coke formation the best solution seems to be the use Ag–Ni/Al_2O_3 as DIR-MCFC anode catalyst. The presence of Ag decreases the formation of carbon filaments, while Al_2O_3 increases the alkali resistance of the catalyst.

Freni et al. (1994) analyzed the influence of the operating parameters on the energy balances of a MCFC fueled with indirect internal reforming (IIR-MCFC) by using a mathematical model at equilibrium. The methane conversion and the electrical efficiency were investigated by changing operating temperature (893 to 973 K) and steam/carbon ratio (1.5 to 2.5). The results showed that the steam/carbon ratio mostly influences the electrical efficiency of the system operating at low temperature (893 K). In fact, the high temperatures (923 and 973 K) favor the steam-reforming reaction thus balancing the detrimental effect of the steam/carbon ratio lower. Hence, the temperature is the important parameter affecting the cell performance, because it influences the methane-reforming equilibrium as well as the cell kinetics, reducing the electrodes overpotentials.

Morita et al. (2002) analyzed the performance of molten carbonate fuel cell using a Li/Na electrolyte and Li/K electrolyte in comparison and the behavior during long-term performance. The experiment showed that Li/Na cell performance is superior in output voltage to the Li/K cell performance under a condition of 1.00 atm and 650 ℃. The temperature dependence of Li/Na cells under atmospheric conditions is larger than that of Li/K cells. Voltage decay rate in long-term operation is similar between Li/K and Li/Na cells. As a result of the long-term operation in bench-scale cell, which makes the electrolyte loss as small as possible in order to estimate the behavior of long-term performance on stack-scale cell level, the voltage decay is mainly caused by the increase of internal resistance. Moreover, they also proposed the expressions of the overpotentials in equivalent ohmic resistance for anode, cathode and electrolyte. The expressions of the anode and cathode are functions of the reactant partial pressures.

Liu and Weng (2010) developed a dynamic model of MCFC. They presented a one-dimensional mathematical model for MCFC considering the variation of local gas properties, and the experimental analysis for the validation of model. The volume–resistance (V–R) characteristic modeling method had been introduced. The partial differential equations for mass, energy and momentum balance can be modified by using the V–R modeling method and the modular modeling idea in order to develop a model for quick simulation. The simulation result had a good agreement with experimental.

Moreover, Muñoz et al. (2011) classified MCFC model into three groups and compared their ability to predict fuel cell performance. The model presented by Liu and Weng (2010) was classified into model type C1 which is based on a combined experimental and theoretical approach. The model is in the form of the equivalent global resistances of electrodes and electrolyte. Each model is validated against many other experiments, including the point that far from the design point. The result showed model C1 is a good model with the best balanced between simple mathematical and satisfactory accuracy in a broad range of operating conditions.

Due to carbon dioxide emission in a process, MCFCs are recently gained attention as an alternative CO_2 utilization technology. MCFC is used to support the CO_2 capture system in many processes such as cement industry and power plant. In

cement plants, Spinelli et al. (2014) used the MCFC to reduce to power consumption in CO_2 purification process which is located at the downstream of the cement process. The result showed a remarkable high CO_2 avoided (up to about 70%) and Specific Primary Energy Consumption for CO_2 captured (SPECCA) is much lower for the proposed MCFC plants than for a conventional MEA system.

Wee (2014) claimed that MCFCs act as CO_2 concentrators or separators when integrated into traditional power plants, and they can increase the overall electrical efficiency and reduce CO_2 emission per power generation because of additional power generation and an increase in CO_2 recirculation inside the system. Currently, MCFCs are used in the bottom stream in a power plant to utilize CO_2 and reduce CO_2 emission (Discepoli et al., 2016). Discepoli et al. (2012) did experimental tests on using the MCFC to separate CO_2 from the exhaust gases of a combined heat and power plant to point out the limit in the operations. The was found that the carbon dioxide concentration in the cathode was a critical factor that can induce quick voltage drops and make the cell sensitive to the other parameters. Carapellucci, Saia, and Giordano (2014) studied different configurations of using a MCFC as a CO_2 separator of a natural gas combined-cycle (NGCC), including cases of using exhaust gas recirculation with and without CO_2 capture. The results showed that the addition of a MCFC fed by GT exhaust gas markedly increases the power generation by +39% with specific CO_2 emission (without a capture system) reduces from 397 to 381 kg/MWh and the efficiency remains almost unchanged. However, all the case that without a carbon capture can slightly reduce the specific CO_2 emission due to the increase in power generation.

McPhail et al. (2011) analyzed the overlapping of materials, operating operations and applications of SOFC and MCFC and did mention the possibility of merging the solid oxide and molten carbonate electrolytes by creating a composite electrolyte based on carbonate-impregnated ceramics as a result of the similarity in their operating temperature and anode catalyst. It's however rather to be a new fuel cell concept. Samanta and Ghosh (2017) used both an SOFC and a MCFC to repower a coal fired power plant. In their design, an SOFC is integrated at the upstream of the present boiler and a MCFC is integrated with MEA to capture CO_2 at the downstream of the present boiler. They claimed that the net plant output increase by 57%, net

efficiency increases by 11% and specific CO_2 emission reduces by 90%, although the price of electricity produced increases by 46.5%.

2.3   Control of fuel cell systems

In the modeling research field of fuel cells, the models have been developed to simulate the behavior and it can be ranged from zero- to three-dimensional models (some literature showed in chapter 2.1 and 2.2). The level of details including in a mathematical model depend on the purpose of using the model. For optimization and control strategies, the art is not to include every complexity but to include enough details to predict the interested variables accurately enough, hence simple and accurate models are very valuable and it is a reason of most fuel cell control strategies rely on lump and one-dimensional models (Bavarian et al., 2010).

However, Georgis et al. (2011) asserted that lumped models considered only time changes are sufficiently accurate for analysis and control of fuel cell systems. They also showed some evidence of other researcher using lumped models for analyst control of fuel cell with achieved overall accuracy of 10-15%. Xi et al. (2010) also showed that lumped-parameter models are adequately accurate for systems-level analysis and control through experimental validation. In addition, Murshed et al. (2007) implemented more details in the lumped model including the separation of component energy balance for analysis and control of the planar SOFC systems. The added detail into the lamped model do not affect much in the term of computational time in analysis.

There are many possible ways to control a process to meet the objective and a fuel cell system has no exception. The work of Bizon et al. (2015) showed that a standalone renewable/fuel cell hybrid power source had 4 possible control structures for the load following and maximum efficiency point tracking problem. In their design, the fuel cell power generation is controlled via the fueling rates; one is controlled in the load following loop and another is used to controlled in the maximum efficiency point tracking loop. Each control topology is efficient for different loads. Chaisantikulwat et al. (2008) studied the control system of an anode supported planar SOFC using first-order transfer functions. They indicated that cell

voltage is a key variable to be controlled due to load changes. For small changes in the load current case, it can be effectively controlled by PI controllers using the hydrogen concentration in the fuel as the manipulated variable. They also stated that temperature played an importance role in the performance and failure of the fuel cell and thus it should be maintained within an acceptable range. Huang et al. (2011) reviewed the dynamic modelling and control systems of a fuel cell system. It found out that a simple model may perform better a complex 3D model and the control objectives were targeted for the operation, temperature, power and fuel utilization. Fuel and air flow rates can be manipulated variables to achieve the above targets. Moreover, current density, the inlet temperatures of fuel and air can be either a manipulated variable or a disturbance variable depending on the objective. For univariate control scenario, fuel rate can be used to control power whereas air rate can be used to control either fuel utilization or fuel cell temperature. If it is used to control fuel utilization, the override temperature control can be used to maintain the cell temperature below its maximum allowance. In this case, addition of a pre-heat exchanger (additional degree of freedom) requires to maintain the cell temperature. Hajimolana and Soroush (2009) studied a simple control (PI controller) of a tubular solid oxide fuel cell system to control the cell output voltage and cell-tube temperature via manipulating the pressure and temperature of the inlet air stream, respectively. The results showed that the performance of control system can successfully reject unmeasured disturbances in the load resistance, the velocity of the inlet air and fuel stream, and the pressure and temperature of fuel stream. Aguiar et al. (2005) implemented a typical feedback PID temperature controller into a planar anode-supported intermediate-temperature direct internal reforming solid oxide fuel cell by manipulating the air ratio and imposing current density as disturbance with the constants of fuel utilization and air ratio. Their research further proved the need for process control to enhance the reliability and minimize the degradation of a SOFC. However, an adjustable set-point control strategy is more effective in avoiding oscillatory control action for the load changes of higher magnitude. This leads to operation failure, as well as in preventing potentially damaging temperature gradients

that lead to cell breakdown. Above examples show that simple controllers like PID controllers are able to control a fuel cell system to meet the target even more complex system. Kandepu et al. (2007) showed that PI controllers can control the power output and the cell temperature by manipulating the fuel and air feed flow rates, respectively in a SOFC combined with a gas turbine (GT) system. The controllers provide satisfactory performance for load changes at the cost of efficiency. Kaneko et al. (2006) implemented a standard PID control strategy to control the power and temperature of fluctuating biomass gas fueled solid oxide fuel cell (SOFC) by manipulating inlet fuel flow rate for controlling the power output of the system and by manipulating a bypass valve around the recuperator for controlling the cell temperature. By releasing excess heat to the exhaust, the bypass valve provided the control means to avoid the self-exciting behavior of system temperature and stabilized the temperature of SOFC. However, Braun et al. (2012) categorized the objective of an SOFC control system, which was mostly related to its performance (to meet a design output), in terms of safety and operation (to maintain inputs and outputs within desired bounds).

Because the integrated system involves many uncertain parameters, the control design should take a model uncertainty into account. In addition, depending on the objective of the control strategy, different manipulated variables possibly can be used to control the fuel cells. Skogestad (2004) has proposed a procedure for control structure design for complete chemical plants. At the beginning of the procedure, the operational and economic objectives, and degree of freedom was carefully defined with the aim of avoidance of real time optimization. In addition, the second part of the procedure has the goal to stabilize the system. Control structure design deals with the structural decisions of the control system, including the selection of manipulated variables, controlled variables, control configuration, and controller type and pairing the variables to form control loops (Skogestad and Postlethwaite, 2005). The self-optimizing control is implemented to select the good controlled variable which can be kept constant at setpoints without the need to re-optimize when disturbance occur (Skogestad, 2000). Panahi et al. (2010) studied self-optimizing and control structure design for a CO_2 capturing plant. The result found that the temperature close to the

top of the stripper to be a good controlled variable for the remaining unconstrained degree of freedom. Chatrattanawet et al. (2015) studied control structure design of direct internal reforming SOFC. The analysis showed the system was 2 DOFs system problem which the cell temperature and the fraction of fuel needed to be controlled. The RGA number recommended that air flow rate was used to control the cell temperature and the fuel flow rate was used to control the fuel fraction. The closed-loop respond showed the controlled can control the system well. However, there are still some gaps to implement economic control studied by Chatrattanawet et al. (2015) into the integrated system.

2.4   Gas Turbine and compressed air energy storage

Both SOFCs and MCFCs are able to implement with GTs because of their high operating temperatures. In addition, the remaining gas from the FC can be further used to generate additional power. Haseli et al. (2008) studied a gas turbine cycle combined with a solid oxide fuel cell using thermodynamic modeling. The Individual models were developed for each component, through applications of the first and second laws of thermodynamics. They also found that increasing the turbine inlet temperature results in decreasing the thermal efficiency of the cycle, whereas it improves the net specific power output. Moreover, an increase in either the turbine inlet temperature or compression ratio leads to a higher rate of entropy generation within the plant. It was found that the combustor and SOFC contribute predominantly to the total irreversibility of the system. About 60% of the irreversibility takes place in the following components at typical operating conditions: 31.4% in the combustor and 27.9% in the SOFC. The thermal efficiency of the integrated cycle becomes as high as 60.6% at the optimum compression ratio (around 4). However, their proposed system required some fuel fed to the combustor of the gas turbine.

Saebea et al. (2013) analyzed a pressurized solid oxide fuel cell-gas turbine hybrid system with cathode gas recirculation using ethanol as a fuel. When considering an energy management of the system, it is found that a heat input is highly required to preheat air before being fed to the SOFC stack. The results showed that an increase in the operating pressure dramatically improves the system electrical efficiency. The highest system electrical efficiency and the lowest recuperation energy

from the waste heat of the GT exhaust gas can be achieved when 4-6 bar of operating pressure is used. They also found that the SOFC-GT system requires a high recirculation of the cathode exhaust gas to maintain the system without supplying the external heat under a high-pressure operation; however, the increased recirculation ratio of the cathode exhaust gas reduces the system electrical efficiency.

Orecchini et al. (2006) studied the MCFC and microturbine power plant simulation in order to develop the necessary models to analyze different plant configurations. They developed MCFC mathematic model starting from the geometrical and thermofluidodynamic parameter of the cell. They also developed plate reformer model, a particular compact reformer that exploit the heat obtained by a catalytic combustion of the anode and part of cathode exhausts to reform methane and steam, microturbine-compressor model that describe the efficiency and pressure ratio of the two machines as a function of the mass flow and rotational regime. The simulation of the fuel cell had showed that global electrical efficiency surely can be kept easily over 50–55%, and a cogenerative efficiency about 75%.

El-Emam and Dincer (2011) analyzed the energy and exergy of the MCFC combined with a gas turbine using biogas as a fuel. The system and its components used the mass, energy, entropy and exergy balance equations in simulation process. The results showed that the maximum work output of the MCFC was estimated as 314.3 kW when operating at 650 °C. The overall energy and exergy efficiencies achieved for this system are 42.89% and 37.75%, respectively. The catalytic burner, HRSG and the combustion chamber appeared to have high values of exergy destructions as there is a potential for improvement. Exergy destruction of different devices in the studied system was affected by changing the ambient temperature. They also found that the energy and exergy efficiencies of the MCFC and the overall system increased with increasing the temperature within the operating temperature range of the MCFC.

Energy storage system (ESS) may be classified into 5 main categories such as chemical, electrochemical, electrical, mechanical, and thermal energy storage (Guney and Tepe, 2017). Compressed air energy storage (CAES) system, is one of the mechanical energy storage system, uses a compressor to pressurize air and pumps it into the storage which can be expanded in a turbine when it is needed. This system

provides many benefits such as large power and energy capacities, long life cycle, low cost per kWh, and minor needs for power electronic converters. However, it is favorable for large scale power plant (>100 kW). Ibrahim, Ilinca, and Perron (2008) also reviewed energy storage systems and classify large-scale energy storage into three main operational categories such as power quality required, buffer and emergency storage, and network management. CAES is considered to be in network management category which is used to decouple synchronization between power generation and consumption. The CAES provides high efficiencies, lifetime cycles and relative low investment cost. The comparison also showed that the investment cost per charge-discharge cycle of the CAES is low. The overall analysis of the comparisons of energy storage techniques suggest that compressed air and flow batteries are the best choices for the process concerning peak-hour load levelling.

Nease and Adams Ii (2014) designed an integrated SOFC with a compressed air energy storage (CAES) system for a load-following power production with 100% CO_2 capture. During charging phase, part of power generation by the SOFC is used to store the spent air from the SOFC in the CAES. During discharging phase, the spent air from the SOFC is rather spent to produce power through the turbines and stored air is released to the another set of turbines. The remaining fuel from the SOFC is completely burned with high-purity O_2 provided by the ASU. The results showed that the addition of CAES to an SOFC-based system significantly improves load following capabilities with the low levelized cost of electricity (LCOE). Moreover, the carbon capture and sequestration (CCS) is able to reduce the total CO_2 emissions of the plant to nearly zero.

Mozayeni et al. (2017) studied the effect of storage pressure, pre-set pressure, compressor and turbine efficiency on the performance of an advance adiabatic compressed air energy storage (AA-CAES) system which is the second generation of the CAES system. Thermal Energy Storage (TES) is adopted to replace combustor to eliminate the need for fossil fuels in the AA-CAES system. The results showed that the storage pressure is an important parameter effecting the amount of energy stored and generated in the AA-CAES system. Moreover, the stored and generated energy was reduced in a semi-linear manner with increasing of the pre-set storage pressure.

Recently, ESS with carbon dioxide as working fluid has proposed as a candidate in CAES system. Zhang et al. (2016) used the thermodynamic analysis to compare the AA-CAES, compressed CO_2 energy storage (CCES), and liquid CO_2 systems. The results revealed that the AA-CAES system provided the highest system efficiency. However, the energy density of the CCES system was 2.8-fold higher than that of the AA-CAES system that indicates the AA-CAES requires more volume to store energy than the CCES.

Compressed air can be stored either at isochoric (constant volume) or at isobaric (constant pressure) (Budt et al., 2016). The pressure indicates the state of charge in the isochoric storage whereas the volume indicates the state of charge in the isobaric storage. Isochoric storage is such as a steel pressure vessel and a salt cavern. The example of isobaric storage is a hydraulically compensated reservoir or a balloon. The major drawback of the isochoric compressed air storage is change in pressure which affects on the efficiencies of compression and expansion machinery. Isobaric storage volumes don't have the effect in that way; however, it is more complex and not widespread.

Sheng et al. (2017) used a balloon to store compressed air under the ocean in a tidal turbine farm for daily power management in a stand-alone island. The conventional diesel generators were designed to be used only as backup supply. The results showed the proposed system can greatly help to decrease diesel generators fuel consumption and CO_2 emission.

CHAPTER 3
THEORY

This chapter presents a background theory of each unit. In the first part, fuel cell which consists of the principle of fuel cell, type of fuel cell, the advantage of each type and the fuel cell, SOFC and MCFC, operations is presented. Next part describes the control structure design procedure. Final part presents the principle of gas turbine and compressed air energy storage.

3.1   Fuel Cell

3.1.1   Principle of Fuel Cell

Fuel cells are the electrochemical devices which convert chemical energy of fuels directly into electrical power and produce water and heat as by-product. They provide electrical power as long as fuel and oxidant are added. Fuel cells avoid intermediate steps of producing heat and mechanical work thus they are not limited by thermodynamic limitations of heat engines such as the Carnot efficiency. Thank to limitations avoided, fuel cell can reach 60% of efficiency. The basic physical structure of a fuel cell consists of an electrolyte layer in contact with an anode and a cathode on either side of it as shown in **Figure 3.1**. This figure presents the flow directions of gases and the electrons and ion conductions. In the simplest fuel cell operation, hydrogen and oxygen are continuously fed to the anode side and the cathode side, respectively. Hydrogen is oxidized on the anode whereas oxygen is reduced on the cathode. The electrochemical reaction takes place on the electrode. In practical, electrochemical reaction is broken down into two half-cell reactions that occur in physically separate regions of the cell. These regions are interconnected by an electrolyte that conducts ions but not electrons. The oxidizing half-reaction released the electrons which can conduct to the reduction side via external circuit and establish the current that is the purpose of the cell. The ions that diffuse through the electrolyte can be positive or negative ions depending on the electrolyte type. Water is the byproduct, will be generated on the anode side if the negative ion conducting electrolyte is selected. Heat and exhaust gases are also produced by the fuel cell.
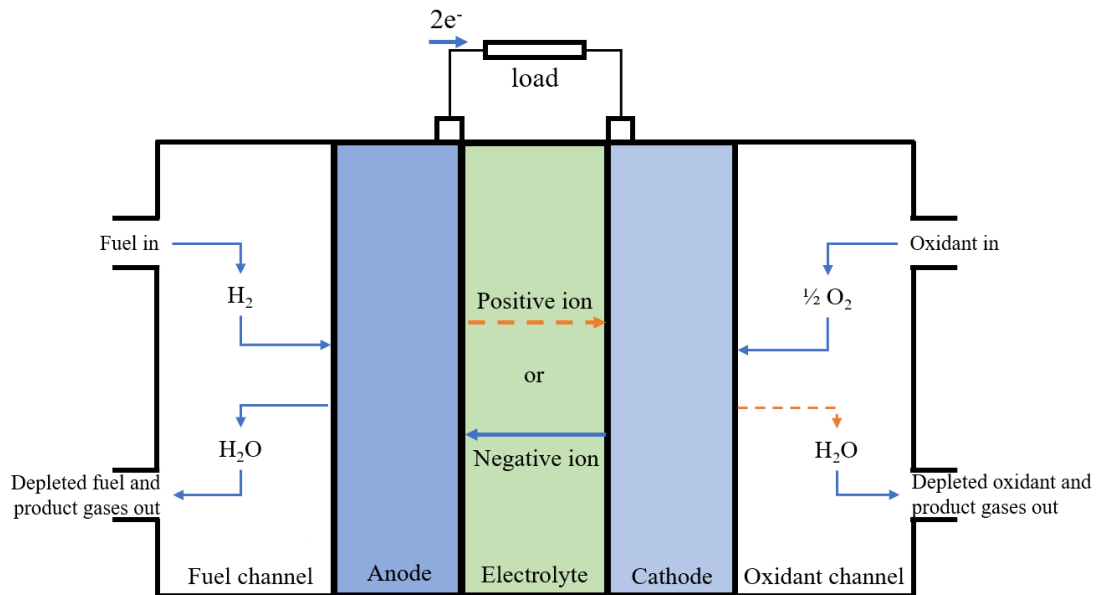
Figure 3.1 A schematic of fuel cell

3.1.2 Types of Fuel Cell

There are several types of fuel cells currently under development for wanted applications. Each type has its own advantages, limitations, and potential applications. The temperature of operation, kind of chemical reactions that take place in the cell, the kind of catalysts required, the fuel required and other factors affect which fuel cells are most suitable for the applications. Operating temperature, type of fuel, type of electrolytes, state of the electrolyte and chemical nature of electrolyte can be criteria of classification of fuel cells. Fuel Cells are commonly classified by the type of electrolytes used in the cells that include polymer electrolyte membrane fuel cell (PEMFC), alkaline fuel cell (AFC), phosphoric acid fuel cell (PAFC), molten carbonate fuel cell (MCFC), and solid oxide fuel cell (SOFC). The choice of electrolyte dictates broadly the operating temperature of the fuel cell. The operating temperature and useful life of a fuel cell dictate the physicochemical and thermo mechanical properties of materials used in the cell components such as electrodes, electrolyte, interconnect and current collector. The operating temperature also plays an important role in dictating the type of fuel that can be used in a fuel cell. In low-temperature fuel cells (LTFCs) such as PEMFC, AFC, and PAFC, all the fuel must be converted to hydrogen before it enters the fuel cell. In high-temperature fuel cells

(HTFCs) such as MCFC and SOFC, fuel such as CH_4 and CO can be directly feed to fuel cell and internally converted to hydrogen inside the fuel cell. **Table 3.1** presents details of the various fuel cells. The applications of the fuel cell, the advantage and disadvantage for each type of fuel cells are illustrated in **Table 3.2**.

Table 3.1 Description of Major Fuel Cell Types

	Types of fuel cells				
	polymer electrolyte membrane fuel cell (PEMFC)	alkaline fuel cell (AFC)	phosphoric acid fuel cell (PAFC)	molten carbonate fuel cell (MCFC)	solid oxide fuel cell (SOFC)
Operating Temperature (°C)	50-100	50-220	200	600-700	600-1000
Electrolyte	Polymer membrane	Liquid KOH (immobilized)	Liquid H_3PO_4 (immobilized)	Molten carbonate	Ceramic
Charge carrier	H^+	OH^-	H^+	CO_3^{2-}	O^{2-}
Cell component	Carbon based	Carbon based	Carbon based	Stainless based	Ceramic based
Interconnect	Carbon	Metal	Graphite	Stainless steel or Nickel	Nickel, ceramic, or steel
Electrode	Carbon	Transition metals	Carbon	Nickel and Nickel Oxide	Perovskite and perovskite/metal cermet
Catalyst	Platinum	Platinum	Platinum	Electrode material	Electrode material
Fuel compatibility	H_2, methanol	H_2	H_2	H_2, CH_4 CO	H_2, CH_4, CO
Product Water Management	Evaporative	Evaporative	Evaporative	Gaseous Product	Gaseous Product
Product Heat Management	Process Gas + Liquid Cooling Medium	Process Gas + Electrolyte Circulation	Process Gas + Liquid cooling medium or steam generation	Internal Reforming + Process Gas	Internal Reforming + Process Gas
Balance of Plant	Low-moderate	Moderate	Moderate	Complex	Moderate
Efficiency	40%	60%	40%	55%	55%
Size (MW)	0.25	very small	11	2	1-2

Table 3.2 The applications of the fuel cell, the advantage and disadvantage for each type of fuel cells

Types of fuel cells	Advantage	Disadvantage	Application
PEMFC	- Highest power density of all the fuel classes - Good start-stop capabilities - Suitable for portable applications	- Uses expensive platinum catalyst - Expensive polymer membrane and ancillary components - Required active water management - Very poor CO and S tolerance	- Transportation: cars, buses, boats - Residential: household electrical power needs - Portable: laptop computers, cell phones, medical equipment
AFC	- Improved cathode performance - non-precious metal catalysts - Low materials costs	- Must use pure H_2-O_2 - Must remove water from anode	- NASA space program: space vehicles
PAFC	- Mature technology - Excellent reliability/long term performance - Relatively low-cost electrolyte	- Expensive platinum catalyst - Susceptible to CO and S poisoning - Corrosive-liquided electrolyte	- Landfill/wastewater treatment facilies: To generate power from methane gas
MCFC	- Fuel flexibility - non-precious metal catalysts - High-quality waste heat - Relatively high power density	- Corrosive, molten electrolyte - Degradation/lifetime issues - Relatively expensive materials	- Commercial: utility power plants, airport terminals, schools, office buildings, hotels, hospitals
SOFC	- Fuel flexibility - non-precious metal catalysts - High-quality waste heat - Solid electrolyte - Relatively high power density	- Significant high-temperature materials issues - Sealing issues - Relatively expensive components/fabrication	- Commercial: utility power plants, airport terminals, public and commercial office buildings, hotels, hospitals

3.1.3 Solid Oxide Fuel Cell

Solid oxide fuel cell (SOFC) contains a solid oxide electrolyte made from ceramic materials such as yttria-stabilized zirconia and operates at high temperature which offers several advantages as shortly described in Section.

3.1.3.1 SOFC Operation

SOFC operates at 600ºC–1000ºC and atmospheric or elevated pressures where ionic conduction by oxygen ions takes place. The structure of SOFC is the solid state character of all SOFC components. This means that, in principle, there is no restriction on the cell configuration. The SOFC structure consists of two porous electrodes, anode and cathode, that sandwich an electrolyte. In general, a single unit of SOFC cannot produce adequate power and thus, it is necessary to stack SOFCs to increase the voltage and power. The interconnection in fuel cell stacks is desired to connect each cell in series as show in **Figure 3.2**, so that the electricity each cell generates can be combined. **Figure 3.3** shows a schematic view of basic SOFC operation.
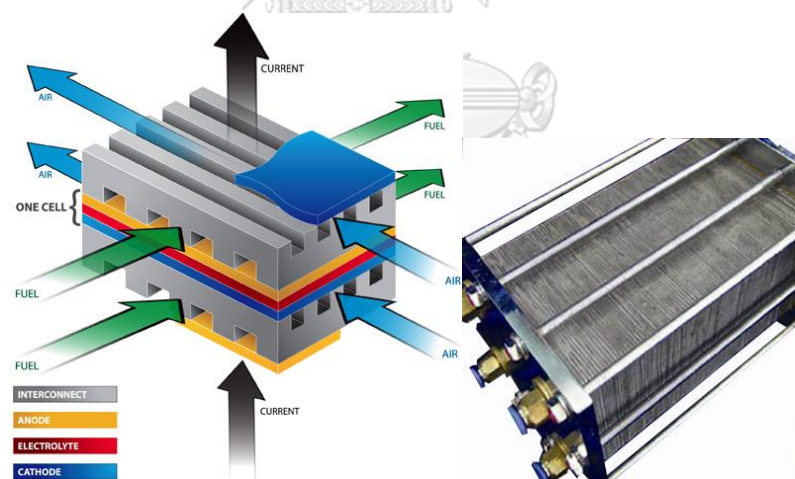
Figure 3.2 The connected SOFCs in series

(http://www.netl.doe.gov/research/coal/energy-systems/fuel-cells/solid-oxide-fuels/cell-stack-and-module)
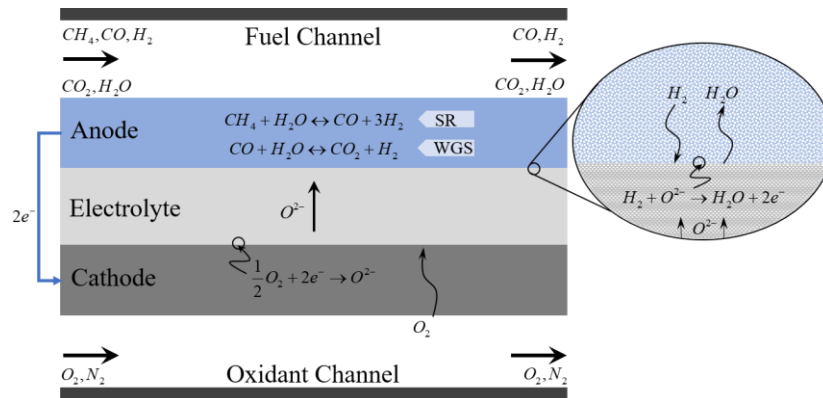
Figure 3.3 A basic solid oxide fuel cell operation.

Methane or syngas, carbon monoxide and hydrogen, is fed at the anode side and oxygen, usual air, is used as oxidant at the cathode side. At the cathode side, oxygen is reduced and formed into oxygen ions. Then oxygen ions diffuse through the ion-conducting electrolyte to the anode/electrolyte interface where they react chemically with hydrogen in the fuel. The dense structure of the electrolyte does not allow the passage of the cathodic gas through it, while the high ionic conductivity and the high electrical resistance allow only oxygen ions to migrate from the cathode to the anode. Water and heat as by-product are given off while electrons that are produced via the electrochemical reaction are released. The electrons transport through the anode via the external circuit, providing electrical energy and back to the cathode/electrolyte interface.

The electrochemical reactions occurring in SOFCs are based on Equations (3.1) and (3.2)

At the anode, oxygen ion reacts with hydrogen producing water

$$H_2 + O^{2-} \rightarrow H_2O + 2e^-$$

(3.1)

At the cathode, the reduction of oxygen occurs via

$$0.5O_2 + 2e^- \rightarrow O^{2-}$$

(3.2)

The overall reaction occurring in the cell is exothermic.

$$H_{2,\,(an)} + 0.5O_{2,\,(ca)} \rightarrow H_2O_{,\,(an)}$$

(3.3)

3.1.4 Molten Carbonate Fuel Cell

The electrolyte in molten carbonate fuel cell (MCFC) is a mixture of alkali carbonates, Li_2CO_3 and Na_2CO_3, immobilized in a $LiOAlO_2$ matrix. The carbonate ion, CO_3^{2-}, act as the electron carrier in the MCFC. A mixture of Li_2CO_3 and K_2CO^3 can be used as the electrolyte too as shortly described in Section 2.2

3.1.4.1 MCFC Operation

The molten carbonate fuel cell operates at approximately 650 °C. The high operating temperature is needed to achieve sufficient conductivity of the carbonate electrolyte, yet allow the use of low-cost metal cell components. The MCFC structure consists of two porous electrodes, anode and cathode, that sandwich an electrolyte. **Figure 3.4** shows a schematic view of basic MCFC operation.
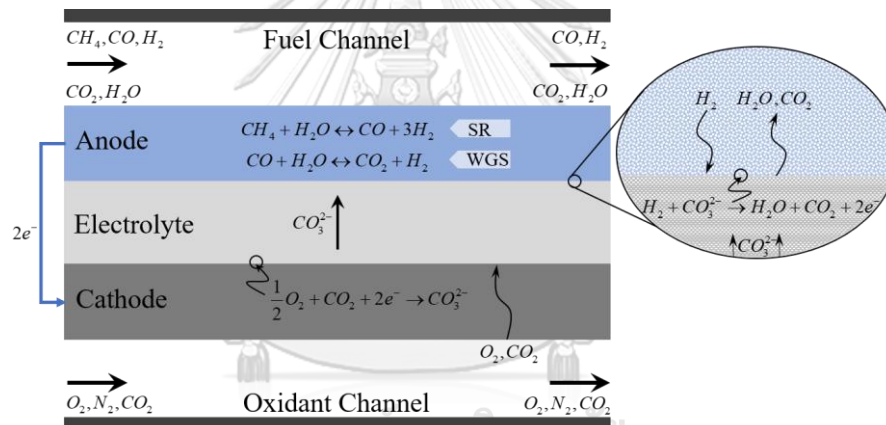
Figure 3.4 A basic molten carbonate fuel cell operation.

Methane or syngas, carbon monoxide and hydrogen, is fed at the anode side and oxygen and carbon dioxide are fed at the cathode side. At the cathode side, carbon dioxide is reduced and formed into carbonate ions. Then carbonate ions diffuse through the ion-conducting electrolyte to the anode/electrolyte interface where they react chemically with hydrogen in the fuel. The electrolyte does not allow the passage of the cathodic gas through it, while the high ionic conductivity and the high electrical resistance allow only carbonate ions to migrate from the cathode to the anode. Water and heat as by-product are given off while electrons that are produced via the electrochemical reaction are released. The electrons transport through the

anode via the external circuit, providing electrical energy and back to the cathode/electrolyte interface like that in SOFC.

The electrochemical reactions occurring in MCFCs are based on Equations (3.4) and (3.5).

At the anode, Oxidation reaction

$$H_2 + CO_3^{2-} \rightarrow H_2O + CO_2 + 2e^-$$ (3.4)

At the cathode, Reduction reaction

$$0.5O_2 + CO_2 + 2e^- \rightarrow CO_3^{2-}$$ (3.5)

The overall reaction (exothermic)

$$H_{2,(an)} + 0.5O_{2,(ca)} + CO_{2,(ca)} \rightarrow CO_{2,(an)} + H_2O_{,(an)}$$ (3.6)
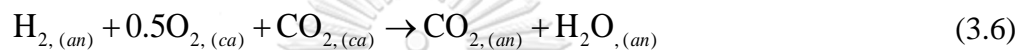
3.1.5 Internal Reforming of HTFCs

A hydrogen-rich gas can be converted by reforming of hydrocarbon fuels. Reforming process can be divided into internal reforming and external reforming according to where the reaction takes place. In this part will explain only internal reforming. Internal reforming that occurs inside the fuel cell itself (at the surface of anode's catalysts) is divided into indirect internal reforming (IIR) and direct internal reforming (DIR). The primary conversion may be accomplished with or without a catalyst via one of three major types of fuel reforming processes, i.e., steam reforming (SR), partial oxidation (POX) reforming, and autothermal reforming (AR).

Chemical reaction characteristics of three primary fuel reforming reactions are steam reforming reaction, partial oxidation and autothermal reforming. The steam reforming reaction produces the highest H_2 yield and cleanest exhaust as shown in **Table 3.3**. The low H_2 yield for another is a result of their intake of air; the oxygen in air partially oxidizes the fuel while the nitrogen in air dilutes the hydrogen composition in the outlet gas. For all three reactions, the H_2 yield can be increased by downstream use of the water gas shift reaction.

Table 3.3 Comparison of Chemical reaction characteristics of three primary fuel reforming reactions (O'Hayre et al., 2009)

Type	Chemical Reaction	Temperature Range (°C)	Outlet Gas Composition (with Natural Gas Fuel)					Exothermic or Endothermic?
			H_2	CO	O_2	N_2	Others	
Steam reforming	$C_xH_y + xH_2O\,(g) \leftrightarrow xCO + (\frac{1}{2}y + x)H_2$	700-1000	76%	9%	15%	0%	Trace NH_3, CH_4, SO_x	Endothermic
Partial oxidation	$C_xH_y + \frac{1}{2}xO_2 \leftrightarrow xCO + \frac{1}{2}yH_2$	>1000	41%	19%	1%	39%	Some NH_3, CH_4, SO_x, HC	Exothermic
Autothermal reforming	$C_xH_y + zH_2O\,(g) + (x - \frac{1}{2}z)O_2 \leftrightarrow xCO + (z + \frac{1}{2}y)H_2$	600-900	47%	3%	15%	34%	Trace NH_3, CH_4, SO_x, HC	Neutral

HTFCs, SOFCs and MCFCs, operate at the steam reforming environment. The steam reforming of hydrocarbons are required for HTFCs to gain the benefits of the high temperature operation. Internal reforming of the hydrocarbon fuels in HTFC systems increases the system efficiency by using waste heat recovery inside the stack to generate hydrogen. This can substantially reduce the complexity and cost of the system by elimination of the external reformer and associated heating arrangements and it reduce the stack cooling air requirements and associated equipment. Thus, internal reforming HTFCs offer significantly higher system efficiencies and reduced complexity compared to lower temperature fuel cells, as well as offer flexibility in the choice of fuel.

Direct internal reforming HTFCs (DIR-HTFCs) is the process that the reforming takes place directly on the anode and the fuels are supplied directly into the cell. This type offers the simplest and most cost effective design for a HTFC system. High-efficiency of using DIR-HTFC results from utilizing the heat from the exothermic electrochemical oxidation reaction to reform the hydrocarbon fuel which is a strongly endothermic reaction. A more advantage of direct internal reforming is the hydrogen is consumed to form steam via the electrochemical reactions, which help drive the reforming reaction to completion.

However, the problems with direct internal reforming is that it gives rise to a sharp endothermic cooling effect at the cell inlet, generating inhomogeneous temperature distributions and a steep temperature gradient along the length of the anode. This problem is very difficult to control and can result in cracking of the anode and electrolyte materials.

In indirect internal reforming HTFC (IIR-HTFC), the reformer unit is separated from the fuel cell but adjacent to the fuel cell anode. The heat from the exothermic fuel cell reaction is still utilized. Although indirect internal reforming is less efficient and less straightforward than direct reforming, it still represents a more efficient, simpler and more cost-effective approach than using an external reformer. The advantage of indirect internal reforming is much easier to control from a thermodynamic standpoint. Moreover, it is easier to develop dispersed catalysts which do not promote carbon deposition to the same extent as the nickel anode. Nevertheless, the conversion of fuels to hydrogen is not promoted as in the direct

internal reforming. A schematic of external reforming (ER), IIR and DIR HTFCs is illustrated in **Figure 3.5** to show where the reforming process occurring in the system.
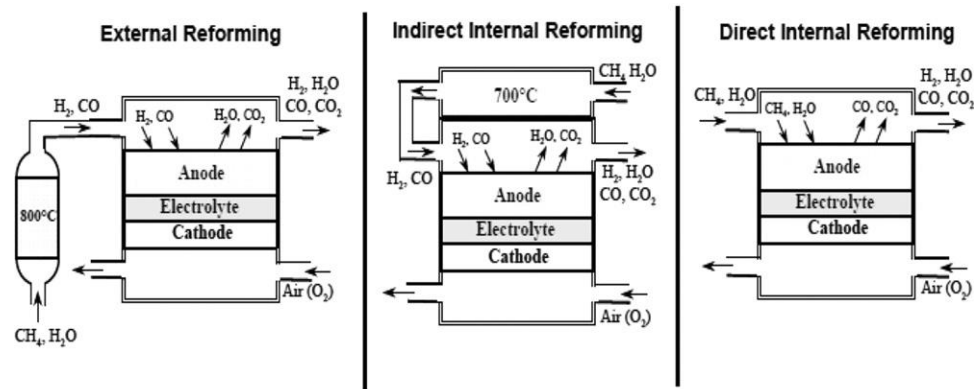
Figure 3.5 A schematic of ER,IIR and DIR HTFCs (Choudhury et al., 2013)

3.2   Control Structure Design

In industrial, equipment is inter-connected and operate together in order to achieve the desired process objective such as optimal production of a valuable product. Their complex interactions between equipment lead to numerous inputs and outputs. To reduce the unnecessary control loops and achieve the desired objective of the process, control structure design is necessary to provide an efficient control system. It deals with the structural decisions of the control system, including the selection of manipulated variables (inputs), controlled variables (output), measurements, control configuration, and how to pair the inputs and outputs to form control loops (Skogestad and Postlethwaite, 2005). The self-optimizing control is implemented in the procedure of control structure design to select the good controlled variable which can be kept constant at setpoints without the need to re-optimize when disturbance occur.

The control structure design procedure can follow the stepwise of Skogestad (2004). The procedure consists of two main parts: Top-down and Bottom-up. Top-down is a selection of controlled outputs, measurements and inputs. This part is mainly focus on economic steady-state optimal operation. Bottom-up is a design of the control system including the selection of control configuration, the most important decision. This part is dynamic considerations focusing on the control layer structure. The steps of control structure design are shown as follow:

Step 1. Define operational objectives.

The operational objective in term of a scalar cost function *J* which should be minimized is defined. Notably, fixed costs and capital costs should not be included in the cost function *J* because they are not affected by the plant operation on the timescale of 1 hour. Moreover, the minimized cost function J must subject to satisfying the defined operational, safety and environmental constraints.

The general operational objective function is defined as *J (u, x, d)*. The variable *u* refers to the steady-state degrees of freedom, *x* refers to state variables, and *d* refers to disturbances. The operational objective function *J* is minimized with respect to *u* for given *d* can be formulated as:

$$\min_{u} \quad J(x, u, d) \tag{3.7}$$

Subject to: model equations: $f(x, u, d) = 0$ (3.8)

operational constraints: $g(x, u, d) \le 0$ (3.9)

Step 2. Identify steady-state degrees of freedom and determine the optimal steady-state operation conditions, including active constraints.

The dynamic and steady-state degrees of freedom (DOF) are identified. The number of control variables is equal to the number of steady-state degrees of freedom, N_{ss} and can be calculated from Equation (3.10).

$$N_{SS} = N_{valves} - N_{0SS} - N_{specs} \tag{3.10}$$

where N_{valves} represents the numbers of dynamic DOFs (counting all valves in the system) that is equal to the number of manipulated variables, N_{0SS} represents the is the number of valves with no steady-state effect, and N_{specs} represents the number of specified conditions. Next, the task is to identify the active constraints resulting of the disturbance changes. Note that active constraints may change with disturbances resulting in different active constraint regions.

Step 3. Selection of primary controlled variables.

To make use of all the economic degrees of freedom (inputs, *u*), economic control variables (CV₁) need to be identified as many as we have inputs (*u*). However, which variables should be controlled to maintain a close-to-optimal economic

operation in-spite of disturbances? According to rule 1 and 2 of Minasidis et al. (2015), we need to control the active constraints variable and control self-optimizing variable (if any remaining unconstrained steady-state degrees of freedom). The variable needed to remain constant is active constraint. Self-optimizing variables are controlled variables which their optimal values are insensitive to disturbances. Self-optimizing control is achieved an acceptable loss L (without the need to reoptimize when disturbances occur) with constant setpoint values for the controlled variables. The concept of self-optimizing control can be shown in **Figure 3.6**. The loss L is defined as the difference between the actual value of the cost function ($J(u,d)$) and the optimal value ($J_{opt}(u,d)$) and can be express as:

$$L = J(u,d) - J(u_{opt}, d) \tag{3.11}$$

Loss L imposed by keeping constant setpoint for the controlled variable rather than reoptimizing when disturbance occur. For the case as shown in **Figure 3.6**, $C_{1,s}$ is better self-optimizing controlled variable than $C_{2,s}$ (a smaller loss). d* represents its nominal optimal operating point.
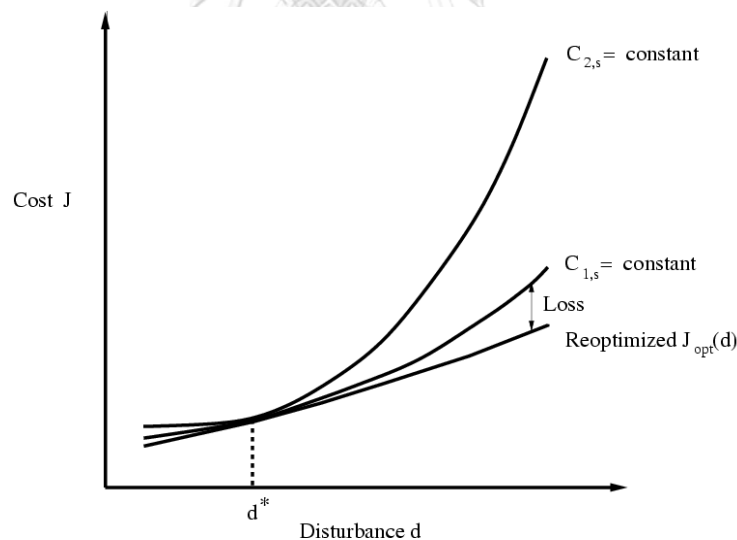
Figure 3.6 The concept of self-optimizing control

Step 4. Determine where in the plant to set the production rate.

The production rate is determined by specifying one degree of freedom, an inlet to the process, which is referred as the throughput manipulator (TPM). In

another word, the TPM is the manipulated variable used to control throughput (controlled variable) or a degree of freedom that affects the network flow. Location of the TPM is an importance decision that links the top-down and bottom-up parts together. For TPM location see Rules 4 and 5 in **Table 3.4**.

Step 5. Select structure of regulatory (stabilizing) control layer.

The objective of the regulatory control layer is to "stabilize" the process. The "stabilized" process means it does not drift too far from acceptable operation when there are disturbances. In this step, all the drifting process variables are selected to be controlled to ensure safe and stable process operation. Moreover, these measurements are pairing with the manipulated variables according to pair close rule (**Table 3.4**). The good secondary measurements should select the variables that easy to measure and control using the available manipulated variables.

Step 6. Select supervisory control layer.

The controlled outputs are kept at optimal setpoints, using the setpoints to the regulatory layer in addition to any remaining valves. Decentralized or multivariable (usually MPC) control is also decided to implement in this step. For decentralized (single-loop) control may use simple PI or PID controllers, however, it is preferred for non-interacting process. The relative gain array (RGA) is considered a controllability index for the selection of input-output pairings and to describe the interactions among inputs and outputs (see APPENDIX A.).

Step 7. Online optimization layer (RTO).

This step has task to update the setpoints for CV_1 and to detect change in the active constraint regions that require changing the CV_1. Real-time optimization (RTO) layer gives little benefit and should not be used if the active constraints do not change and good self-optimizing controlled variables can be found. In fact, RTO is costly in the sense that it requires a detailed steady-state computer model to be maintained and continuously updated. Hence, RTO is not available in some plants.

Table 3.4 Rules for control structure design (Minasidis et al., 2015)

Rules	For step	details
Rule 1	Step 3	Control active constraints
Rule 2	Step 3	Control the self-optimizing variables for remaining unconstrained steady-state degrees of freedom (if any)
Rule 3	Step 3	Never try to control the cost function J (or any other variable that reaches a maximum or minimum at the optimal operating point) for remaining unconstrained steady-state degrees of freedom (if any)
Rule 4	Step 4	Locate the TPM close to the process bottleneck
Rule 5	Step 4	Locate the TPM inside the recycle loop for processes with recycle.
Rule 6	Step 5	Arrange the inventory control loops around the TPM location according to the radiation rule.
Rule 7	Step 5	Select sensitive/drifting variables as controlled variables CV_2 for regulatory control
Rule 8	Step 5	Economically important active constraints should be selected as controlled variables CV_2 in the regulatory layer
Rule 9	Step 5	Pair-close rule: The pairings should be selected such that, effective delays and loop interactions are minimal.
Rule 10	Step 5	Avoid using MVs that may optimally saturate (at steady state) to control CVs in CV_2
Rule 11	Step 6	MVs that may optimally saturate (at steady state) should be paired with the subset of CV_1 that may be given up.

3.3   Gas Turbine

The gas turbine is an internal combustion engine that uses air as the working fluid. The engine extracts chemical energy from fuel and converts it to mechanical energy using the gaseous energy of the working fluid (air) to drive the engine to produce the electricity.

High-temperature fuel cells and gas turbines are thermally well matched because the operating temperature of high-temperature fuel cells and the turbine inlet temperature for micro-gas turbine are in a similar temperature range: 700-1000 °C. Microturbines (**Figure 3.7**) is a small gas turbine that produces between 25 kW and 500 kW of power. The overview of Microturbines is shown in **Table 3.5**
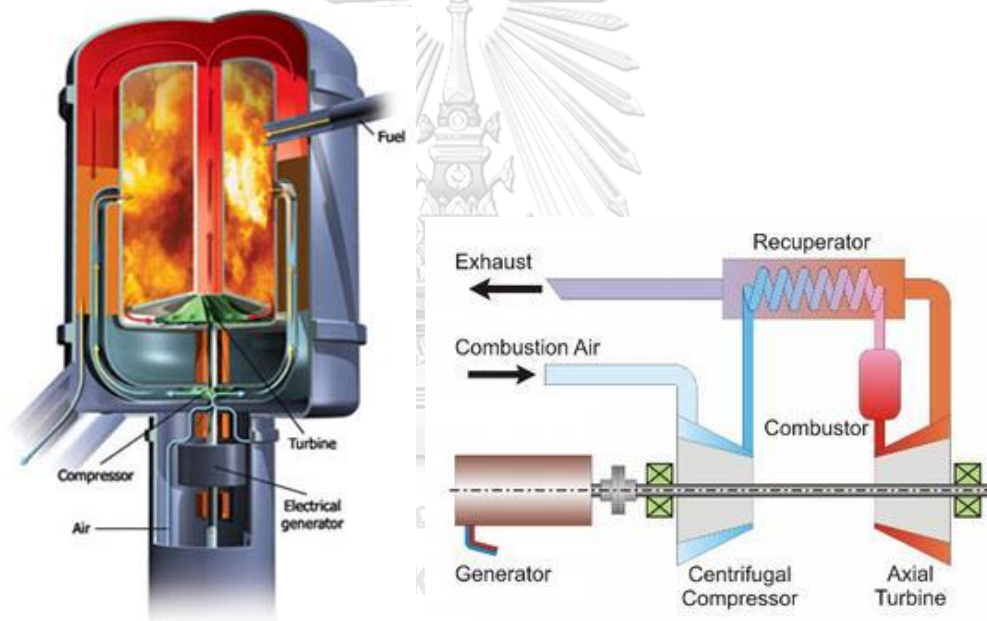
Figure 3.7 A micro-gas turbine.

(http://www.wbdg.org/resources/microturbines.php)

Air passes through a gas turbine engine, aerodynamic and energy requirements demand changes in the air's velocity and pressure. During compression, a rise in the air pressure is required, but not an increase in its velocity. After compression and combustion have heated the air, an increase in the velocity of gases is necessary for the turbine rotors to develop power. The size and shape of the ducts through which the air flows affect these various changes. Where a conversion from velocity to pressure

is required, the passages are divergent. Conversely, if a conversion from pressure to velocity is needed, a convergent duct is used.

Table 3.5 Microturbine Overview

Size range	25-500 kW
Fuel	Natural gas, hydrogen, propane, diesel
Efficiency	15% (Unrecuperated)
	20-30% (Recuperated)
	Up to 85% (With heat recovery)
Environmental	Low (<9-50 ppm) NO_x
Commercial status	Small volume production, commercial prototypes now.

3.3.1 Compression

Following **Figure 3.8**, the ideal gas is compressed from P_1 to P_2 resulting in a temperature increase from T_1 to T_2. The actual temperature depends on the assumptions of the actual compression process.
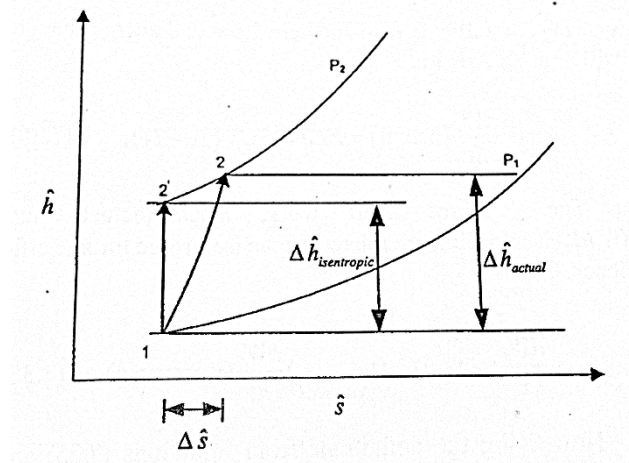
Figure 3.8 Enthalpy-entropy diagram for the compression process

For the adiabatic process ($dQ/dt = 0$) (assuming ideal gas system or constant heat capacity system and well-designed compressor), the energy balance will be as Equation (3.12)

$$-\frac{dW_s}{dt} = \dot{m}\Delta h = \dot{m}C_P^{ig}\left(T_2 - T_1\right) \tag{3.12}$$

where dW_s/dt is the rate of shaft work done by the system to the surroundings and h is the enthalpy per unit mass.

For compressors, shaft work will be required from the surroundings as an energy input ($dW_s/dt < 0$). This results in $T_2 > T_1$ for compression process.

Isentropic process is often assumed (ideal gas). The temperature that causes by the isentropic compression or expansion of an ideal gas with constant heat capacity from (P_1, T_1) to P_2 is described in (3.13).

$$T_2^{isen} = T_1 \left(\frac{P_2}{P_1} \right)^{(\gamma-1)/\gamma} \tag{3.13}$$

Where γ is the specific heat ratio defined as following:

$$\frac{C_P^{ig}}{C_V^{ig}} = \frac{C_P^{ig}}{C_V^{ig}} = \gamma \tag{3.14}$$

Hence, the energy balance will be as Equation (3.15).

$$-\frac{dW_s}{dt}(isentropic) = \dot{m}\Delta h = \dot{m}C_P^{ig} \left(T_1 \left(\frac{P_2}{P_1} \right)^{(\gamma-1)/\gamma} - T_1 \right) \tag{3.15}$$

The process from 1 to 2' is isentropic and this changes in energy given by $\Delta h_{isentropic}$. The actual system path will be 1 to 2 and the actual energy change will be Δh_{actual}.

$$-\frac{dW_s}{dt}(actual) = \dot{m}\Delta h = \dot{m}C_P^{ig} \left(T_2 - T_1 \right) \tag{3.16}$$

The isentropic compressor efficiency $\eta_{isen,com}$ is used to describe the correlation between the actual rate of shaft work and the isentropic rate of shaft work:

$$\frac{dW_s}{dt}(actual) = \frac{\frac{dW_s}{dt}(isentropic)}{\eta_{isen,com}} \tag{3.17}$$

After rearrangement, the temperature results from the isentropic compression will be

$$T_2 = T_2(actual) = T_1 \left\{ 1 + \frac{1}{\eta_{isen,com}} \left[\left(\frac{P_2}{P_1} \right)^{(\gamma-1)/\gamma} - 1 \right] \right\} \tag{3.18}$$

3.3.2 Combustion chamber

In this section, energy will be added to the working fluid by igniting the fuel in the chamber. For an ideal gases system, the mass and energy balance are

$$\dot{m}_g = \dot{m}_a + \dot{m}_f \tag{3.19}$$

$$\dot{m}_a \hat{C}_{P,a}^{ig} \Delta T_2 + \dot{m}_f LHV = (\dot{m}_a + \dot{m}_f) \hat{C}_{P,g}^{ig} \Delta T_3 + \dot{m}_f LHV(1-\eta_c) \tag{3.20}$$

Where T_{ref} is at 25 ºC (298.15 K) and η_c is a combustion chamber efficiency.

3.3.3 Expansion

The gas with high-temperature and high-energy will expand through a turbine and power will be extracted. Fundamentally, the heat from the combustion process is converted to shaft work.

For the expansion process, enthalpy-entropy diagram will be as shown in **Figure 3.9** Enthalpy-entropy diagram for the expansion process, the exhaust gas from the combustion chamber is expanded (P_3 to P_4) in turbine resulting in a temperature decrease (T_3 to T_4). For an adiabatic system or a constant heat capacity system, the energy balance will be

$$-\frac{dW_s}{dt} = F\Delta h = F\hat{C}_P^{ig}(T_4 - T_3) \tag{3.21}$$
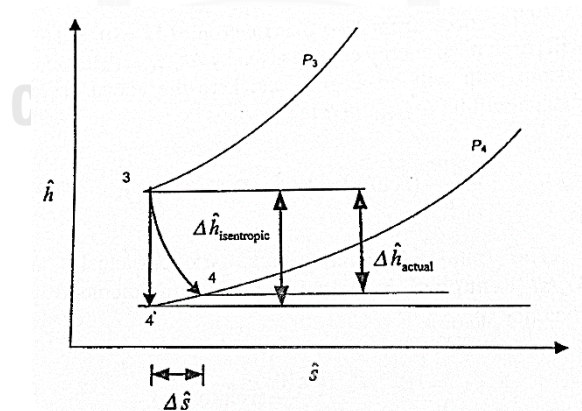
Figure 3.9 Enthalpy-entropy diagram for the expansion process

For turbine, shaft work will be generated by the process ($dW_s / dt > 0$). This can be observed as $T_3 > T_4$ for expansion process.

Isentropic process is assumed. The energy balance will be as:

$$-\frac{dW_s}{dt}(isentropic) = F\Delta h = FC_P^{ig}\left(T_3\left(\frac{P_4}{P_3}\right)^{(\gamma-1)/\gamma} - T_3\right) \tag{3.22}$$

The process from 3 to 4' is isentropic with an energy change $\Delta h_{isentropic}$. The actual system path is 3 to 4 and the actual energy change will be Δh_{actual}.

$$-\frac{dW_s}{dt}(actual) = F\Delta h = FC_P^{ig}\left(T_4 - T_3\right) \tag{3.23}$$

The isentropic turbine efficiency $\eta_{isen,\,ex}$ is used to describe the correlation between the actual rate of shaft work and the isentropic rate of shaft work:

$$\frac{dW_s}{dt}(actual) = \eta_{isen,ex}\frac{dW_s}{dt}(isentropic) \tag{3.24}$$

After rearrangement, the temperature results from the isentropic expansion will be

$$T_4 = T_4(actual) = T_3\left\{1 + \eta_{isen,ex}\left[\left(\frac{P_4}{P_3}\right)^{(\gamma-1)/\gamma} - 1\right]\right\} \tag{3.25}$$

The gas turbine engine has a task to produce usable output shaft power to drive the generator. In addition, it must also provide power to drive the compressor. A large mass of air is required to be supplied by the compressor to the turbine in order to produce the necessary power.

3.4   Compressed Air Energy Storage

Energy storage means a formation of energy in difference styles which can be drawn in the future to perform some useful operations, for example a power supply and batteries. However, the electrical energy generally requires its conversion into another form of energy. The converted energy form is widely used to classify the energy storage system (ESS) which may be divided into 5 main categories: chemical, electrochemical, electrical, mechanical and thermal energy storage.

Compressed air energy storage (CAES) system is a mechanical energy storage system. The concept of CAES is rather simple. The air storage is charged by the use of electrically driven compressors, that convert the electric energy into potential energy of pressurized air. The pressurized air in the storage can be released upon the demand to generate electricity by air expansion through an air turbine. Three main components used in CAES system are compressor, air storage reservoir, and expander. CAES have been mainly applied to the system which require air. A CAES system schematic is shown in **Figure 3.10**.
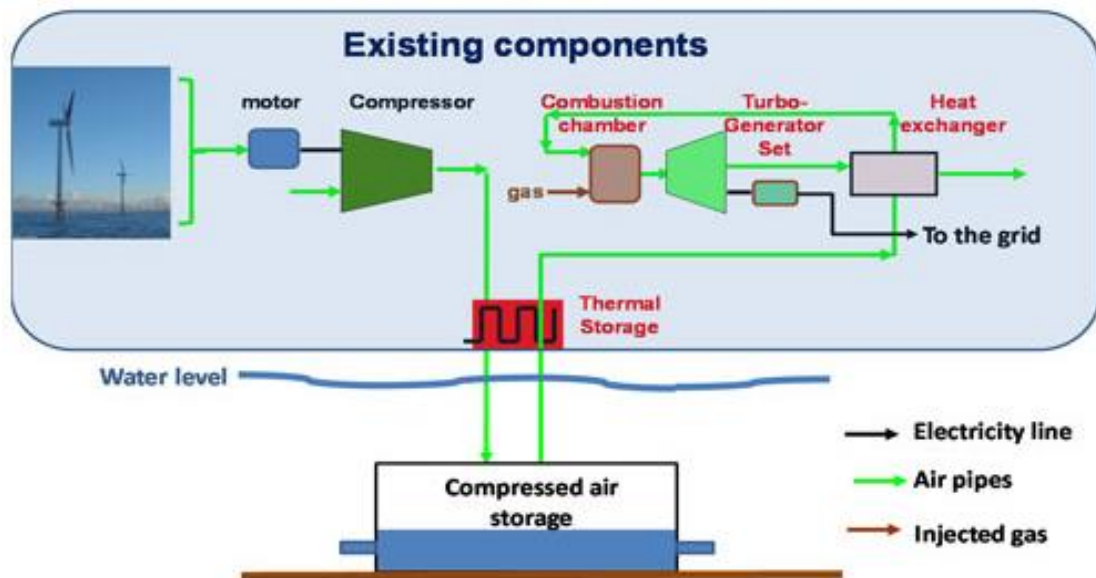
Figure 3.10 A CAES system schematic

(https://www.greenprophet.com/2012/07/arothrons-underwater-compressed-air/)

The advance adiabatic CAES (AA-CAES) is a second-generation with the aim of minimizing the use of fuels for firing. The thermal energy storage (TES) is implementing into A-CAES to be the heat source instead of firing fuels. The simplified AA-CAES process scheme is shown in **Figure 3.11**. In AA-CAES, the ambient air is compressed, and the heat of compression is then captured in the TES. The stored heat is reused during the discharging process. The compressed air can be stored either at isochoric or at isobaric (**Figure 3.12**). For isochoric case, the pressure is the state of charge whereas the volume indicates the state of charge in isobaric case. The main drawback of isochoric compress air storage is their effect on the compression and expansion machinery due to the changing pressure and therefore the operations of machines are not in their design pressure ratio. Isobaric storage volumes do not have any of those effects but are more complex and not widespread.
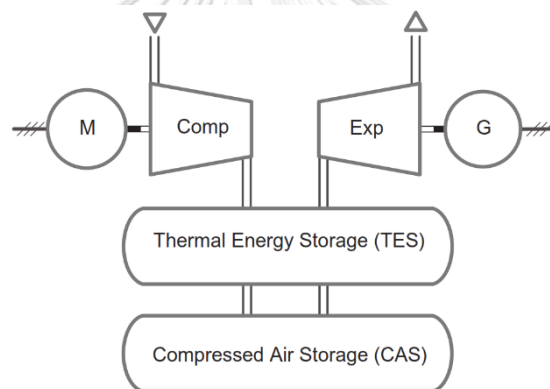
Figure 3.11 Simplified AA-CAES process scheme
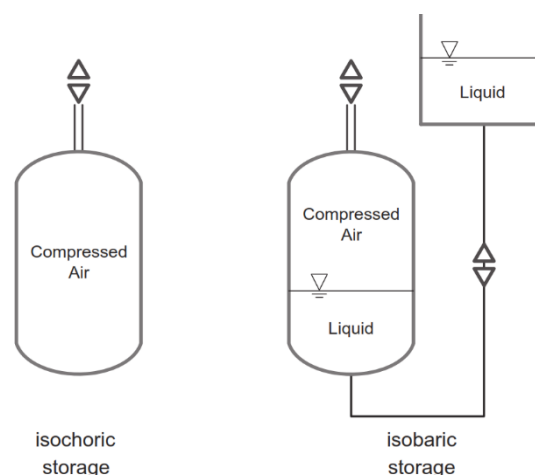
Figure 3.12 Types of air storage devices

CHAPTER 4

MATHEMATICAL MODEL

A mathematical model is an essential tool in the design and optimization of the process system. Fuel cell has no exception. It is helpful for fuel cell developers to improve the design or reduce the drawback. The model should be robust and accurate enough to provide solutions under a wide range of operating conditions. Consequently, this part is concerned with the process model using in this research. In this chapter, it will describe fuel cell models (SOFC and MCFC), GT and AA-CAES, respectively.

4.1 Fuel Cell Models

In CHAPTER 5 and CHAPTER 6 (analysis and design parts), they are studied at steady-state isothermal conditions. For CHAPTER 7, it is performed in dynamic environment to study control structure design. CHAPTER 8 is studied under steady-state non-isothermal condition.

4.1.1 System configuration

Both the SOFC and MCFC are modeled in a planar configuration with co-flow direction of fuel and air (**Figure 4.1**). The SOFC consists of a Ni-YSZ anode, a YSZ electrolyte and a YSZ-LSM cathode. In the MCFC, a Ni-alloy is used as the anode, Li_2CO_3/Na_2CO_3 is used as the electrolyte, and NiO is used as the cathode. The structure of the fuel cell is generally divided into a fuel channel, an air channel, a PEN structure (anode-electrolyte-cathode) and interconnects as shown in **Figure 4.2**. The dimensions of both cells are shown in **Table 4.1**. The fuel (methane) and steam are fed to the reformer to pre-reform the gas at 10% pre-reforming with steam to carbon (S/C) ratio of 2 under 1 atm and 973 K (normal operation). The reformed gas from the reformer is fed to fuel channel which is adjacent to the anode. Air and carbon dioxide (only for MCFC) are fed to air channel beside the cathode. The reformed gas is further reformed inside the fuel cells (SOFC and MCFC) via steam reforming and water-gas-shift reactions (Equations (4.1) and (4.2) in

Table 4.2). H₂ is used to generate electricity via electrochemical reactions as shown
in Equations (4.3) - (4.8) in

Table 4.2.
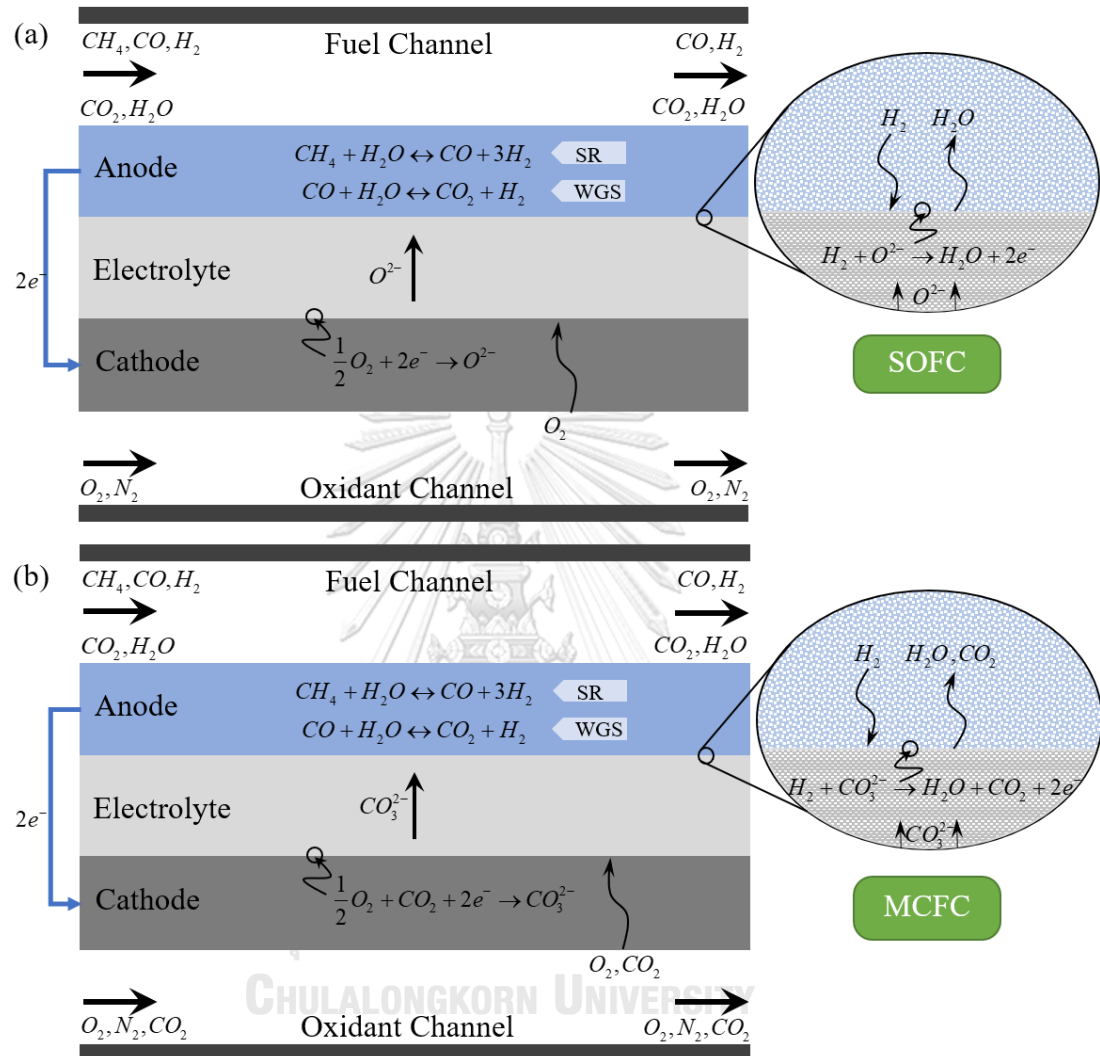
Figure 4.1 Schematics of planar SOFC (a) and MCFC (b) operation
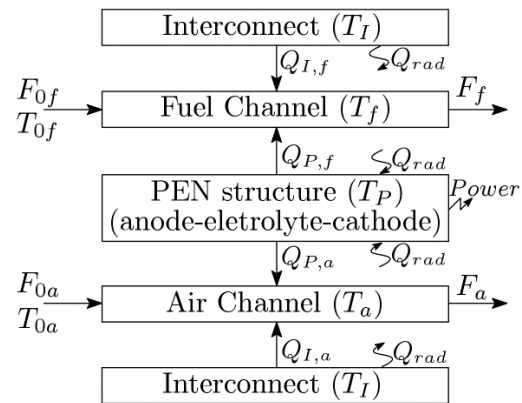
Figure 4.2 the mass and heat balances in fuel cell components
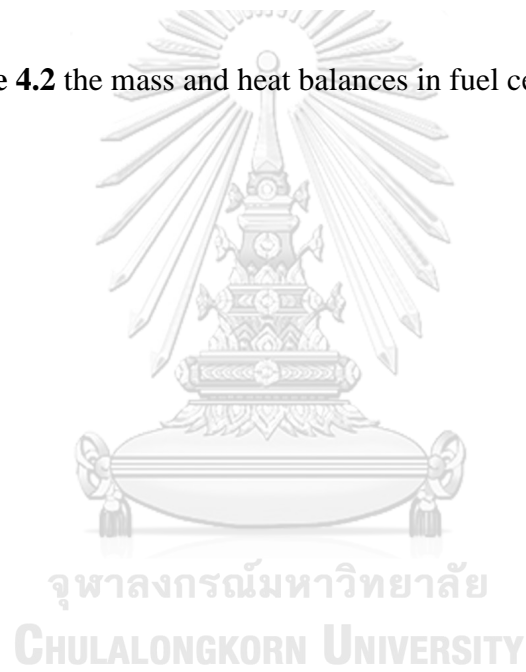
Table 4.1 Structural parameters

	SOFC	MCFC
	(Aguiar et al., 2004)	(Liu and Weng, 2010)
Cell length, L (m)	0.4	0.4
Cell width, W (m)	0.1	0.8
Fuel channel height, h_f (mm)	1	0.8
Air channel height, h_a (mm)	1	0.8
Anode thickness, τ_a (μm)	500	-
Cathode thickness, τ_c (μm)	50	-
Electrolyte thickness, τ_e (μm)	20	-
PEN thickness, τ_{PEN} (μm)	570	1000

Table 4.2 Reactions that occurred in the fuel cell.

Steam reforming reaction (SR)

$$CH_4 + H_2O \leftrightarrow 3H_2 + CO \qquad (4.1)$$

Water-gas-shift reaction (WGS)

$$CO + H_2O \leftrightarrow H_2 + CO_2 \qquad (4.2)$$

SOFC

Oxidation reaction (anode)

$$H_2 + O^{2-} \rightarrow H_2O + 2e^- \qquad (4.3)$$

Reduction reaction (cathode)

$$0.5O_2 + 2e^- \rightarrow O^{2-} \qquad (4.4)$$

Overall electrochemical reaction

$$H_{2,(an)} + 0.5O_{2,(ca)} \rightarrow H_2O_{,(an)} \qquad (4.5)$$

MCFC

Oxidation reaction (anode)

$$H_2 + CO_3^{2-} \rightarrow H_2O + CO_2 + 2e^- \qquad (4.6)$$

Reduction reaction (cathode)

$$0.5O_2 + CO_2 + 2e^- \rightarrow CO_3^{2-} \qquad (4.7)$$

Overall electrochemical reaction

$$H_{2,(an)} + 0.5O_{2,(ca)} + CO_{2,(ca)} \rightarrow CO_{2,(an)} + H_2O_{,(an)} \qquad (4.8)$$

4.1.2 Model assumption

The fuel cell structure is a composite of 4 components; a fuel channel, an air channel, a PEN structure (anode-electrolyte-cathode) and interconnects as shown in **Figure 4.2**. Each component is considered to be lumped model as in the work of (Georgis et al., 2011). They asserted that lumped models are sufficiently accurate for analysis and control of fuel cell systems. The models are based on the following assumptions:

(1) pressure drop inside the channels is neglected

(2) heat loss to the surroundings is neglected

(3) all gases behave as ideal gases

(4) only hydrogen oxidation is considered

(5) heat capacity changes are negligible

There are three reactions taken into account in the fuel channel: methane steam reforming that is methane directly reformed within fuel cells, water gas-shift which is carbon monoxide reacted with water to produce hydrogen and carbon dioxide, and oxidation reaction. In the air channel, only reduction reaction is considered. All these reactions used in the mass and energy balances are presented in **Table 4.2**.

As mentioned above, steam reforming is an endothermic reaction of steam with the fuel in the presence of a catalyst to produce hydrogen and carbon monoxide. The rate expression of steam reforming reaction for the SOFC, $R_{SR,S}$ in a nickel cermet is written as Equation (4.9) (Achenbach, 1994) and for the MCFC, $R_{SR,M}$ in a nickel based alloy is written as Equation (4.10) (Ovrum and Dimopoulos, 2012).

$$R_{\text{SR,S}} = k_0 p_{\text{CH}_4} \exp\left(-\frac{E_a}{\Re T_P}\right) \tag{4.9}$$

where k_0 is a pre-exponential constant and equal to 4274 mol s^{-1} and E_a an activation energy equal to 82 kJ mol^{-1}, respectively.

$$R_{\text{SR,M}} = \exp\left[84.4\left(\frac{1}{2.929} - \frac{T^0}{T_P}\right)\right] \times \left(y_{\text{CH}_4} y_{\text{H}_2\text{O}} - \frac{y_{\text{CO}} y_{\text{H}_2}^3}{K_{\text{SR}}}\right) \times \frac{25}{LW} \tag{4.10}$$

$$K_{SR} = \exp\left(30.19 - 90.41\frac{T^0}{T_P}\right) \tag{4.11}$$

Excess steam is used to prevent carbon formation on the catalyst and to force the reaction to completion. An associated reaction to the reforming reaction is the water-gas shift reaction. Unlike the steam reforming reaction, the water gas-shift reaction is exothermic reaction. The rate expression of water gas shift reaction for the SOFC, $R_{WGS,S}$ is written as Equation (4.12) (Haberman and Young, 2004) and for the MCFC is written as Equation (4.15) (Ovrum and Dimopoulos, 2012).

$$R_{WGS,S} = k_{WGSR}\, p_{CO}\left(1 - \frac{p_{CO_2}\, p_{H_2}/p_{CO}\, p_{H_2O}}{K_{eq}}\right) \tag{4.12}$$

$$k_{WGSR} = 0.0171\exp\left(-\frac{103191}{\Re T_P}\right) \tag{4.13}$$

$$K_{eq} = \exp\left(\frac{4276}{T_P} - 3.961\right) \tag{4.14}$$

$$R_{SR,M} = \exp\left[6.2\left(\frac{1}{2.929} - \frac{T^0}{T_P}\right)\right] \times \left(y_{CO}\,y_{H_2O} - \frac{y_{CO_2}\,y_{H_2}}{K_{WGS}}\right) \times \frac{100}{LW} \tag{4.15}$$

$$K_{WGS} = \exp\left(-3.97 + 14.57\frac{T^0}{T_P}\right) \tag{4.16}$$

Faraday's law relates the flux of reactants and products to the electric current arising from an electrochemical reaction. According to this law and when only hydrogen oxidation is present, the local amount of H_2 and O_2 consumed and H_2O produced (in MCFC, CO_2 is also consumed in cathode and produced in anode) through overall cell reaction,(4.5) and (4.8) are related to the electric current density, j, produced in the cell by:

$$R_{E,S/M} = \left(\frac{j}{2F}\right) \tag{4.17}$$

4.1.3 Mass Balance

Mass balances are included in the fuel and air channels but not in the PEN structure and the interconnect (between each individual cell). The chemical species

considered in the fuel channel include CH_4, H_2O, CO, H_2, and CO_2 while O_2 and N_2 (including CO_2 and H_2O for the MCFC) are considered in the air channel. The fuel and air channel mass balances can be defined in term the mole of component, as shown below:

$$\frac{dN_i}{dt} \underset{=0\ for\ Ch.5,6}{} + \underset{=F_i-F_{0i}\ for\ Ch.7,8}{L\frac{dF_i}{dx}} = \sum_j v_{i,j}R_jA \qquad (4.18)$$

Boundary condition:

$$F_i\big|_{t=0} = F_{ss,i} \qquad (4.19)$$

where F (mol s^{-1}) are the molar flow rate of species i in the fuel and air channels, $v_{i,j}$ is the stoichiometric coefficient of component i in reaction j, R_j (mol s^{-1} m^{-2}) is the rate of reaction j (j = SR, WGS and E for fuel channel and j = E for air channel), and A is the reaction area (m^2).

4.1.4 Energy Balance

Energy balances are included in all fuel cell components. Radiation heat between the PEN structure and the interconnect is considered due to high-temperature operation. In the PEN structure, electrochemical reaction heat and power generation heat losses are considered here. The signs of heat in and out of the system are shown in **Figure 4.2**. Energy balance of each component are shown as below:

Fuel channel:

$$\rho_f Cp_f V_f \frac{dT_f}{dt} = H_{0f} - H_f + Q_{P,f} + Q_{I,f} + \sum_{j\in\{SR,WGS\}} \left(-\Delta H\right)_j R_j A \qquad (4.20)$$

Air channel:

$$\rho_a Cp_a V_a \frac{dT_a}{dt} = H_{0a} - H_a + Q_{P,a} + Q_{I,a} \qquad (4.21)$$

PEN structure:

$$\rho_P Cp_P V_P \frac{dT_P}{dt} = -Q_{P,f} - Q_{P,a} + Q_{rad} - jEA + \left(-\Delta H\right)_{\mathrm{E}} R_{\mathrm{E}} A \qquad (4.22)$$

Interconnect:

$$\rho_I Cp_I V_I \frac{dT_I}{dt} = -Q_{I,f} - Q_{I,a} - Q_{rad} \qquad (4.23)$$

Here

Enthalpy flow in streams: $H_k = \sum_i F_i \int_{298}^{T_k} Cp_i dT \quad k \in \{0f, 0a, f, a\}$ (4.24)

Heat conduction: $Q_{P/I} = A\langle h\rangle(T_{P/I} - T_k) = \dfrac{Ak_k Nu(T_{P/I} - T_k)}{D_h}$ (4.25)

Heat radiation: $Q_{rad} = A\left(\dfrac{\sigma(T_I^4 - T_P^4)}{1/\in_I + 1/\in_P - 1}\right)$ (4.26)

where Cp_i (kJ kmol^{-1} K^{-1}) is heat capacity of gas i, heat conduction ($Q_{P/I}$, kW) relies on Fourier's law with a constant Nusselt number, Nu, (Aguiar et al., 2004), k_k (kJ m^{-1} s^{-1} K^{-1}) is thermal conductivity of gas steam k, D_h (m) is hydraulic diameter of a rectangular cross-section gas channel, σ (W m^{-2} K^{-4}) is Stefan–Boltzmann constant, and $\in_k$ is emissivity of solid component k.

In the CHAPTER 5 and CHAPTER 6, the isothermal operation is additionally assumed to study the effect of implementation of the MCFC in the SOFC system. Hence, the amount of energy required for operating the fuel cells under isothermal conditions can be calculated by the energy balance around the SOFC and the MCFC as shown in Equation (4.27).

$$\dot{Q} = \sum_{i=1}^{n} F_i h_i - \sum_{i=1}^{n} F_{0i} h_{0i} + P_W$$ (4.27)

where h_i (kJ mol^{-1}) is enthalpy of gas i and P_w (kW) is power generated by fuel cell W.

4.1.5 Electrochemical model

4.1.5.1 SOFC

The theoretical open circuit voltage is the maximum voltage that can be calculated by Nernst equation as shown in Equation (4.28). The operating cell voltage is less than the open circuit voltage due to internal losses inside the cells. Internal loss inside the SOFC can be divided into three types: activation overpotentials, ohmic loss and concentration overpotentials. The voltage of an operating cell is given by subtracting the voltage drops due to the various losses from the theoretical open circuit voltage:

$$E_{OCV,S} = E^0 - \frac{\Re T}{2F} \ln\left(\frac{p_{H_2O}}{p_{H_2} \, p_{O_2}^{0.5}} \right) \qquad (4.28)$$

$$E = E_{OCV,S} - \sum \eta_{loss} \qquad (4.29)$$

$$\sum \eta_{loss} = \eta_{con} + \eta_{act,an} + \eta_{act,ca} + \eta_{ohm} \qquad (4.30)$$

where E is operating cell voltage, $E_{OCV,S}$ is the open circuit voltage of fuel cell, η_{ohm} is ohmic losses, η_{con} is concentration overpotentials, and η_{act} is activation overpotentials. Three major losses influence the shape of i-V curve that shows the voltage output of the fuel cell for a given current output, as illustrated in **Figure 4.3**.
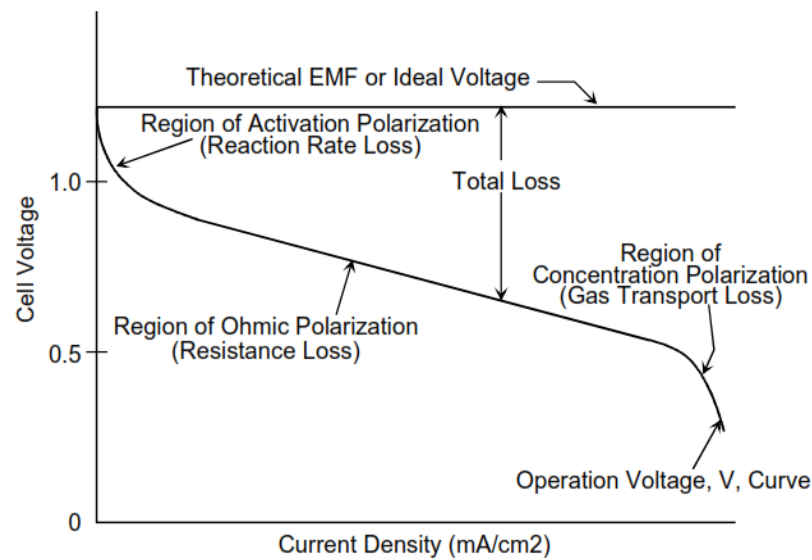
Figure 4.3 a schematic of fuel cell i-V curve (EG&G Technical Services, 2004)

Ohmic losses are caused by transport of oxide ions through the electrolyte, transport of electrons through the electrodes (the cathode and the anode). Ohm's law can describe the ohmic losses that can be expressed:

$$\eta_{ohm} = j \sum_i \frac{\tau_i}{\sigma_i} \qquad (4.31)$$

where j is the current density, τ_i is thicknesses of electrodes and electrolyte and σ_i is conductivities of electrodes and electrolyte. Assumption of Equation (4.31) is negligible contact resistances, cross-plane charge flow, and series connection of resistances. Common methods of reducing ohmic losses include making electrolyte as

thin layer, and employing high conductivity materials, and operating at higher temperatures.

Concentration overpotentials are the result of practical limitations on mass transport within the cell. They can be caused when the reactants are consumed by the electrochemical reaction faster than diffusing into the porous electrode. Moreover, they can also be caused by variation in bulk flow composition because the consumption of reacting species in the reactant flows causes a drop in reactant concentration along the cell, which causes a drop in the local potential near the end of the cell. The occurrences of these losses include gas species transport in electrodes, solution of reactants into the electrolyte, dissolution of products out of the electrolyte and diffusion of the reactants/products through the electrolyte to/from the reaction sites.

These losses involve the difference between the species concentration at the three-phase boundaries (TPB) and the bulk channel flow and current density. The concentration overpotentials can be written as;

$$\eta_{con} = \frac{\Re T}{2F} \ln\left(\frac{p_{H_2O,TPB}\, p_{H_2,f}}{p_{H_2O,f}\, p_{H_2,TPB}} \right) + \frac{\Re T}{4F} \ln\left(\frac{p_{O_2,a}}{p_{O_2,TPB}} \right) \tag{4.32}$$

Equation (4.32) can be divided into the anodic concentration overpotential, $\eta_{con,an}$ occurring on the first term of right-hand side and the cathodic concentration overpotential, $\eta_{con,ca}$ which occurs on the second term of right-hand side.

The partial pressures of H_2, H_2O, and O_2 at the three-phase boundaries can be determined by using porous-media gas-phase transport models as shown in Equations (4.33) - (4.35)

$$p_{H_2,TPB} = p_{H_2,f} - \frac{RT\tau_{an}}{2FD_{eff,an}} j \tag{4.33}$$

$$p_{H_2O,TPB} = p_{H_2O,f} + \frac{RT\tau_{an}}{2FD_{eff,an}} j \tag{4.34}$$

$$p_{O_2,TPB} = P_a - \left(P_a - p_{O_2,a} \right) \exp\left(\frac{RT\tau_{ca}}{4FD_{eff,ca} P_a} j \right) \tag{4.35}$$

where $D_{eff,an}$ and $D_{eff,ca}$ are the average effective diffusion coefficients of the anode and cathode, respectively. It is considered a binary gas mixture of H_2 and H_2O in the anode and of O_2 and N_2 in the cathode, which was proposed by Aguiar et al. (2004). These overpotentials can be mitigated by reducing the reactant utilization fraction or increasing the electrode porosity.

Activation overpotentials occur due to the need of the available energy to break the chemical bonds of hydrogen and oxygen molecules into ions form at the surface of electrodes for using in the electrochemical reaction. It can be determined by the non-linear Butler-Volmer equation as follows:

$$j = j_{0,an}\left[\frac{p_{H_2,TPB}}{p_{H_2,f}}\exp\left(\frac{\alpha nF}{\Re T}\eta_{act,an}\right) - \frac{p_{H_2O,TPB}}{p_{H_2O,f}}\exp\left(-\frac{(1-\alpha)nF}{\Re T}\eta_{act,an}\right) \right] \quad (4.36)$$

$$j = j_{0,ca}\left[\exp\left(\frac{\alpha nF}{\Re T}\eta_{act,ca}\right) - \exp\left(-\frac{(1-\alpha)nF}{\Re T}\eta_{act,ca}\right) \right] \quad (4.37)$$

where α is the transfer coefficient (usually considered to be 0.5), n is the number of electrons transferred in the single elementary rate-limiting reaction step (in this case n = 2), j is the current density, and $j_{0,an}$ and $j_{0,ca}$ are the exchange current densities of the anode and the cathode, as expressed by

$$j_{0,electrode} = \frac{RT}{nF}k_{electrode}\exp\left(-\frac{E_{electrode}}{RT}\right) ; electrode \in \{an, ca\} \quad (4.38)$$

where $E_{eletrode}$ represents the activation energy of the exchange current densities, as 140 kJ mol^{-1} for anode and 137 kJ mol^{-1} for cathode, $k_{electrode}$ represents the pre-exponential factor of the exchange current density, as 6.54 x 10^{11} Ω^{-1}m^{-2} for anode and 2.35x10^{11} Ω^{-1}m^{-2} for cathode, respectively (Aguiar et al., 2004).

Table 4.3 Parameters used in the electrochemical models (Chatrattanawet et al., 2015).

$D_{eff,an}$ (m^{2}s^{-1})	3.66×10^{-5}
$D_{eff,ca}$ (m^{2}s^{-1})	1.37×10^{-5}
σ_{an} (ohm^{-1}m^{-1})	$(9.5 \times 10^7/T)\exp(-1150/T)$
σ_{ca} (ohm^{-1}m^{-1})	$(4.2 \times 10^7/T)\exp(-1200/T)$
σ_{el} (ohm^{-1}m^{-1})	$33.4 \times 10^3 \exp(-10300/T)$

4.1.5.2 MCFC

In a MCFC, electrochemical model is using the general fuel cell theory as using in an SOFC. However, internal loss inside the MCFC usually based on a combined experimental and theoretical approach is defined as the equivalent global resistances which account for all type of losses. Nernst Equation for a MCFC depends on the gas composition and temperature at the electrodes like the SOFC. The Nernst Equation is shown as:

$$E_{\mathrm{OCV,M}} = -\frac{\Delta G}{2F} - \frac{\Re T}{2F} \ln\left(\frac{p_{\mathrm{H_2O}} p_{\mathrm{CO_2},f}}{p_{\mathrm{H_2}} p_{\mathrm{O_2}}^{0.5} p_{\mathrm{CO_2},a}} \right) \tag{4.39}$$

$$E = E_{\mathrm{OCV,M}} - \sum \eta_{\mathrm{loss}} \tag{4.40}$$

$$\sum \eta_{\mathrm{loss}} = \left(R_{ir} + R_{an} + R_{ca} \right) j \tag{4.41}$$

where ΔG (kJ mol^{-1}) is Gibbs free energy change, the subscript f and a denote fuel channel and air channel, respectively. R_{ir}, R_{an} and R_{ca} (Ω cm^2) are equivalent global resistance of the electrolyte, anode and cathode, respectively. The resistance can be expressed as follows (Morita et al., 2002) which Li$_2$CO$_3$/Na$_2$CO$_3$ is considered as electrolyte:

$$R_{ir} = 1.12 \times 10^{-2} \exp\left(\frac{23}{\Re T} \right) \tag{4.42}$$

$$R_a = 2.04 \times 10^{-3} \exp\left(\frac{23.7}{\Re T} \right) p_{\mathrm{H_2}}^{-0.5} \tag{4.43}$$

$$R_c = 3.28 \times 10^{-9} \exp\left(\frac{132}{\Re T}\right) p_{O_2}^{-0.75} p_{CO_2}^{0.5}$$
$$+ 3.39 \times 10^{-6} \exp\left(\frac{67.1}{\Re T}\right) \left(2 \times 10^{-5} y_{H_2O} + y_{CO_2}\right)^{-1}$$

(4.44)

Here, y_i is mole fraction of gas i in cathode.

4.1.6 Performance index

The power density or power output of fuel cell W ($P_{D,W}$; W cm^{-2}) is the amount of power per unit area which is obtained by the product of the operating cell voltage (E) and current density (j), as given by:

$$P_{D,W} = j_W E_W$$

(4.45)

Thus, a cell of fuel cell W can generate power as Equation (4.46) and the generated power from the integrated of a cell of SOFC and MCFC can be computed by Equation (4.47).

$$P_W = P_{D,W} A_W$$

(4.46)

$$P_{sys} = \sum_{W \in \{S,M\}} P_{D,W} A_W$$

(4.47)

In CHAPTER 8, the power generated by the integrated fuel cell system is converted to AC via a DC-AC convertor.

The fuel utilization factor (U_f) is the ratio of the total inlet fuel used to produce electricity in the cell and the inlet fuel flow, and is defined by:

$$U_f = \left(\frac{\dot{m}_{0f} - \dot{m}_f}{\dot{m}_{0f}}\right) = \frac{\dot{m}_{f,consumed}}{\dot{m}_{0f}} = \frac{jA}{2F(4F_{CH_4} + F_{CO} + F_{H_2})}$$

(4.48)

where $\dot{m}_{0f}$ is the mass flow rate of fuel inlet, $\dot{m}_f$ is the mass flow rate of fuel outlet, A is reaction area, F is Faraday constant and F_i is molar flow rate of gas i.

The excess air is another important parameter for the design of the fuel cell system. The air ratio reflects the air excess which is supplied to the cell for cooling and retaining the cell temperature. Therefore, the air utilization factor can be defined as:

$$U_a = \left(\frac{\dot{m}_{0a} - \dot{m}_a}{\dot{m}_{0a}}\right) \times 100\% = \frac{\dot{m}_{a,consumed}}{\dot{m}_{0a}} \times 100\%$$

(4.37)

The air ratio (λ_{air}) is the inverse of the air utilization factor, which is defined as:

$$\lambda_{air} = \frac{1}{U_a} = \frac{F_{0O_2}}{jA/4F} \tag{4.38}$$

For energy conversion device, the efficiency of a system is great importance. Fuel cell electrical efficiency represents the capability of the total chemical energy in the inlet fuel which is converted into electricity. Electrical efficiency of a fuel cell W can be calculated from thermal energy of fuel fed in the cell that are methane, carbon monoxide, and hydrogen, as described below:

$$\eta_{ele,W} = \frac{P_W}{F_{0CH_4}LHV_{CH_4} + F_{0H_2}LHV_{H_2} + F_{0CO}LHV_{CO}} \quad W \in \{S, M, sys\} \tag{4.49}$$

The thermal efficiency (η_{th}) is defined in terms of the amount of energy input (LHV basis) that can be converted to a net thermal energy of the system as:

$$\eta_{th,W} = \frac{Q_{gen} - Q_{use}}{F_{0CH_4}LHV_{CH_4} + F_{0H_2}LHV_{H_2} + F_{0CO}LHV_{CO}} \quad W \in \{S, M, sys\} \tag{4.50}$$

Power generated per feed used is also commonly used in comparison of the power generation to show amount of power generated with the same amount of fuel feed as shown in Equation (4.51).

$$En_W = P_W / F_{0CH_4} \quad W \in \{S, M, sys\} \tag{4.51}$$

In power generation process, carbon dioxide emission coefficient (CEC) is used as indicator to measure amount of CO_2 released (Equation (4.52)) because ways to reduce CO_2 emission usually require energy to extract CO_2 out of the exhaust stream.

$$CEC_W = \dot{m}_{CO_2} / P_W \tag{4.52}$$

4.1.7 Model validation

The electrochemical model is used for the computation of the fuel cell voltage, current density, and power density. The model reliability has been examined by comparing the predicted results with the experimental data of Zhao and Virkar (2005) for the SOFC and that of Milewski et al. (2013) for the MCFC.

Figure 4.4 shows the operating voltages of the SOFC (a) and MCFC (b) predicted from the model, compared with the experimental data as a function of current densities at different operating temperatures. **Table 4.4** - **Table 4.7** show the values of operating parameters used for model validation. It is observed that the simulations show good agreement with the experimental data of the MCFC and SOFC at 1073 K. The error between the simulation and experimental data may be due to the assumption of the constant for the diffusion coefficients and the activation energy in the electrodes to simplify the model even though they are functions of temperature. The error in the results of the SOFC at a low current density and temperature are evident. The activation and concentration overpotentials based on the used model parameters are overestimated at low temperatures and current densities. Because the simulation showed similar trends to the experimental data, this error ($< 10\%$) is deemed acceptable.
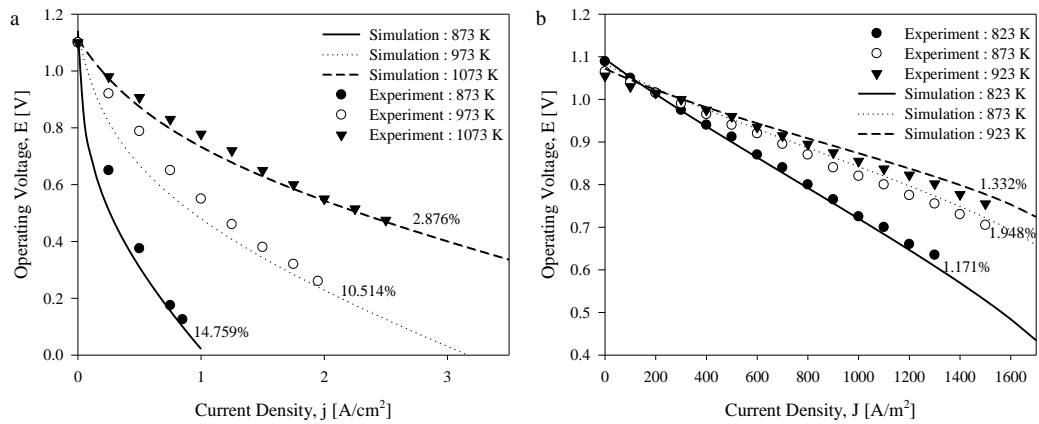
Figure 4.4 Comparison of the simulations and the experimental results of the SOFC
(a) and the MCFC (b).

Table 4.4 SOFC operating conditions for model validation (Zhao and Virkar, 2005)

Symbol	Representation	Value	Unit
P	Pressure	1	bar
T	cell temperature	873, 973, 1073	K
Fuel feed		97% H_2, 3% H_2O	
Air feed		21% O_2, 79% N_2	

Table 4.5 SOFC structure parameters for model validation (Zhao and Virkar, 2005)

Symbol	Representation	Value	Unit
τ_{an}	anode thickness	1000	μm
τ_{ca}	cathode thickness	20	μm
τ_{el}	electrolyte thickness	8	μm
h_f	fuel channel height	1	mm
h_a	air channel height	1	mm
L	cell length	0.4	m
W	cell width	0.1	m

Table 4.6 MCFC operating conditions for model validation (Milewski et al., 2013)

Symbol	Representation	Value	Unit
P	Pressure	1	atm
T	cell temperature	823, 873, 923	K
Fuel feed		70% H_2, 13% H_2O, 17% CO_2	
Air feed		15% O_2, 55% N_2, 30% CO_2	

Table 4.7 MCFC structure parameters for model validation (Milewski et al., 2013)

Symbol	Representation	Value	Unit
τ_{an}	anode thickness	0.76	mm
τ_{ca}	cathode thickness	0.7	mm
τ_{el}	electrolyte thickness	0.9	mm
L	cell length	10	cm
W	cell width	10	cm

จุฬาลงกรณ์มหาวิทยาลัย

CHULALONGKORN UNIVERSITY

4.2 Gas Turbine and Compressed Air Energy Storage Models

Gas turbine (GT) and advance adiabatic compressed air energy storage (AA-CAES) are implemented into the proposed integrated fuel cell system for coping with load variation in CHAPTER 8. The AA-CAES system includes a CAES system and TES technology. The assumptions for the GT and AA-CAES system are as follows:

(1) the compression and expansion are considered as an isentropic process

(2) air is a binary ideal dry gas and its specific heat capacity is considered to be constant

(3) the storage vessel is well insulated with no heat loss across the vessel

(4) complete combustion occurs in the combustion chamber (this assumption also applies to the afterburner).

(5) heat capacity changes are negligible

The parameters related to the GT and the AA-CAES system calculations are listed in **Table 4.8**.

Table 4.8 Parameters of the gas turbine (GT), compressor, turbine, and storages

Specific heat capacity of the heat transfer oil, Cp_{TES} (J kg^{-1} K^{-1})	2200
Isentropic efficiency of the turbine (%)	82
Isentropic efficiency of the compressor (%)	82
combustion process efficiency (%)	98
Thermal energy storage (TES) efficiency (%)	85
DC-AC inverter efficiency (%)	94
Generator mechanical efficiency (%)	94

The electricity consumed by the compressor can be calculated from Equation (4.53):

$$P_{com} = \frac{1}{\eta_{m,c}} \dot{m}_c Cp T_{0c} \left(\beta_c^{(\gamma-1)/\gamma} - 1 \right) \tag{4.53}$$

where β_c is the pressure ratio, defined as the ratio of the outlet-to-inlet pressure and $\eta_{m,c}$ is the mechanical efficiency of the compressor, which is assumed to be constant.

The power generated by the turbine is calculated using Equation (4.54), while the net power generation from the GT is expressed by Equation (4.55):

$$P_{tur} = \eta_{m,t} \dot{m}_t CpT_{0t} \left(1 - \beta_t^{(\gamma-1)/\gamma} \right) \tag{4.54}$$

$$P_{GT} = \left(P_{tur} - P_{com} \right) \eta_{gen} \tag{4.55}$$

where $\eta_{m,t}$ is the mechanical efficiency of turbine, which is also assumed to be constant.

Since not all the fuel is consumed by the fuel cell system, the fuels employed should comprise low percentages of hydrogen and carbon monoxide in the combustion chamber. Due to the high temperature involved in fuel cell operation, the air mass flow is much higher than the fuel, which will control the stack temperature. The oxidant in the combustion process is a combination of the depleted oxygen of the MCFC cathode outlet stream and the additional air feed. Moreover, it is much higher than the required combustion stoichiometric value that results in complete combustion reactions (Equations. (4.56) - (4.58)). To determine the exit temperature of the combustor, the energy balance for the combustion chamber, in which η_c represents the combustion efficiency was established (Equation (4.59)).

$$CH_4 + 2O_2 \rightarrow CO_2 + 2H_2O \tag{4.56}$$

$$H_2 + 0.5O_2 \rightarrow H_2O \tag{4.57}$$

$$CO + 0.5O_2 \rightarrow CO_2 \tag{4.58}$$

$$\dot{m}_a \hat{C}_{P,a}^{ig} \Delta T_2 + \dot{m}_f LHV = (\dot{m}_a + \dot{m}_f)\hat{C}_{P,g}^{ig} \Delta T_3 + \dot{m}_f LHV (1 - \eta_c) \tag{4.59}$$

The storage design total volume can be determined as reported by Sheng et al. (2017):

$$V_{air,storage} = \frac{P_{com} t_{charge} \eta_{m,c}}{CpT_{0c} \left(\beta_c^{(\gamma-1)/\gamma} - 1 \right)} \bullet \frac{\Re T}{P} \tag{4.60}$$

The simplified TES model (Gil et al., 2010) is divided into two parts: (1) cold heat transfer fluid (HTF) storage and (2) hot HTF storage (**Figure 4.5**). The temperatures of the hot and cold HTF storages should be constant during operation. The compressed air after the compressor is cooled down normally to room

temperature (298.15 K) to increase the energy storage density (Mozayeni et al., 2017). To determine the TES volume required, the charging heat is calculated by Equation (4.61). The design volume of the TES is calculated using Equation (4.62). The compressed air is heated before the air is fed to the turbine (Equation (4.63)).

$$\dot{Q}_{TES,C} = \dot{m}_{air,C} Cp_{air} (T_C - T_{C,0}) \tag{4.61}$$

$$V_{TES} = \frac{Q_{TES,C} T_{charge}}{Cp_{TES} (T_{Hot} - T_{Cold})} \tag{4.62}$$

$$T_D = T_{D,0} - \left(\dot{Q}_{TES,C} \eta_{TES}\right) / \left(\dot{m}_{air,D} Cp_{air}\right) \tag{4.63}$$
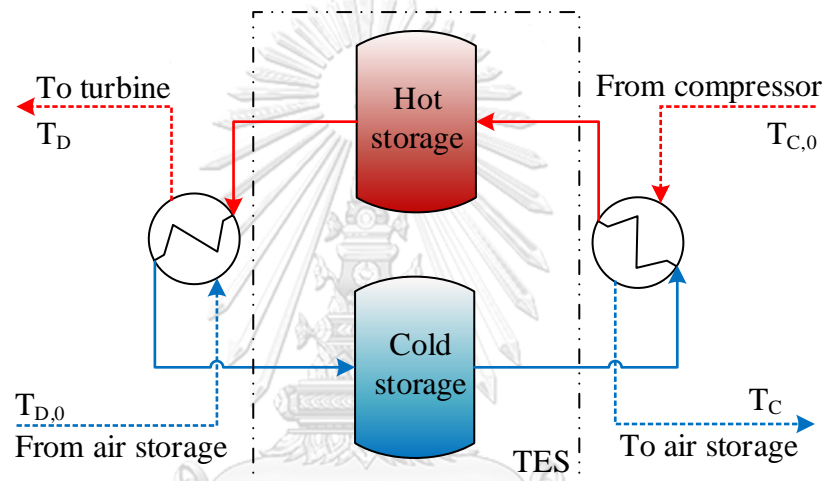
Figure 4.5 Simplified thermal energy storage (TES) model in the advanced adiabatic compressed air energy storage (AA-CAES) system

CHAPTER 5

Investigating the performance of a solid oxide fuel cell and a molten carbonate fuel cell integrated system

This chapter presents the implementing of a molten carbonate fuel cell with solid oxide fuel cell. The investigation is performed by using steady-state model of mass and electrochemical model. The effect of key operating parameters on the SOFC and MCFC is considered to investigate the performance of the system. The integrated system is also compared with the single of SOFC and MCFC. This chapter is related to the work of Jienkulsawad and Arpornwichanop (2016).

5.1 Introduction

Alternative power sources are currently being researched due to environmental concerns. Fuel cells are devices that directly convert chemical energy into electrical energy at high efficiencies using environmentally friendly methods compared to conventional combustion-based processes (EG&G Technical Services, 2004). High-temperature fuel cells (HTFCs) such as solid oxide fuel cells (SOFCs) and molten carbonate fuel cells (MCFCs) typically operate at temperatures above 600 ℃ and produce heat that can be used in fuel processing and heat generation systems. HTFCs are more flexible with regard to the fuels they can use; fuels such as methane, methanol and ethanol, can be reformed at the anode of an HTFC to produce hydrogen and carbon monoxide through a process called direct internal reforming where the reforming and oxidation reactions are occurred (Bakalis and Stamatis, 2014; Baldinelli et al., 2015; Papurello et al., 2015; Rokni, 2013). It is noted that as the reforming concentrates in a reduced area of the anode, it is usual that internal reforming has to be done partly indirectly. The advantage of this type of operation is the high conversion rate and associated high efficiencies (da Rosa, 2009; Laosiripojana and Assabumrungrat, 2007; McPhail et al., 2011).

In SOFCs, methane can be directly fed to a Ni/YSZ anode without the carbon formation problem when the appropriate steam content is supplied; additional steam inhibits carbon from being generated (Laosiripojana and Assabumrungrat, 2007).

However, the power density decreases as the steam content increases due to dilution in the fuel channel (Janardhanan et al., 2007). Partial reforming of fuels, called external pre-reforming, can be used to avoid carbon formation and fuel dilution (Adams II et al., 2013; Arpornwichanop et al., 2009; Arpornwichanop et al., 2010; Cocco and Tola, 2009b). Because SOFCs cannot operate at a high fuel utilization rate, a hydrogen deficiency causes a collapse in the physical structure (Adams II et al., 2013; Nehter, 2007; Nishikawa et al., 2008). Thus, SOFCs tend to operate at a moderate fuel utilization rate; the resulting exhaust gas from the SOFC anode is still valuable due to the quantity of remaining fuels, such as hydrogen and carbon monoxide.

Generally, the exhaust gas from SOFCs is used in another heat and/or power generation system. The exhaust gases from the anode and cathode are mixed and burned in an afterburner to generate heat, which is required for upstream preheating or steam production. The second way to improve the performance of the system is by recycling the exhaust gases similar to many typical chemical processes; the anode and/or cathode can also be recycled, eliminating or reducing the required external steam and improving the excess heat recovery. The combined systems with SOFCs, such as an SOFC combined with a gas turbine (SOFC-GT) or combined with another fuel cell, are alternatively potential way to improve the electrical efficiency; however, the efficiency of SOFCs is typically higher than the Carnot cycle (Adams II et al., 2013; Saebea et al., 2012). Thus, many researchers have theoretically studied on the integration of SOFCs with other fuel cells. A system with an SOFC and a polymer electrolyte fuel cell (SOFC-PEFC) provided an efficiency of 59% (Yokoo and Take, 2004); a high-temperature SOFC and a low-temperature SOFC provided an efficiency of 50.3% (Araki et al., 2006); and an oxygen-ion-conducting electrolyte and a proton-conducting SOFC provided an efficiency of 54.11% (Patcharavorachot et al., 2010).

Like SOFCs, MCFCs are also directly fed by methane and can be combined with other heat and/or power generation systems. The similarities of SOFCs and MCFCs include a nickel-based oxidation catalyst, their operating conditions and their applications (McPhail et al., 2011). The significant difference between SOFCs and MCFCs is their charge carriers that diffuse through different electrolytes: oxygen ions (O^{2-}) diffuse through YSZ in SOFCs, and carbonate ions diffuse through

Li_2CO_3/Na_2CO_3 in MCFCs. These differences indicate that MCFCs require carbon dioxide and oxygen at their cathodes to operate effectively. The product gas from the anode of an SOFC is normally found in the anode of an MCFC, which indicates that MCFCs can use the product gas from SOFCs directly, which increases the fuel utilization and ultimately produces more electricity. The idea of an integrated SOFC-MCFC system has been proposed by McPhail et al. (2011). They mentioned the possibility of merging the solid oxide and molten carbonate electrolytes by creating a composite electrolyte based on carbonate-impregnated ceramics as a result of the similarity in their operating temperature and anode catalyst. However, that possibility looks into new fuel cell concepts and requires a long time to successfully synthesize a composite electrolyte. Thus, the integrated system proposed in this study uses the integrated idea to increase the performance and utilize the remaining fuel from the SOFC.

In this study, the performance of the SOFC and MCFC integrated system is compared to a single SOFC and MCFC at selected operating conditions (details shown in Section 5.2.1) and then the performance of the SOFC and MCFC integrated system is studied in each operating condition (degree of pre-reforming in Section 5.2.2, operating temperature of fuel cells in Section 5.2.3, fuel utilization in Section 5.2.4 and carbon dioxide fed to MCFC cathode in Section 5.2.5). The schematics of the fuel cell systems are shown in Figure 5.1. First, the fuel and steam are fed to the pre-reformer to produce reformed gas in all systems. For the single system, the reformed gas is fed to the SOFC or MCFC where the steam reforming and the water-gas-shift reaction occur. For the integrated system, the synthesis gas is fed to the SOFC. The MCFC uses the remaining gases from the SOFC, where CO further reacts with H_2O to produce more H_2; this H_2 is then used to produce more electrical power. As a result, more electrical power is produced by the integrated system. The remaining gas from the fuel cell is mixed and burned in an afterburner in all of the systems and used in preheating units. The performance of the integrated system is evaluated by the conservation of mass and the electrochemical model of an SOFC and an MCFC. The sequence of the calculation is shown in Figure 5.2.
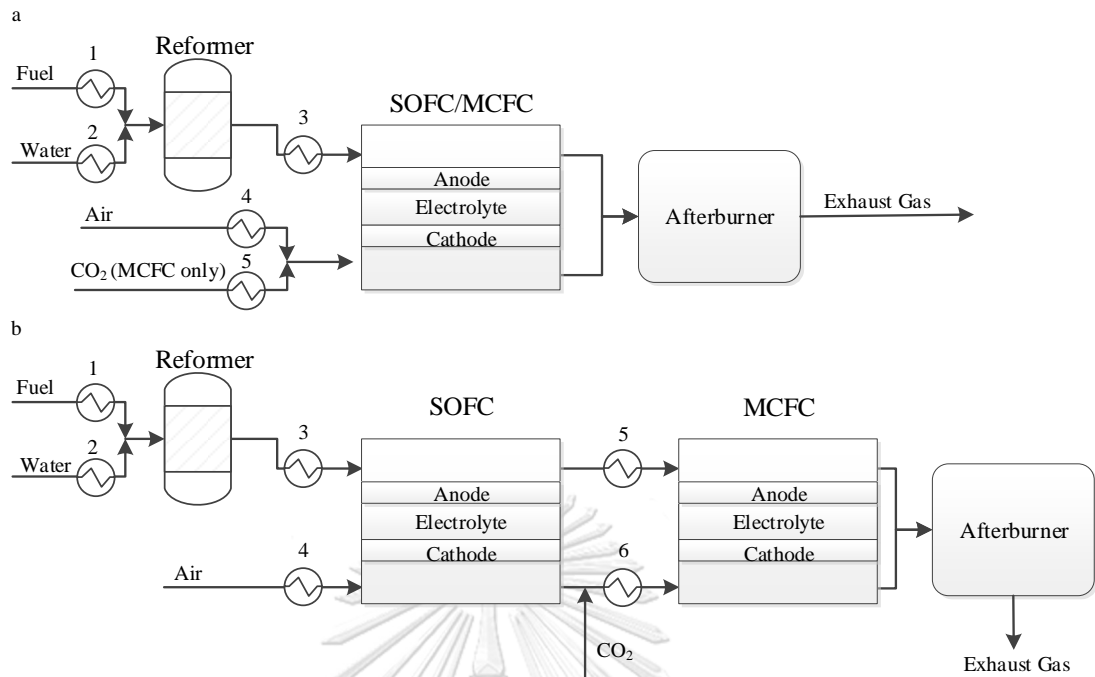
Figure 5.1 Schematic of a single system (a) and of the integrated system (b).
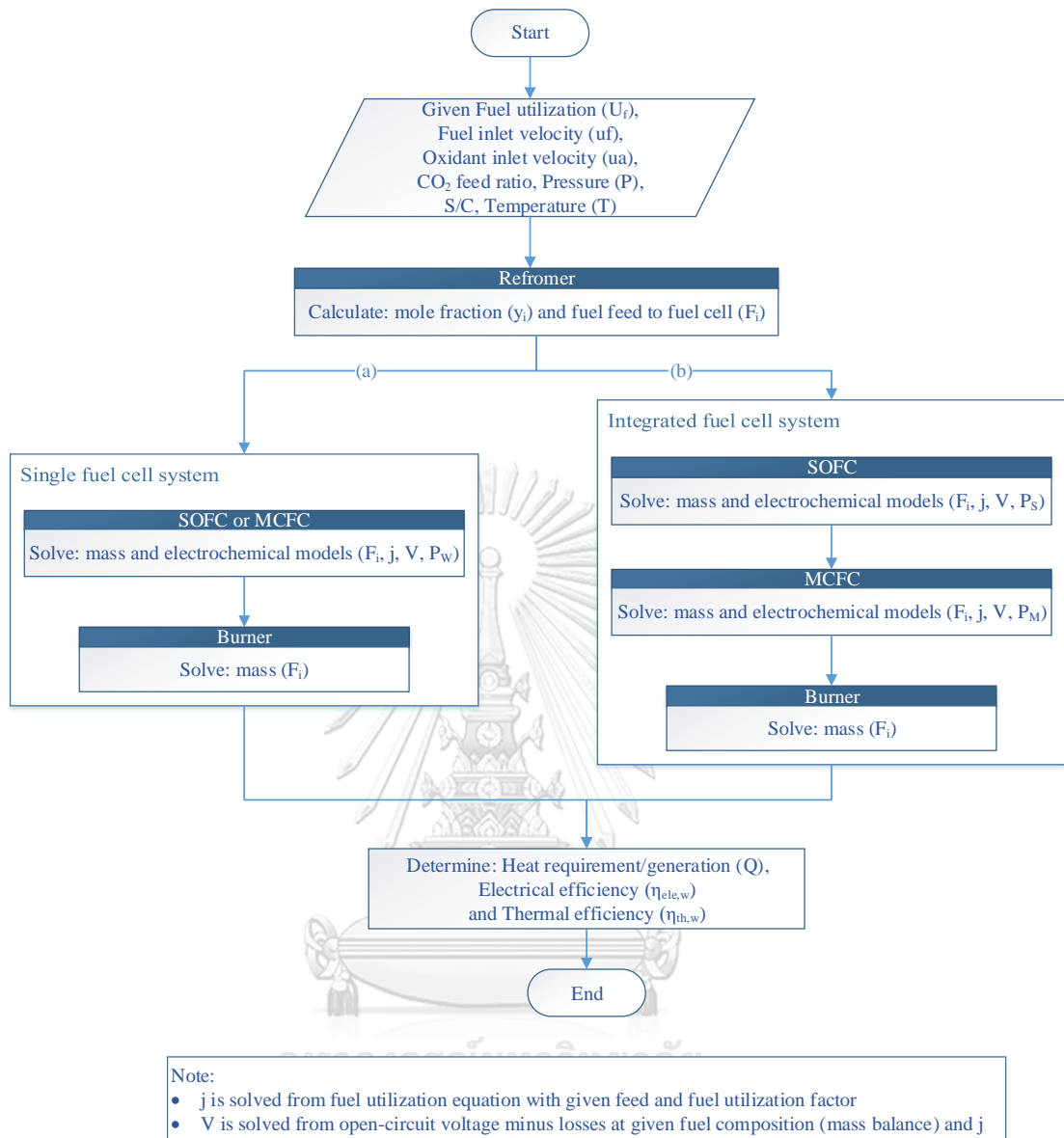
Figure 5.2 A solution diagram of the fuel cell systems model.

5.2   Results and Discussion

Firstly, the performance of the SOFC and MCFC integrated system is compared to a single SOFC and MCFC in Section 5.2.1. Next, the performance of the SOFC and MCFC integrated system is studied in each operating condition (Section 5.2.2 - Section 5.2.5).

5.2.1 Performance of the SOFC, the MCFC and the integrated system

In comparison, the reformer is performed at 10% pre-reforming with steam-to-carbon ratio of 3 for a single fuel cell system (2 for the integrated system) under 1 atm and 973 K. The fuel is fed to the fuel cell with velocity 2 m/s and the oxidant is fed with velocity 18 m/s. The SOFC is operated at 1 atm and 1073 K with fuel utilization factor of 0.7 whereas the MCFC is operated at 1 atm and 973 K with fuel utilization factor of 0.8. The performances of the single SOFC, the single MCFC and the integrated system are shown in Figure 5.3(a). It is shown that the integrated system provides a higher electrical efficiency than the single SOFC or the single MCFC; however, the thermal efficiency of both of the single fuel cells is better than that of the integrated system. Because the remaining fuel from the SOFC is used for power generation via electrochemical reaction in the MCFC instead of burned in the afterburner. These findings indicate that the chemical energy is more effectively converted to electrical energy in the integrated system. Additionally, lower rates of steam and carbon dioxide from the MCFC are required in the integrated system; because the SOFC produces steam, the additional feed steam to the MCFC was not necessary. It is also shown that methane is completely reformed inside the SOFC; thus, the assumption that steam reforming is not occurring in the MCFC is reasonable. When considering the anode exhaust gas in each system (Figure 5.3(b)), it is shown that the amounts of CO and H_2 released from the integrated system are smaller than those of the single systems. As the operating temperature of the MCFC is lower than that of the SOFC, the water-gas shift reaction is more pronounced in the MCFC causing a decrease in the amount of CO. In addition, H_2 produced is consumed to produce more power in the MCFC. This confirms that the integrated system can use fuel more effectively. The CO_2 that exits the anode of the integrated system is a bit higher than the MCFC because part of CO_2 is produced from the SOFC fed to the MCFC and another part is from the MCFC itself. Hence, the CO_2 in the anode can be more concentrated in the integrated system (as some researchers claimed the MCFC is

a CO_2 concentrator (Campanari, 2002; Caprile et al., 2011; Wee, 2010; Williams and Maru, 2006)).
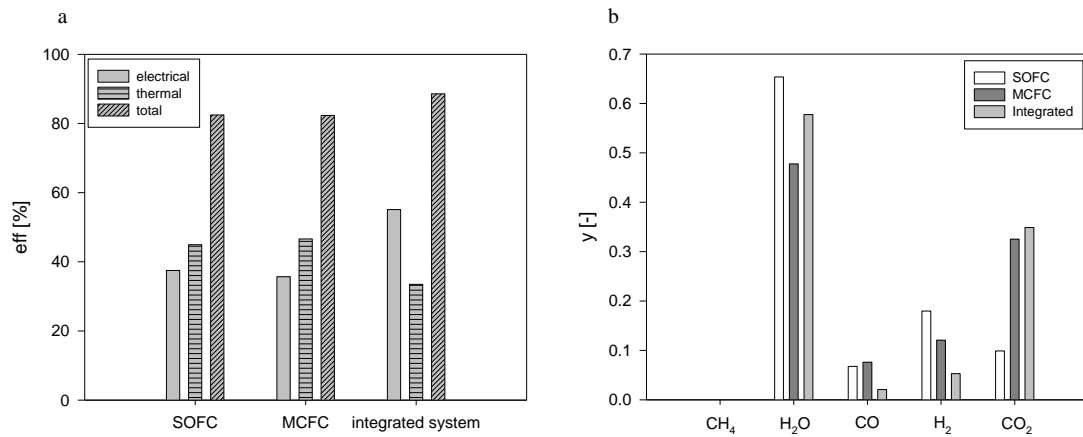
Figure 5.3 Efficiency of the system (a) and the composition of the anode exhaust gas of the system (b).

5.2.2 Effect of degree of pre-reforming

The use of a pre-reformer to partially reform a portion of the fuel before it is fed to the fuel cell can mitigate the carbon formation in the fuel cell. The effect of the degree of pre-reforming on the efficiency of the integrated system and the SOFC part and MCFC part of the integrated system is shown in Figure 5.4. It is shown that increasing the degree of pre-reforming results in a slight increase in the SOFC efficiency (SOFC in the integrated system); this is because more hydrogen is generated due to the higher degree of pre-reforming. This finding indicates that hydrogen-rich gas is fed to the SOFC, leading to a higher open-circuit voltage and lower losses, and thus, there is an increase in the power generated in the SOFC. However, the efficiency of the integrated system decreases as the degree of pre-reforming increases. Because more of the fuel is used to generate power in the SOFC, a higher degree of pre-reforming reduces the amount of fuel fed to the MCFC, which results in lower power generation.
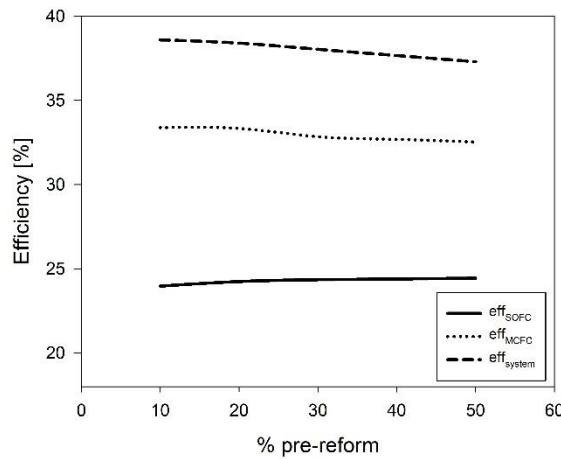
Figure 5.4 Effect of the degree of pre-reformation on the efficiency of the integrated system (overall), the SOFC part of the integrated system and the MCFC part of the integrated system ($T_{reformer}$ 1023K, T_{SOFC} 1023K, T_{MCFC} 973K, $U_{f,SOFC}$ 0.7, $U_{f,MCFC}$ 0.8, and CO_2 feed ratio 2).

5.2.3 Effect of the operating temperature of the fuel cells

Figure 5.5 shows the efficiencies of the integrated system and the SOFC part and MCFC part of the integrated system as functions of the operating temperature. It is shown that the efficiency of the SOFC in the integrated system can be improved by increasing the operating temperature. At higher SOFC operating temperatures, although the open-circuit voltage of fuel cells decreases, a reduction in the cell overpotentials (all types of loss decrease) is dominant in the cell voltage. Even though an increase in the SOFC operating temperature results in a faster electrochemical reaction, the CO concentration at the outlet is higher. That is because the water-gas-shift reaction is less promoted in higher temperature. The efficiency of the MCFC in the integrated system, however, decreases with increasing cell temperature. As a result of the exothermic water-gas-shift reaction, it seems that the reaction reverses when temperature increases (CO_2 and H_2 concentrations are reduced while CO is increased). Increasing in the MCFC temperature, it is found that the open-circuit voltage of the MCFC is dramatically decreased whereas all losses are slightly reduced. Thus, the open-circuit voltage is more dominate in power generation when

MCFC temperature increases. For the overall efficiency (integrated), the efficiency is shown to marginally decrease with increasing MCFC temperatures, while the temperature of the SOFC significantly affects the efficiency of the integrated fuel cell system. The SOFC temperature should be higher than the MCFC temperature to enhance the integrated system efficiency.
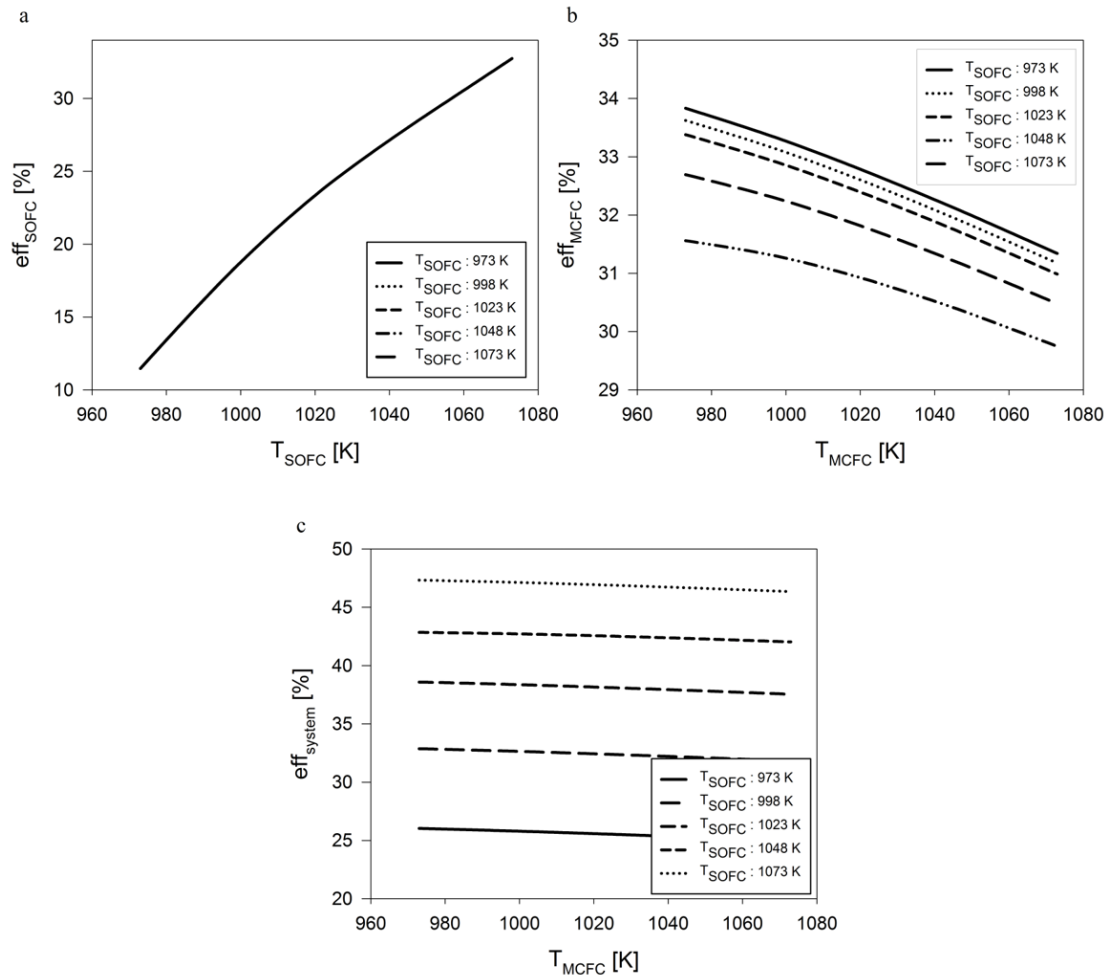
Figure 5.5 Effect of the operating temperature of the fuel cells on the efficiency of the SOFC in the integrated system (a), the MCFC in the integrated system (b) and the integrated system (overall) (c) (degree of pre-reforming 10%, $T_{reformer}$ 973K, $U_{f,SOFC}$ 0.7, $U_{f,MCFC}$ 0.8, and CO_2 feed ratio 2).

5.2.4 Effect of fuel utilization on fuel cells

The fuel utilization factor describes the amount of hydrogen used in the fuel cells. As mentioned in the introduction, if the SOFC operates at a high fuel utilization, the amount of hydrogen fed to the MCFC will be low, and the SOFC will incur cell damage with NiO formation; this will affect the power generation. The effect of the fuel utilization of the SOFC and MCFC on the efficiency of the SOFC in the integrated system, the MCFC in the integrated system and the integrated system (overall) is shown in Figure 5.6. In the SOFC part (Figure 5.6(a)), the efficiency rapidly increases at first with increasing fuel utilization because more hydrogen is used, as shown in Figure 5.8(a). However, the operating voltage of the SOFC (Figure 5.7(b)) decreases as a result of less fuel at high fuel utilization. In the MCFC part of the integrated system (Figure 5.6(b)), the efficiency improves with increasing fuel utilization in both cells because the amount of H_2 and CO in the exhaust gas from SOFC is low at high SOFC fuel utilization. However, higher MCFC operating voltages are generated as the fuel utilization of the SOFC increases and the fuel utilization of the MCFC decreases, as shown in Figure 5.8(a); therefore, the current density depends on the fuel utilization. Because the feed of the MCFC is a product of the SOFC, the current density of the MCFC depends on the fuel utilization in both cells (Figure 5.8(b)). The power density of the MCFC can be improved by increasing the fuel utilization of the MCFC and decreasing the fuel utilization of the SOFC, as shown in Figure 5.8(c). For the integrated system (Figure 5.6(c)), the efficiency increases with increasing fuel utilization in the MCFC and decreasing fuel utilization in the SOFC. However, the fuel utilization of the SOFC should not reach 0.6 because it will create more build up of the cathode resistance in the MCFC. It causes by CO_2 in the cathode of MCFC lower than the fuel in the anode side. At a fuel utilization of SOFC below 0.6, the MCFC collapses. Because CO_2 and O_2 are slower to transport to the electrolyte than CO_3^{2-}, which causes an imbalance in the molten salt in the electrolyte. Figure 5.9 shows the exhaust gas composition of the integrated system compared to that of the SOFC; Figure 5.7(a) shows that the integrated system releases less hydrogen gas than the SOFC system.
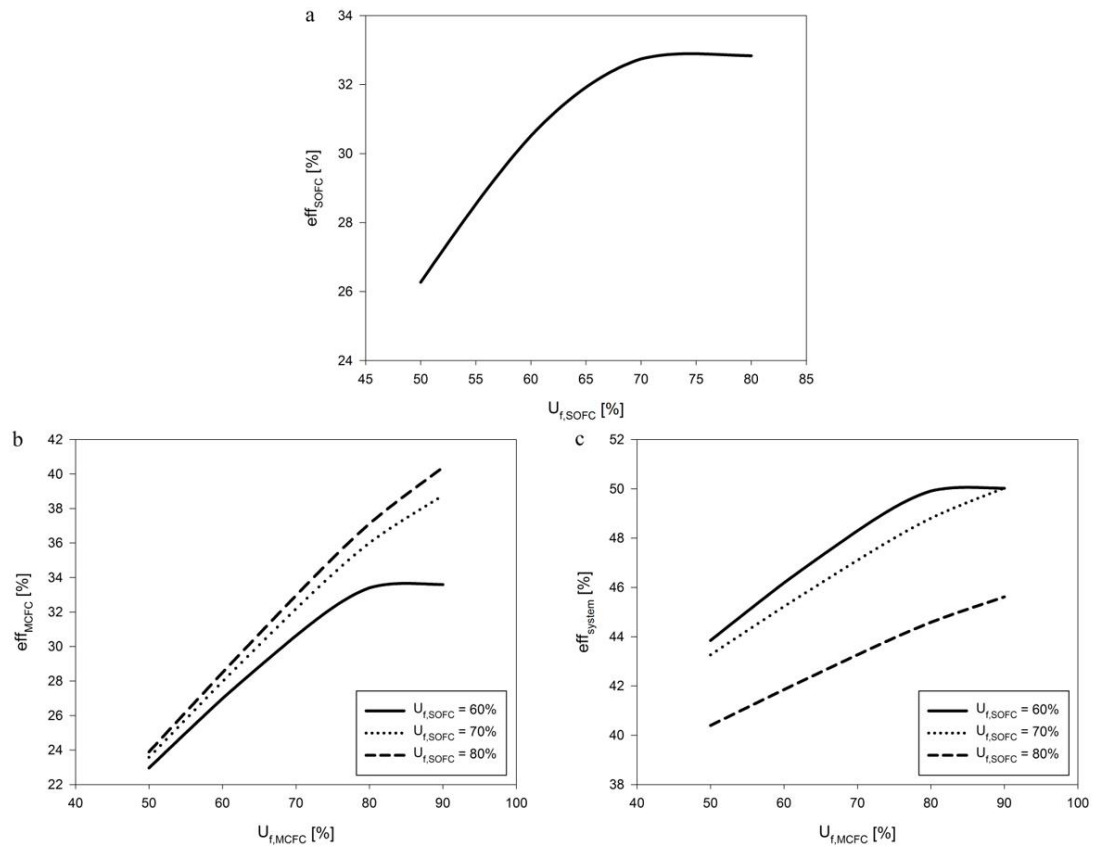
Figure 5.6 Effect of the fuel utilization of the fuel cells on the efficiency of the SOFC in the integrated system (a), the MCFC in the integrated system (b) and the integrated system (overall) (c) (degree of pre-reforming 10%, $T_{reformer}$ 973K, T_{SOFC} 1073K, T_{MCFC} 973K, and CO_2 feed ratio 2)
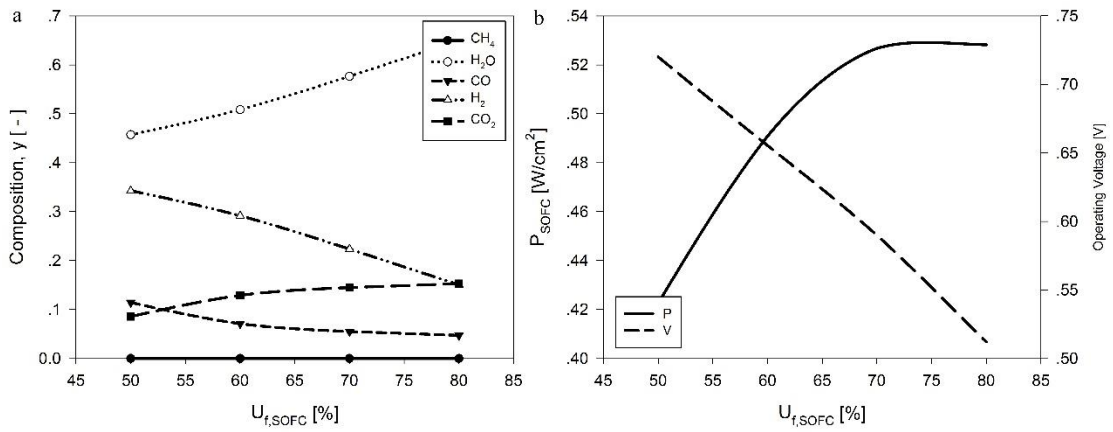
Figure 5.7 Outlet compositions of the anode (a), and the power density and operating voltage (b) of the SOFC part of the integrated system
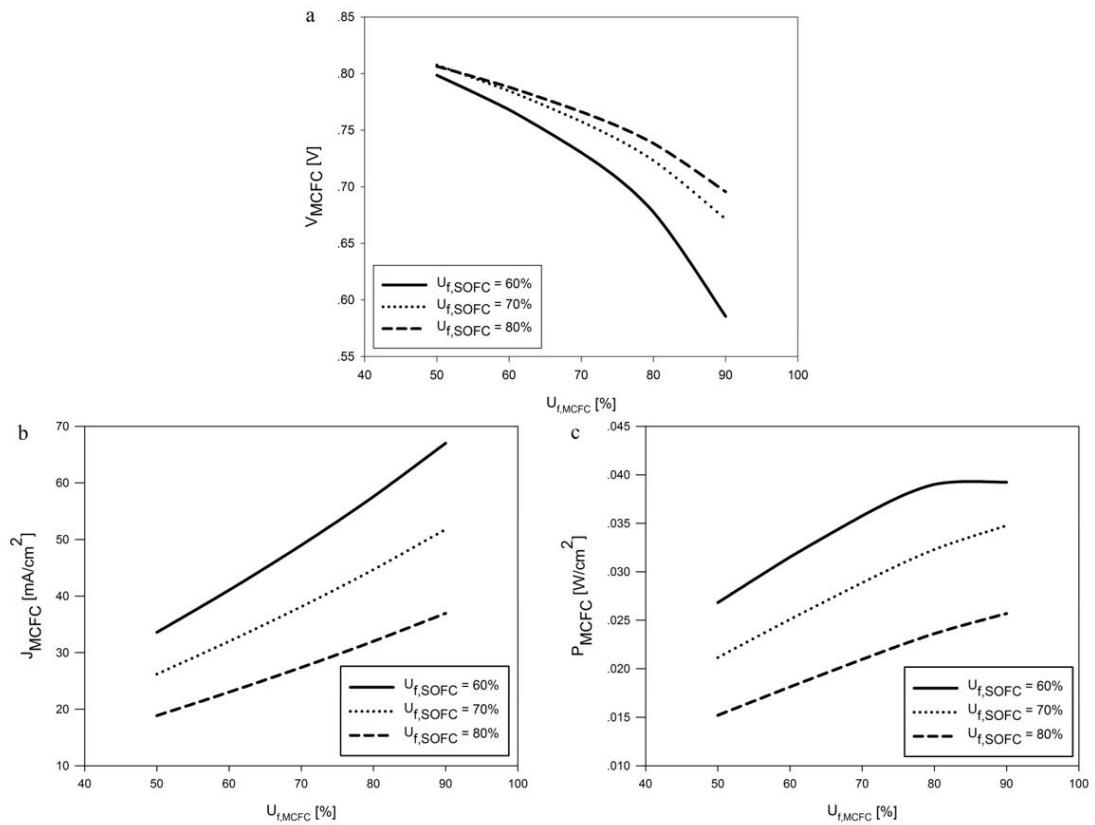
Figure 5.8 Operating voltage (a), current density (b) and power density (c) of the MCFC part of the integrated system.
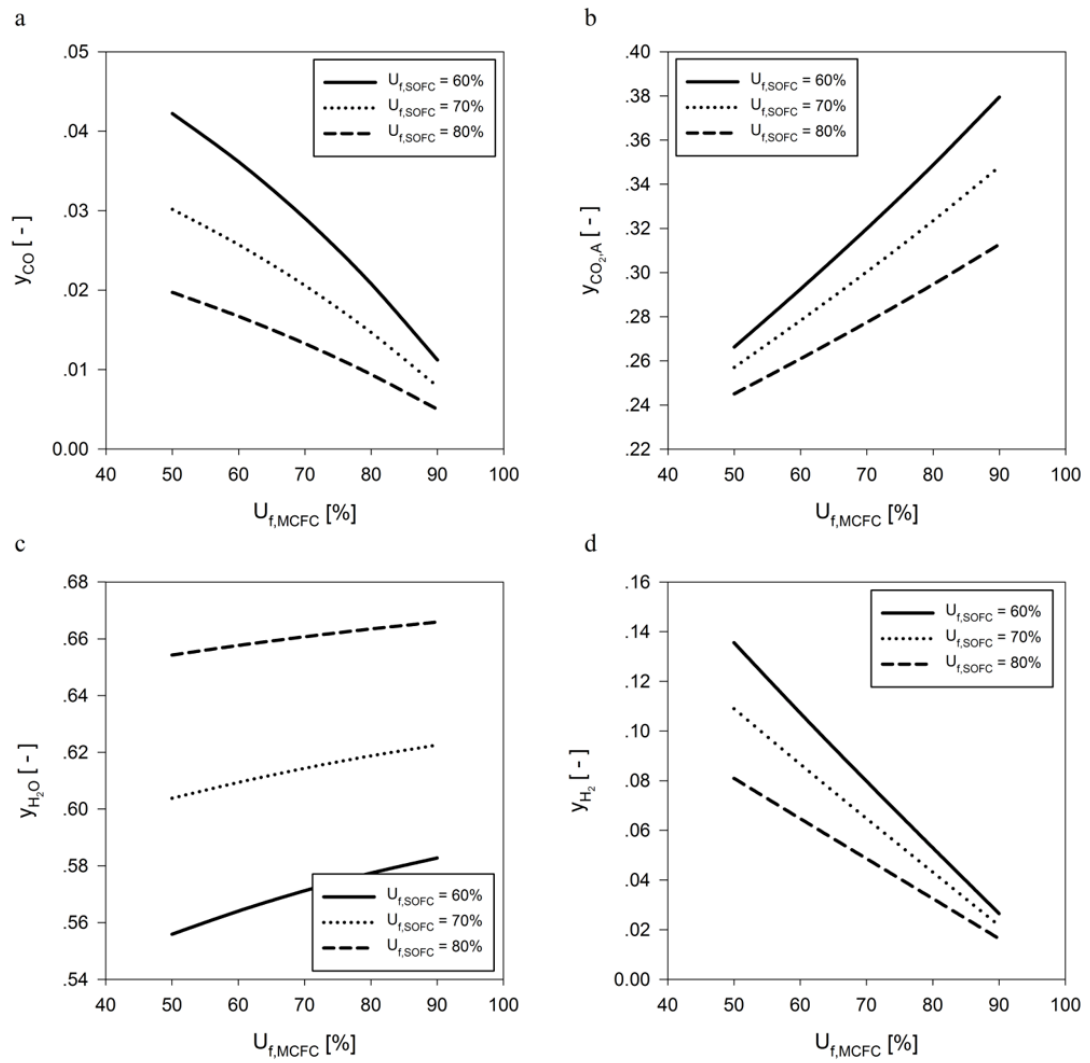
Figure 5.9 Anode exhaust gas compositions of the integrated system.

5.2.5 Effect of the carbon dioxide feed in the cathode of the MCFC on performance

From the configuration shown in Figure 5.1, the carbon dioxide fed to the cathode of the MCFC does not specify the carbon dioxide source in the general case, so the carbon dioxide can come from any process. The concentration of the carbon dioxide is one of the factors that can improve performance. When additional carbon dioxide is fed to the cathode, the performance of the MCFC part of the integrated system and the integrated system may be improved. The effect of the amount of carbon dioxide on the MCFC is investigated by varying the carbon dioxide feed ratio. Figure 5.10 shows the effect of the carbon dioxide feed ratio on the efficiency of the MCFC in the integrated system and the integrated system (overall). The x-axis denotes the CO_2 in the cathode inlet of the MCFC per the CO_2 in the anode inlet of the MCFC because this fraction directly affects to the voltage of the MCFC. The result shows that the efficiencies of the MCFC part and the integrated system increase with an increasing carbon dioxide feed ratio (increase in partial pressure of CO_2 in cathode per partial pressure of CO_2 in anode); this is because the open-circuit voltage increases, and the cathode resistance decreases, as shown in Figure 5.11(a). Figure 5.11(b) shows that the current density is independent of the carbon dioxide feed ratio. However, the additional carbon dioxide feed can marginally improve the performance of the MCFC and the integrated system. When the MCFC anode as a CO_2 source is fully recycled, the CO_2 feed ratio is 2.67. At the CO_2 feed ratio less than 2.67 (partial of MCFC anode is recirculated), the efficiency is significantly increased with increasing of CO_2 reed ratio as results of open-circuit voltage is increased and internal resistance in the electrolyte is dramatically decreased. A CO_2 feed ratio of 2.82 results from the integrated system when the exhaust gas from the burner is used as a CO_2 source. It is noted that when an additional source of CO_2 beside the system recycle stream is considered (CO_2 feed ratio > 2.82), the system efficiency could be enhanced.
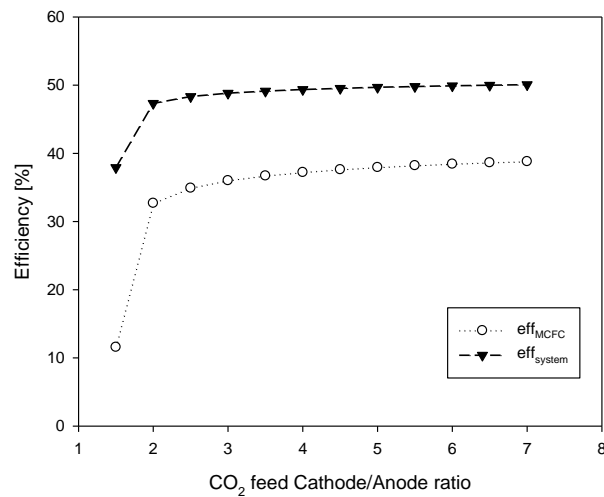
Figure 5.10 Effect of the carbon dioxide feed ratio on the efficiency of the MCFC in the integrated system and the integrated system (degree of pre-reforming 10%, $T_{reformer}$ 973K, T_{SOFC} 1073K, T_{MCFC} 973K, $U_{f,SOFC}$ 0.7, and $U_{f,MCFC}$ 0.8).
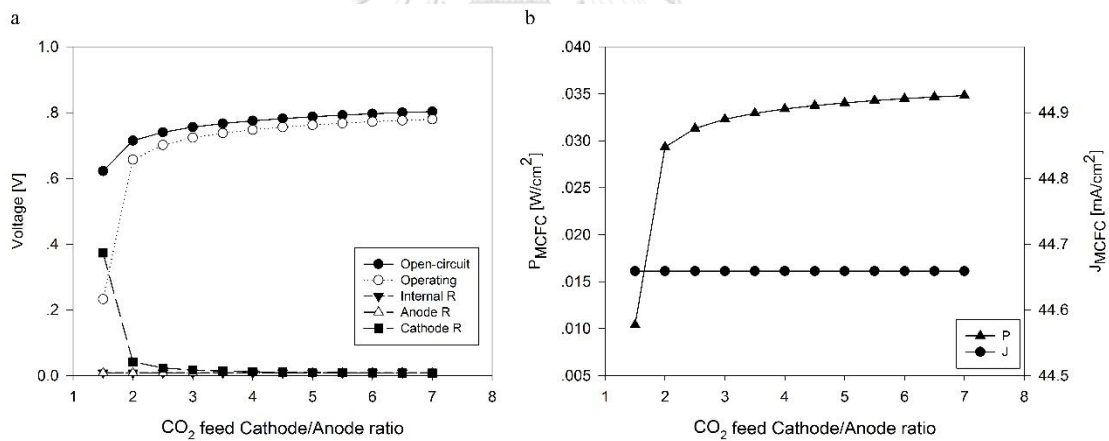
Figure 5.11 Operating voltage (a), power density and current density (b) of the MCFC in the integrated system.

5.3 Conclusions

In this study, the performance analysis of the SOFC and MCFC integrated system fed by methane was presented. Reformed gas from the pre-reformer was used as a fuel for the SOFC, and the exhaust gas from the SOFC was directly fed into the MCFC. The results showed that fuel utilization of both fuel cells, temperature of the SOFC and reformer dramatically affect the performance of the integrated system. A change in the degree of reforming, temperature of the MCFC and CO_2 feed ratio insignificantly affect the performance of the integrated system. The performance of the MCFC in the integrated system degrades when fuel utilization of the SOFC is lower than 60%. The simulation results indicated that the integrated fuel cell system provides a higher electrical efficiency than that of a single fuel cell. At the selected operating conditions (10% degree of reforming, 973 K reformer temperature, 1073 K SOFC temperature, 973 K MCFC temperature, 70% SOFC fuel utilization, 90% MCFC fuel utilization and fully recycled), the electrical efficiency of the integrated system is 55.22%. The system efficiency can be enhanced when the MCFC exhaust gas is further used for additional power generation.

จุฬาลงกรณ์มหาวิทยาลัย

CHULALONGKORN UNIVERSITY

CHAPTER 6

Analysis of a solid oxide fuel cell and a molten carbonate fuel cell integrated system with different configurations

This chapter presents the effect of different integrated fuel cell system configuration to the performance. The analysis is performed by using steady-state model of mass and electrochemical model. The NiO formation possibility is considered to investigate the performance of the system. All units are assumed to operate at their normal operation. Portions of chapter were appeared in Jienkulsawad et al. (2015) and Jienkulsawad et al. (2018).

6.1   Introduction

A reduction of carbon dioxide (CO_2) emission has presently been an important concern for conventional thermal power plants. Although renewable and sustainable energy sources can be used in power generation to reduce CO_2 emission, most power plants are still based on fossil fuels and technology that can capture, store and utilize CO_2 should be applied to mitigate CO_2 emission (Campanari et al., 2016; Chen et al., 2016; Rochedo et al., 2016; Wee, 2014).

High-temperature fuel cells (HTFCs) are high-performance power generation devices that can replace a conventional combustion-based power generator (Chatrattanawet et al., 2015) because heat produced from the fuel cell can be used in fuel processing and heat generation systems (McPhail et al., 2011). Moreover, HTFCs can directly use various types of fuels via direct internal reforming operation (Baldinelli et al., 2015; Curletti et al., 2015; Saebea et al., 2013). Syngas with tar can be also used in SOFCs at some tolerances (Doyle et al., 2014). As methane can be easily obtained during many production processes, such as petrochemical, refining and fermentation processes, it is widely used as a fuel for HTFCs (Davis and Martín, 2014; Mustapha et al., 2017; Yang et al., 2017).

Solid oxide fuel cells (SOFCs) and molten carbonate fuel cells (MCFCs) are among the HTFCs that have higher electrical efficiency and lower CO_2 emission than the combustion-based power plants (Adams II et al., 2013). For power plant

applications, the SOFC is more dominant due to a relatively higher power density and is less corrosive than the MCFC, which uses molten salt electrolyte that can be lost during a long term operation (Pietra et al., 2016). When considering the direct internal reforming operation of SOFC, excess steam input is needed to avoid carbon formation on the fuel cell anode (Yang et al., 2009). However, excessive steam will dilute the hydrogen concentration and cause hydrogen deficiency in the cell stack. This factor increases the formation of NiO on the anode and degrades the cell performance. This incident also occurs when the SOFC is run at a higher fuel utilization rate and thus, the SOFC is operated at a moderate fuel utilization rate (Nehter, 2007; Saebea et al., 2012). Under this operating condition, the anode exhaust gas is still valuable because of remaining fuels, such as hydrogen and carbon monoxide. These useful fuels can be directly used for producing additional power (Pastorino et al., 2011). Frangini and Masi (2016) reviewed the use of MCFC in advanced and sustainable energy sectors with three application categories; generation/conversion/storage of energy, materials and manufacturing processes, and applications to advanced gas processing and gasification technologies. In the advanced gas processing application, the MCFC has recently gained attention as an alternative CO_2 utilization technology (Mehmeti et al., 2016; Rinaldi et al., 2015; Wee, 2014). Wee (2014) claimed that MCFCs act as CO_2 concentrators or separators when integrated into traditional power plants, and they can increase the overall electrical efficiency and reduce CO_2 emission per power generation because of additional power generation and an increase in CO_2 recirculation inside the system. Currently, MCFCs are used in the bottom stream in a power plant to utilize CO_2 and reduce CO_2 emission (Discepoli et al., 2016). In fact, a standalone MCFC could not actually reduce an amount of CO_2 emission, however, CO_2 can be utilized by a MCFC. Although the SOFC itself can produce electricity without generating CO_2, the fuel processing to produce hydrogen for SOFCs involves the production of CO_2 as a byproduct. The integration of SOFCs with MCFCs could relieve this concern, as MCFCs utilizes CO_2 as a reactant in electricity generation. Thus, the SOFC and MCFC integrated system is not only a potential solution for increasing fuel utilization and power but also utilizes carbon dioxide. McPhail et al. (2011) indicated the possibility of merging SOFC and MCFC electrolytes by creating a composite electrolyte based on carbonate-impregnated ceramics, as both the fuel

cells have a similarity in their operating temperature and anode catalyst. Jienkulsawad et al. (2015) studied the integrated system of the SOFC, as a main power generation and the MCFC, as a carbon dioxide concentrator. They proposed that the exhaust gases of the SOFC should be directly introduced to the MCFC and a recirculation of the exhaust gas from an after-burner to MCFC can enhance the energy efficiency and decrease the CO_2 emission. However, NiO formation affecting the SOFC performance is not considered.

As the configuration of the SOFC-MCFC integrated system is important and affects the system performance, in this study, the performance of such an integrated fuel cell system with different configurations with and without feed separation and exhaust gas recirculation is investigated. Air fed to SOFC in parallel configurations is considered. The energy efficiency and CO_2 emission coefficient (CEC) are key parameters for comparing the fuel cell system performance. Moreover, heat duty requirement and the effect of the NiO formation caused by hydrogen deficiency on the fuel cell performance are also taken into account.

6.2 System Configuration

In this study, different configurations of the integrated system, as shown in Figure 6.1 Configurations of the SOFC and MCFC integrated system, are analyzed and compared to determine the suitable system design in terms of power generation and carbon dioxide utilization. The steam-to-carbon ratio is fixed at 2 and 10% pre-reforming in order to avoid carbon formation (Adams II et al., 2013; Yang et al., 2009) in all configurations. For comparison, units are set at the same operating condition in each design to evaluate the effect of different designs and whether NiO formation is possible or not in each system design. The operating conditions of each unit is shown in Table 6.1 and the fuel cell dimension is given in **Table 4.1**. For the first configuration (A) (Figure 6.1(a)), the MCFC is placed at the bottom of the existing SOFC system. The reformed gas is divided to operate the MCFC and the exit-gas from the existing SOFC system is the carbon dioxide source of the MCFC system. The anode off-gas of the MCFC is fully recirculated to burn the faction of remaining fuel. The configurations that are used to compare with configuration (A) are designed by fuel flow pattern between two fuel cell types because the fuel is the

main key of power generation by fuel cell. Configuration (B) (Figure 6.1(b)) represents a series configuration and a parallel configuration is shown in (C) (Figure 6.1(c)). An additional configuration (D) is represented as series-parallel combination configuration. In configuration (B), both the anode and the cathode off-gas from the SOFC are directly fed to the MCFC and portion of the exhaust gas from an after-burner is recirculated to the MCFC. In this configuration, the MCFC uses the remaining fuel from the SOFC, which means this design can improve the fuel utilization of the integrated system, and examines its performance under a lower fuel concentration fed to the MCFC. In the third design (C), the reformed gas is separately fed to the SOFC and the MCFC. Air is separated according to the amount of reformed gas fed to the SOFC. The cathode off-gas is mixed with air and fed to the MCFC. The anode off-gas from the SOFC and the MCFC are mixed with the remaining gas from the cathode of the MCFC and burnt in the burner and portion of the exhausted gas is recirculated. The differences between this configuration and configuration (A) are the recycled steam, the position of the exhaust gas and the heat duty. In configuration (C), the reformed gas may not improve the fuel utilization of the integrated system. The aims of this research are to study the effects of increasing the feed to the MCFC and consequently reducing the feed to the SOFC in order to increase the amount of fuel feed to operate the MCFC. The last configuration (D) (Figure 6.1(d)) differs from configuration (C) in that the exit-gas from the SOFC is mixed with reformed gas. It can handle the remaining fuel from the SOFC more efficiency but produced water will dilute the fuel.

Table 6.1 Operating conditions

Reformer	
Temperature	973 K
Pressure	1 atm
Steam-to-carbon ratio	2
Pre-reforming	10 %
SOFC	
Fuel feed velocity	2 m s^{-1}
Air feed velocity	18 m s^{-1}
Temperature	1073 K
Pressure	1 atm
Voltage	0.7 V
MCFC	
Temperature	923 K
Pressure	1 atm
Voltage	0.7 V
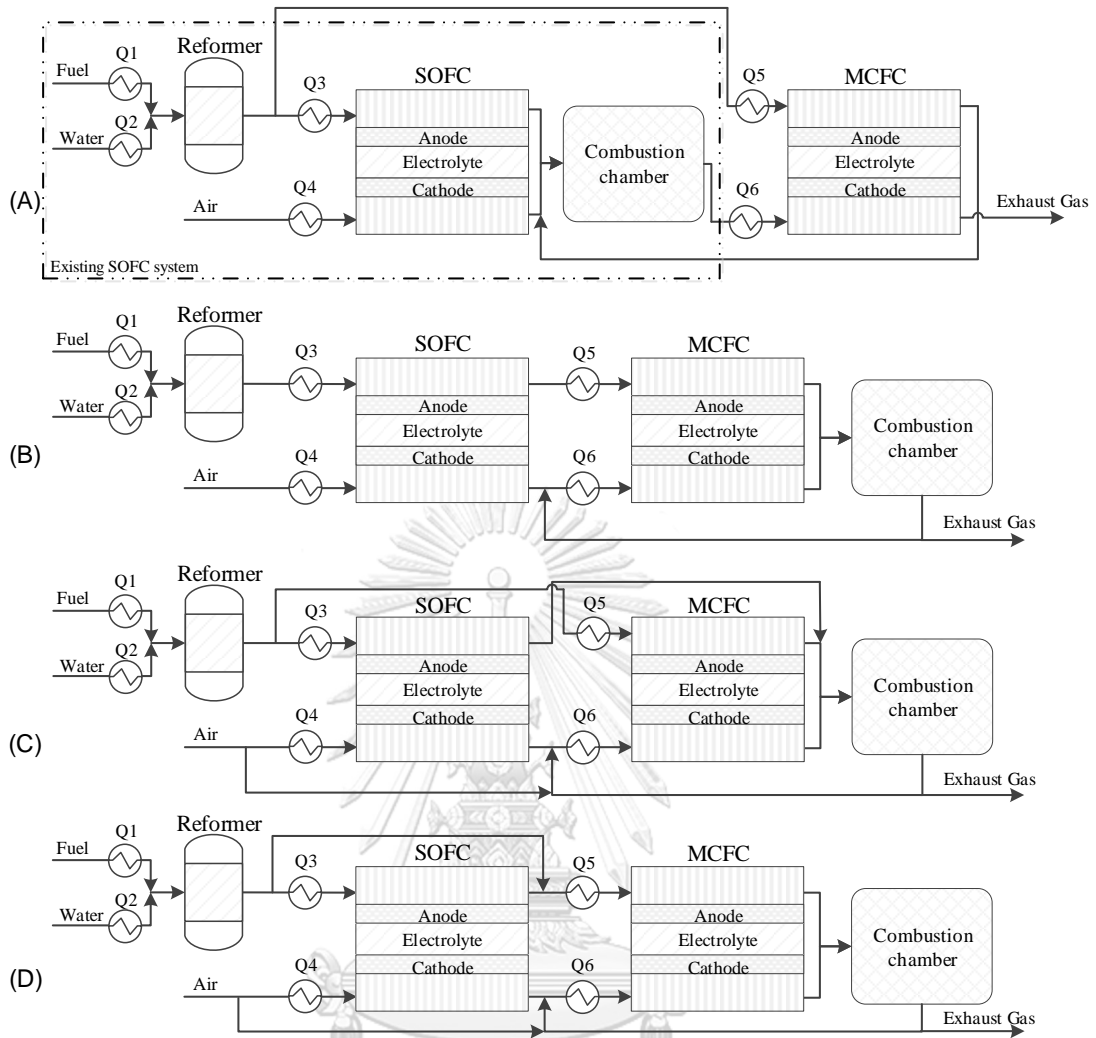
Figure 6.1 Configurations of the SOFC and MCFC integrated system

In this study, we set the steam to carbon ratio to 2 to avoid carbon formation in the catalyst, but when too much steam is fed, it causes NiO formation, decreasing the catalytic activity toward hydrogen oxidation. Thus, estimating the NiO generation possibility in the system is necessary in the configuration design. The formation of nickel oxide can be estimated by comparing the oxygen activity given by nickel oxidation and hydrogen oxidation. In order to avoid the nickel oxide formation at the electrochemical equilibrium condition, the oxygen activity given by hydrogen oxidation (Equation (6.2)) must be lower than that by nickel oxidation (Equation (6.1)). These two equations are used to estimate a possible region of NiO formation by setting Equation (6.1) equal to Equation (6.2) (Nehter, 2007).

Nickel oxidation ($Ni+1/2O_2 \leftrightarrow NiO$): the oxygen activity is given by:

$$\log\left(a_{O_2}\right)_{\text{Ni-NiO}} = 8.96 - \frac{24430}{T}$$

(6.1)

Hydrogen oxidation ($H_2+1/2O_2 \leftrightarrow H_2O$): the oxygen activity is calculated by:

$$\log\left(a_{O_2}\right)_{\text{H}_2\text{-H}_2\text{O}} = 2\log\left(\frac{p_{\text{H}_2\text{O}}}{p_{\text{H}_2}}\right) - \frac{26000}{T} + 5.94$$

(6.2)

It is noted that this model cannot determine the amount of NiO. It simply forbids the opportunity for NiO formation in the Ni-based fuel cell.

The numerical solution of the fuel cell system model can be summarized as shown in Figure 6.2.
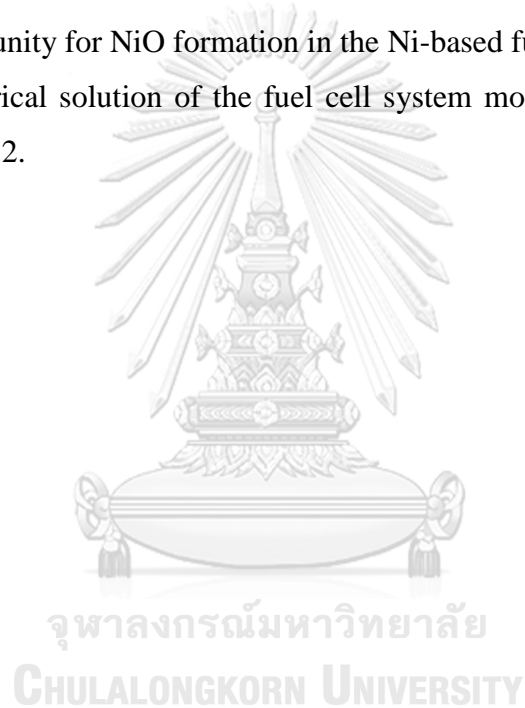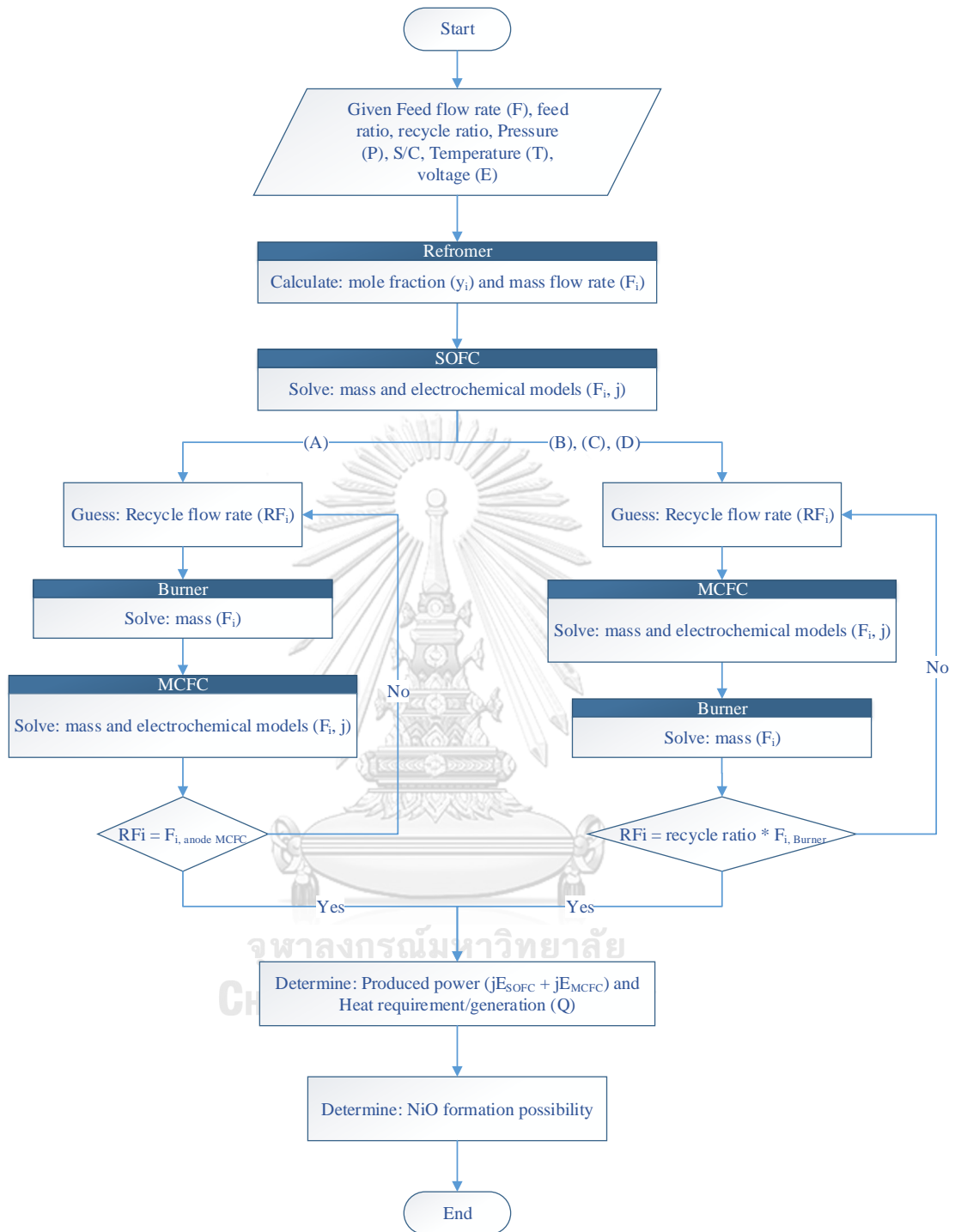
Figure 6.2 A solution diagram of the integrated fuel cell system model.

6.3   Results and Discussion

The performance of the SOFC and MCFC integrated systems with different configurations is compared under the same operating conditions and amount of fuel, steam and air feeds. The performance is studied in terms of the produced power revealed the amount of generated power by the system per 1 kilogram of methane feed, the CO_2 emission coefficient (CEC) described the amount of CO_2 released in kilograms to produce 1 kW-h electricity and the heat duty represented amount of heat generated or required per 1 kilogram of methane feed. The recycle ratio (R) is considered for the system configurations (B), (C) and (D). Increasing the recycle ratio increases the concentration of carbon dioxide in the cathode of the MCFC and consequently reduces the cathode resistance (voltage loss at the cathode) and can reduce heat requirement in the preheating unit on the cathode of the MCFC. In case of system configurations (A), (C) and (D), the reformed gas is divided into two streams and identified by a feed ratio (F). High feed ratio means that a large amount of the reformed gas is fed into the SOFC. The feed ratio revealed the proper fuel feed in each cell to maximize the system efficiency. Thus, the performance of the fuel cell systems varies, depending on the recycle ratio and the feed ratio. However, NiO formation should be avoided to increase the life span of the catalyst, and thus the NiO formation possibility is studied as well.

The simulation results show that for configuration (A), the produced power of the system decreases with increasing feed ratio (Figure 6.3(a)). More fuel is fed to SOFC when feed ratio increases and the rest is fed to operate the MCFC. This means power is mostly generated by the SOFC but it makes a large build-up of losses in the anode of the MCFC. A lower fuel concentration fed to the MCFC causes the open-circuit voltage to drop. However, the cathode losses are reduced due to an increase in the CO_2 concentration on the cathode side of the MCFC. These findings indicate that open-circuit voltage reduction is more influential than cathode losses reduction. That resulted in low power generation by the MCFC. It is clearly observed that adding the MCFC in the existing SOFC system can improve the system efficiency. The CEC rises with the feed ratio (Figure 6.3(b)) because the CO2 is more generated from the SOFC system (actually after burned in the afterburner) and less fuel is fed to the

MCFC. It is consequent to the fuel is not consistent with the CO_2 in the MCFC cathode and thus the CO_2 does not transfer to anode side. The fuel cell system (A) prefers operation at a lower feed ratio, but not too low because NiO will be formed at a lower feed ratio. At the maximized efficiency of this configuration, it is clearly observed that the large heat requirement is at the air preheating unit and the exhaust gas still has a high energy content that can be useful. Net heat duty from this design still generates heat as shown in Figure 6.3(c).

a

b

c
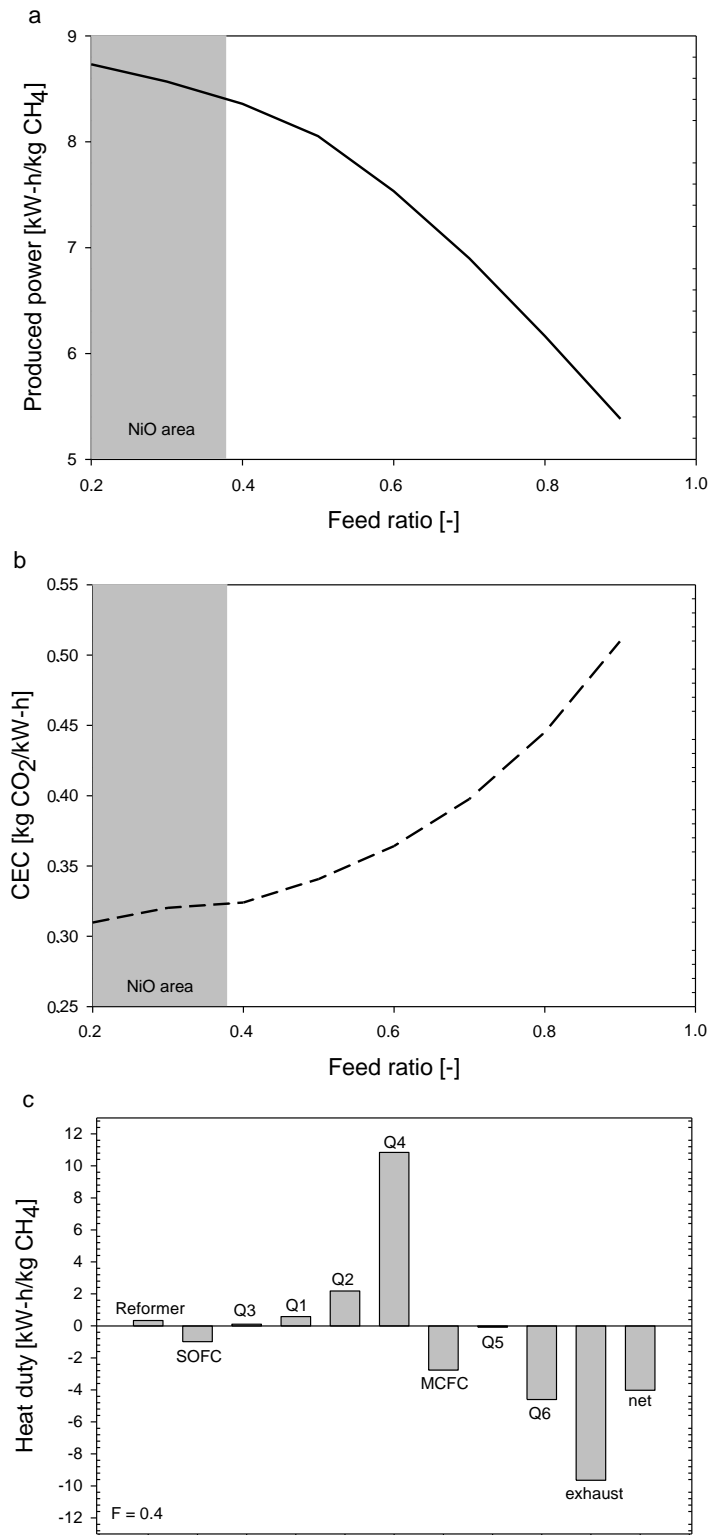
Figure 6.3 Performance of Configuration (A): (a) produced power, (b) CEC and (c)

Heat duty

For system configuration (B), the exit-gas from the anode of the SOFC contains CO and H_2. These fuels can be synthesized on the anode of SOFC via steam reforming and water-gas-shift reactions. Considering the gas compositions in the SOFC, all CH_4 was shifted to CO and H_2. It seems that SOFC performs as a fuel processor because the amount of CO and H_2 became higher at the outlet of the SOFC. As a result, MCFC can directly use the exit-gas from anode of SOFC to improve a fuel utilization and produce additional electrical power. The produced power is improved by increasing the recycle ratio (Figure 6.4(a)) because of higher CO_2 concentration in the cathode of MCFC at higher recycle ratio. A higher recycle ratio also decreases the CEC because more CO_2 is recirculated in the system. The partial recirculation of exhaust gas from the burner can decrease the size of cathode preheating unit because the mixing temperature can reduce the temperature gradation of preheating unit. Since the SOFC has a higher operating temperature than the MCFC, the heat exchanger (Q5) is used to remove heat in the outlet stream. Figure 6.4(b) shows that with this fuel cell system configuration, there is more valuable heat that can be further used. Moreover, NiO formation does not appear in this design, which is the advantage of this system configuration. It is noted that this system prefers operation at a high recycle ratio.

a

b
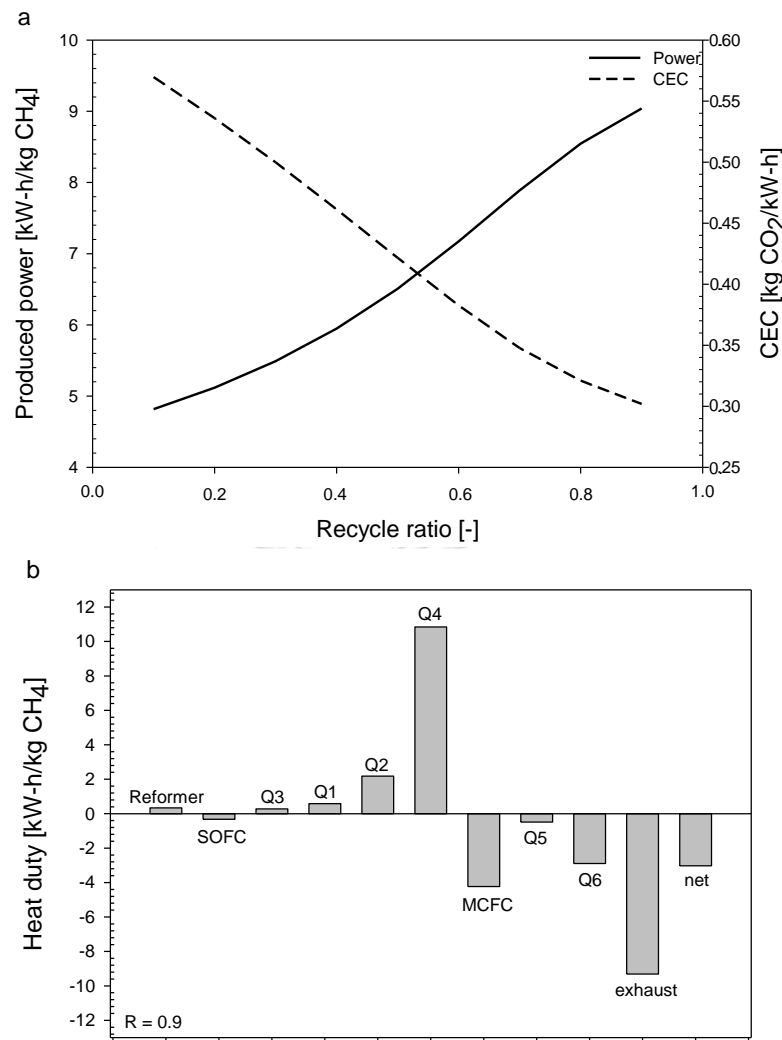
Figure 6.4 Performance of Configuration (B): (a) produced power and CEC and (b)
Heat duty

The results of system configuration (C) (Figure 6.5(a)) show that the system requires some fuel fed in SOFC for producing power and the rest is for MCFC in order to circulate CO_2 and produce additionally power. High recycle ratio also improves the performance. Nevertheless, too large an increase in the fuel fed to SOFC causes the efficiency to drop dramatically at a high recycle ratio. Increasing the feed ratio raises the produced power of the fuel cell system as a result, but if the feed ratio is too high, the efficiency becomes constant at a high recycle ratio. This figure also shows that the system operating at medium feed ratio and high recycle ratio produces more electricity, even though more fuel is fed to the SOFC. The CEC initially

decreases to its minimum and then slightly increases at a high feed ratio (Figure 6.5(b)). As mentioned earlier, recycle ratio is the main key of the CEC reduction. The minimum CEC can meet a high recycle ratio. Thus, a moderate feed ratio and high recycle ratio are selected for this design in order to achieve the best performance and avoid NiO formation. Since air will be changed with the feed ratio at the same rate, the heat duty of the preheating unit (Q4) can be reduced and the heat exchanger Q6 required the heat instead (Figure 6.5(c)). Net heat is also negative (heat generation) for this design.
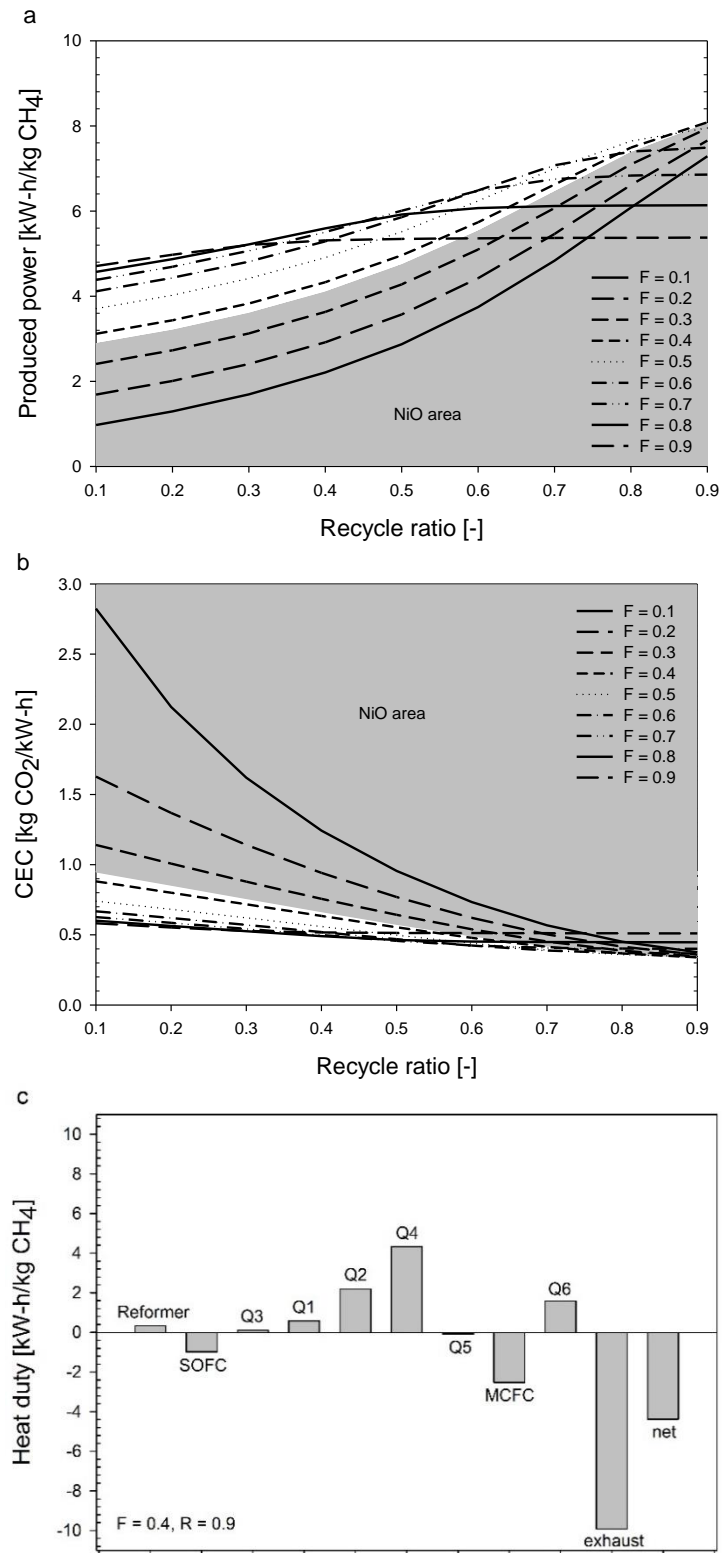
Figure 6.5 Performance of Configuration (C): (a) produced power, (b) CEC and (c) Heat duty

System configuration (D) differs from configuration (C) in that the exit-gas from anode of SOFC is mixed with reformed gas and is fed to MCFC. This fuel can be more useful in the MCFC but the produced water from the SOFC also dilutes the reformed gas too. The simulation results (Figure 6.6(a)) show that the system power generation can be increased by increasing both feed ratio and recycle ratio. However, the produced power increases slightly at a high feed ratio and a high recycle ratio. At a feed ratio of 0.8, it can be observed that there is no data at a recycle ratio of 0.1, as there is not enough fuel to operate the MCFC. Figure 6.6(b) show the effect of feed and recycle ratio on CEC. It is obviously observed that system can further reduce carbon dioxide by increasing the recycle ratio and feed ratio. In order to avoid the formation of NiO and achieve high power, the system requires operation at a moderate feed ratio and a high recycling ratio. When it is operated at a moderate feed ratio, the CEC of the system will not be as low as it could be. The system can achieve the minimum CEC by high feed and recycle ratio operation but it will lose some power. Based on maximum power production, much heat is produced as shown in Figure 6.6(c).
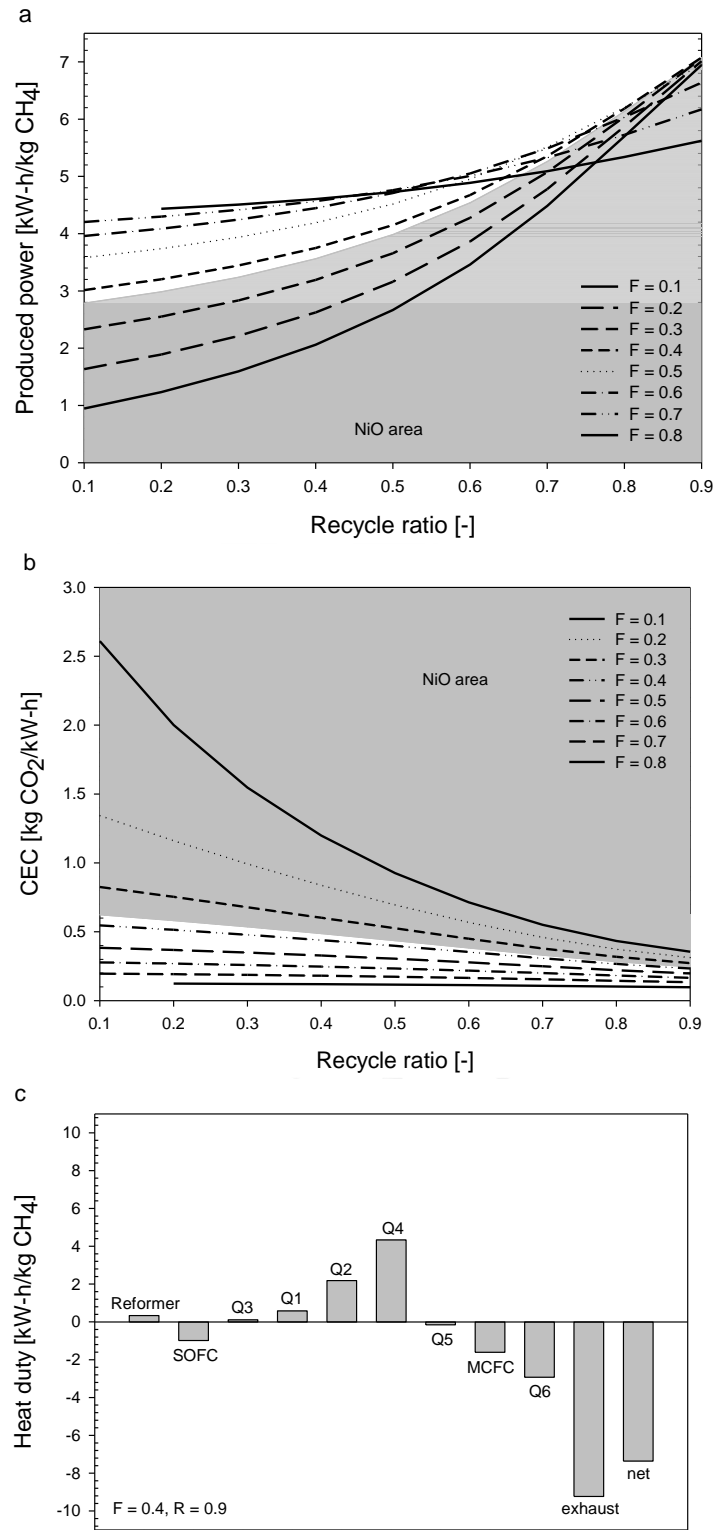
Figure 6.6 Performance of Configuration (D): (a) produced power, (b) CEC and (c)

Heat duty

Figure 6.7(a)-(c) compares the produced power, CEC and heat duty of different fuel cell systems at their optimal operating conditions. This figure clearly shows that system configuration (B) provides the highest produced power, but it is not the lowest CEC. System configuration (D) can provide the lowest CEC and the highest generated heat. The lowest heat generation is provided by design (B). This is because chemical energy is more converted into electrical energy in design (B), causing lower heat generation. If power generation is a high priority, we recommend the system configuration (B). If carbon dioxide emission is the first priority, configuration (D) is the best choice but feed ratio should be carefully controlled to avoid NiO.
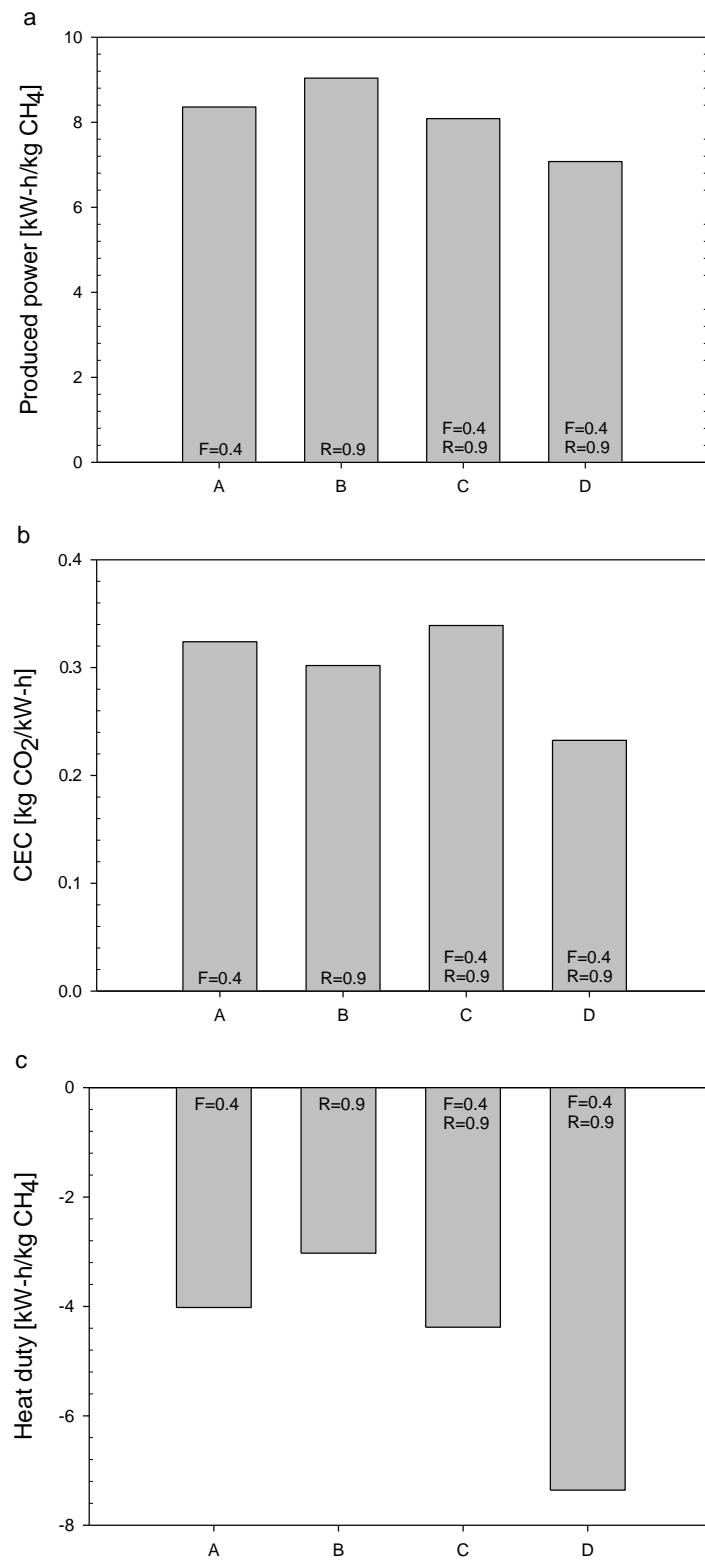
Figure 6.7 Comparing Performance of Each Configuration: (a) produced power, (b) CEC and (c) Heat duty

6.4 Conclusions

This study investigated and compared the performance of the SOFC and the MCFC integrated systems with different configurations in terms of power generation, CO_2 utilization, heat duty and NiO formation possibility. The simulation results indicate that the configuration affects the performance of the integrated system in different ways. Four configurations are proposed, including adding the MCFC on existing an SOFC, in series, in parallel and in a series-parallel combination configuration. All configuration can improve the power generation and carbon dioxide utilization. However, the optimal operation in each design showed two interesting configurations that are series (B) and series-parallel combination (D). Based on power generation improvement, system (B) is suitable. System (D) is the one of the most suitable for carbon dioxide utilization.
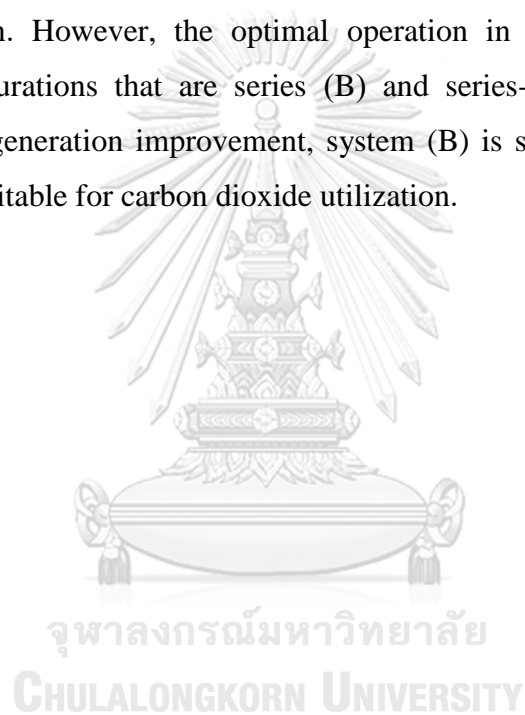
CHAPTER 7

Control structure design of a solid oxide fuel cell and a molten carbonate fuel cell integrated system

This chapter studies control structure design of the SOFC and the MCFC integrated system. A procedure for select an active constraint and self-optimizing variables is presented. Moreover, the relative gain array (RGA) considered as a controllability index for the selection of input-output pairings is also implemented. Portions of chapter were appeared in Jienkulsawad et al. (2017).

7.1   Introduction

Most power plants are generally based on fossil fuels and are the largest source of CO_2 emissions (Klein, 2016). High-temperature fuel cells, such as SOFCs (solid oxide fuel cells) and MCFCs (molten carbonate fuel cells), have been considered as alternative reliable power sources for decades because they have higher electrical efficiency and thus a lower environmental impact. Moreover, high-temperature fuel cells have been reported by both theoretical and experimental studies to have a great fuel flexibility, even to the extent of a fuel consisting of tar, as reported by Baldinelli et al. (2006). However, methane is selected as the fuel feed because it is easily obtained from many petrochemical and biochemical processes (Mahdy et al., 2014).

In general, a stand-alone SOFC cannot completely use all the fuel within itself, as NiO forms and corrosion occurs at the anode of the SOFC (Nehter, 2007). The study by Parhizkar and Roshandel (2017) showed that under the optimum operating conditions, the SOFC should be operated at a moderate fuel utilization to avoid a long-term cell degradation, resulting in a remaining fuel in the anode off-gas. Many researches have been carried out to enhance the SOFC system performance. Zhang et al. (2017) proposed the hybrid SOFC system with a thermoelectric generator and thermoelectric cooler to recover the waste heat from SOFC. However, the proposed SOFC system did not deal with the remaining fuel in the exhaust gas. Hosseinpour et al. (2017) studied a cogeneration system based on an SOFC integrated with a Stirling engine. The remaining fuel in the SOFC outlet was combusted to increase the

temperature of the exhaust gas before it was fed to the Stirling engine. Sarmah and Gogoi (2017) designed the combined SOFC power system with gas turbine and steam turbine cycles by using the remaining fuel for a gas turbine cycle. Zhang et al. (2017) used a recycling strategy to enhance the SOFC system efficiency; an anode off gas was recirculated to the reformer providing steam and heat for the reforming process. Alternatively, the integration of SOFC with other fuel cell types to use the remaining fuel in the SOFC outlet for additional power generation has been explored. A combined SOFC and proton exchange membrane fuel cell (SOFC-PEFC) system was proposed by Obara (2010); however, several purifying units were required to treat the exhaust gas from SOFC before it can be fed to the PEFC. Two-staged SOFCs, low and high-temperature SOFCs, with a serial connection were studied by Araki et al. (2006). Patcharavorachot et al. (2010) investigated the performance of the oxygen-ion and proton-conducting electrolyte SOFC hybrid system. Regarding the operation of MCFCs, syngas can be used as a fuel. Moreover, MCFCs need CO_2 and O_2 to promote CO_3^{2-} as an electron carrier. In other words, CO_2 is useful for power generation in an MCFC (Wee, 2014), and the remaining fuel and CO_2 exhaust from the SOFC can be used directly in an MCFC to generate more power (McPhail et al., 2011). Thus, the SOFC and MCFC integrated system can be a potential solution for increasing fuel and carbon dioxide utilization and power generation. Our previous simulation studies showed that the integrated SOFC-MCFC system has better system performance in terms of power generation and carbon dioxide emission (Jienkulsawad and Arpornwichanop, 2016). The series configuration is selected because it has no possibility for NiO formation under optimal operating conditions (Jienkulsawad et al., 2015). The operating parameters, such as temperature and fuel utilization, play an important role in the performance.

Although the integrated fuel cell system has shown an improved overall efficiency, it leads to a complicated process involving many controlled and manipulated variables and requires an efficient control system. Regarding the control of a fuel cell system, Bizon et al. (2015) showed that a standalone renewable/fuel cell hybrid power source had 4 possible control structures for the load tracking problem and each control topology is efficient for different loads. Chaisantikulwat et al. (2008) studied the control system of an SOFC and indicated that cell voltage is a key variable

to be controlled by adjusting the hydrogen concentration in the fuel. Huang et al. (2011) stated that the control systems of a fuel cell system were targeted for the operation, temperature, power and fuel utilization. Braun et al. (2012) categorized the objective of an SOFC control system, which was mostly related to its performance (to meet a design output), in terms of safety and operation (to maintain inputs and outputs within desired bounds). To date, control of fuel cells has mostly been focused on stabilizing control and less on economic control. In addition, depending on the objective of the control strategy, different manipulated variables possibly can be used to control the fuel cells. For example, the air flow rate can be used to control either the cell temperature or fuel utilization. Although the economic control for an SOFC was studied by Chatrattanawet et al. (2015), there are still some gaps when economic control is applied to the SOFC and MCFC integrated system. The previous study (Jienkulsawad and Arpornwichanop, 2016) showed that in the integrated system, the MCFC operation depends on the SOFC operation and their operating points were changed to maximize total power. Thus, the control of such a system could require a different control structure to achieve the best profit.

This work focuses on a control structure design for the series configuration of the SOFC-MCFC integrated system, **Figure 7.1**. The control structure design based on an economic steady-state optimization analysis is performed to select suitable manipulated variables and controlled variables of the integrated system (Skogestad, 2004). At present, carbon dioxide emissions are an important concern for power plants (Aghaie et al., 2016) and a carbon tax is considered as a part of the economic objective function. Constraints are included to ensure safe and feasible operation, e.g., a constraint to avoid NiO formation. Active constraint regions are identified and self-optimizing controlled variables are selected for the remaining unconstrained variables. Moreover, the throughput manipulator (TPM) is selected and economic control loops based on this analysis are proposed.
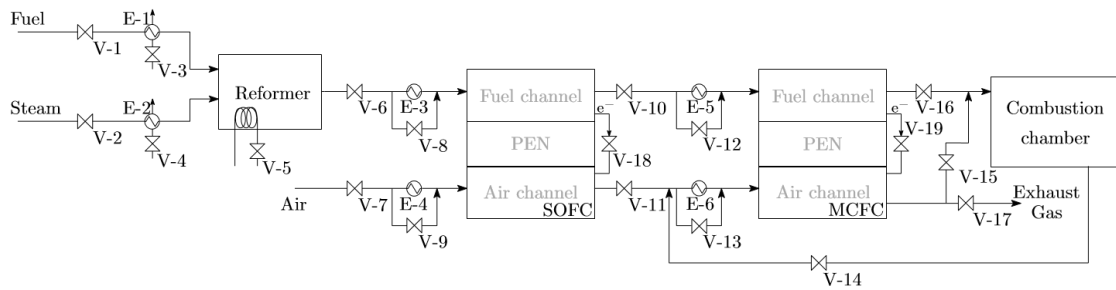
Figure 7.1 series configuration of SOFC and MCFC integrated system

7.2 Control structure design

The stepwise procedure of a control structure design starts by formulating the economic operational objective and the operational constraints. The procedure is divided into two main parts; top-down and bottom-up as shown in **Figure 7.2**, is highlighted.

จุฬาลงกรณ์มหาวิทยาลัย

CHULALONGKORN UNIVERSITY
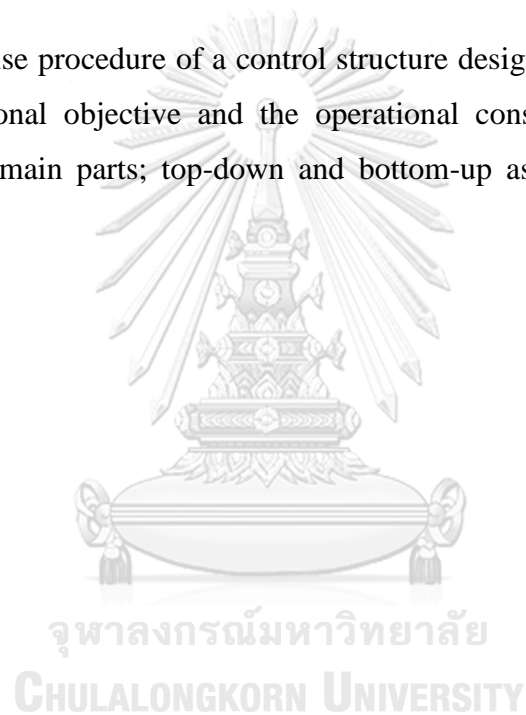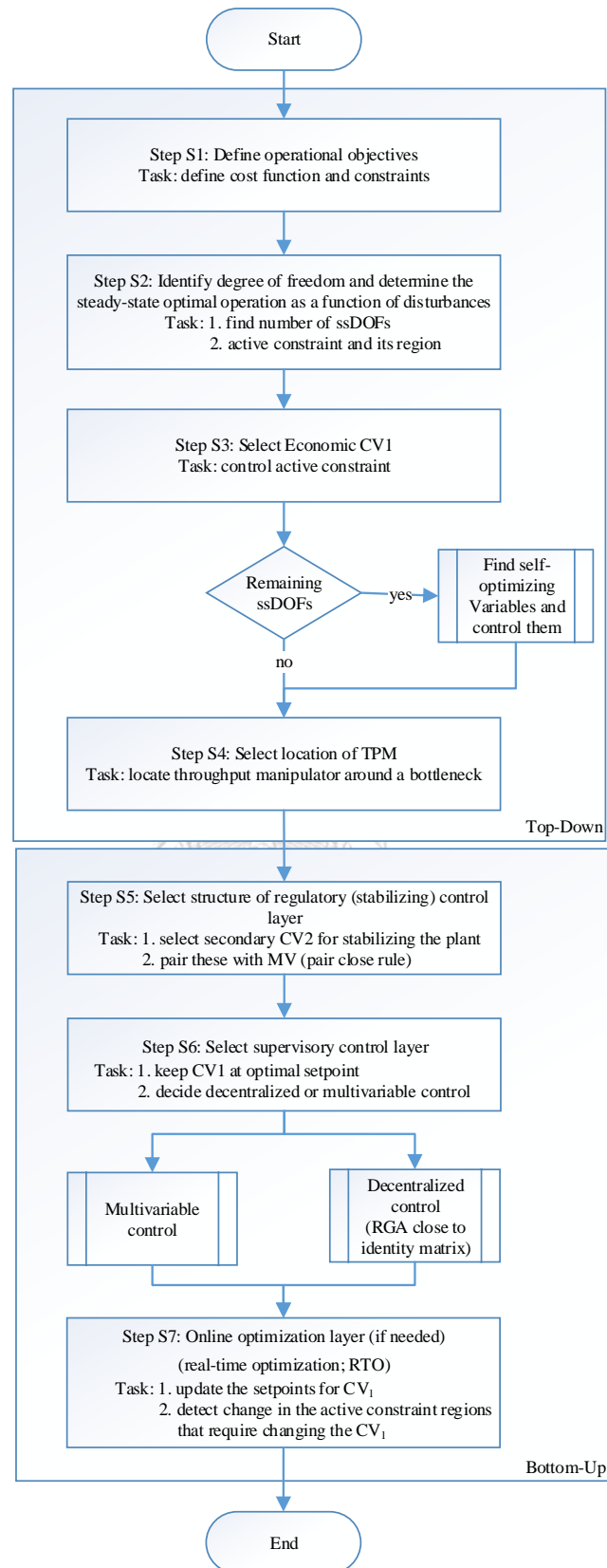
Figure 7.2 Flow chart of control structure design procedure

Step S1: Define operational objectives

In this study, each of the SOFC and MCFC is simulated based on one cell because fuel cells can be scaled up by stacking them up. Thus, the cost function (or negative profit function) is defined per kg of methane feed as in equation (7.1). The cost function does not include the cost of energy in exchangers because the previous work showed this system does not have an external heat requirement at steady state operation.

$$J = -\left(\frac{P_W \cdot P_{ele}}{\dot{m}_{CH_4}^0} - \frac{\dot{m}_{CO_2} \cdot Tax_{CO_2}}{\dot{m}_{CH_4}^0} - P_{CH_4} \right) \quad \left[\$ \left(kg\,CH_4 \right)^{-1} \right]$$
(7.1)

where P_W = generated power from system [kW]

P_{ele} = electricity price [$ (kWh)$^{-1}$]

$\dot{m}_{CH_4}^0$ = CH$_4$ feed to system [kg CH$_4$ s^{-1}]

$\dot{m}_{CO_2}$ = CO$_2$ released from system [kg CO$_2$ s^{-1}]

Tax_{CO_2} = CO$_2$ tax [$ (kg CO$_2$)$^{-1}$]

P_{CH_4} = CH$_4$ price [$ (kg CH$_4$)$^{-1}$]

This cost is to be minimized subject to the following constraints:

- No carbon formation on fuel cells (evaluated by carbon activity).
- For SOFC (Aguiar et al., 2005)

C1   fuel channel feed temperature ($T_{0f,S}$) is in the range 973 - 1073 K

C2   air channel feed temperature ($T_{0a,S}$) is in the range 973 - 1073 K

C3   maximum temperature difference ($T_{f,S} - T_{0f,S}, T_{a,S} - T_{0a,S}$) is 400 K. (maximum temperature gradient of 10 K cm^{-1})

C4   minimum cell voltage (E_S) is 0.55 V.

C5   maximum fuel utilization ($U_{f,S}$) is 85% to prevent NiO formation (Nehter, 2007).

C6   the allowed air ratio to the system (λ_{air}) is between 2 and 14.

- For MCFC (Greppi et al., 2013)

  C7   fuel channel feed temperature ($T_{0f,M}$) is in the range 823-873 K

  C8   air channel feed temperature ($T_{0a,M}$) is in the range 823-873 K

  C9   maximum temperature inside the stack ($T_{f,M}$, $T_{a,M}$, $T_{P,M}$, $T_{I,M}$) is 963

K.

  C10   maximum fuel utilization ($U_{f,M}$) is 75%.

  C11   minimum O_2 mole fraction at cathode inlet ($y_{O_2,M_{0a}}$) is 8%.

  C12   minimum CO_2 mole fraction at cathode inlet ($y_{CO_2,M_{0a}}$) is 4%.

  C13   minimum H_2 mole fraction at anode outlet (y_{H_2,M_f}) is 6%.

In addition, the operating temperature of the SOFC should be higher than that of the MCFC to promote more H_2 via water-gas-shift reaction (Jienkulsawad and Arpornwichanop, 2016) and all flow rates must be non-negative.

Step S2: Identify the degrees of freedom and determine the steady-state optimal operation as a function of disturbances

To determine the steady-state optimal operation, the steady-state degrees of freedom (ssDOFs) and important disturbances need to be identified. It is found that the system has 19 degrees of freedom for control, as shown by the 19 valves in Figure 3. The last two "valves" (V-18 and V-19) represent the current density by each of the fuel cells. In this study, 11 operating variables in the system are assumed to be specified, i.e., fuel feed rate, steam feed rate, fuel and water feed temperatures, reformer operating temperature, and operating pressures of the reformer, fuel and air channels of fuel cells, and the combustion chamber. The number of remaining steady-state (and dynamic) degrees of freedom is:

$$N_{SS} = N_{valves} - N_{0SS} - N_{specs}$$
$$= 19 \quad - 0 \quad - 11 \quad = 8$$

where N_{SS} is the number of ssDOFs, N_{valves} is the number of all valves in the system including adjustable power inputs (current density, V-18 and V-19), N_{0SS} is the

number of valves with no steady-state effect (none in our case), and N_{specs} is the number of specified conditions.

The eight remaining degrees of freedom may be considered to be related to air feed rate, SOFC feed temperatures (anode, cathode), MCFC feed temperatures (anode, cathode), current densities and the exhaust split ratio. Next, the main goal is to identify the active constraints which need to be controlled to maximize profit. Note that active constraints may change with disturbances resulting in different active constraint regions. Normally, each region requires a different control structure but if a neighboring region has a small loss in its cost, the same control structure might be acceptable. When there are many possible disturbances in the system, then there is a multi-dimensional disturbance space. However, a two-dimensional space is more practical to plot. Steam is normally fed in ratio to the fuel (methane) for the avoidance of carbon formation but for our system the ratio to avoid carbon depends on the operating conditions. Thus, two important disturbances are selected, namely, the fuel feed flow rate and the steam feed flow rate.

Prices are not considered as disturbances even though they often change. Paul et al. (2013) showed that prices of fuel and electricity depend on the carbon tax and they are used in this work. If the carbon tax increases, the electricity price increases in the same manner. Thus, it will not affect the optimal solution.

The range of disturbances is considered to be a 50 percent change from the nominal values. To locate the active constraint regions, the disturbance space was gridded. Each point in the grid was used to minimize the cost J with respect to the eight degrees of freedom (u) for the two given disturbances (d). The steady-state optimization problem can be formulated as:

$$\min_{u} \quad J(x,u,d) \tag{7.2}$$

$$\text{subject to} \quad f(x,u,d) = 0 \tag{7.3}$$
$$c(x,u,d) \leq 0$$

where J is the economic objective, f represents the process model equations, and c represents the process constraints.

The active constraint regions of this system are shown in **Figure 7.3** and **Table 7.1** lists which constraints are active in each region. From the table, the active

constraints of this system are mostly found in the MCFC. This is because the MCFC uses the remaining fuel and oxygen from the SOFC.
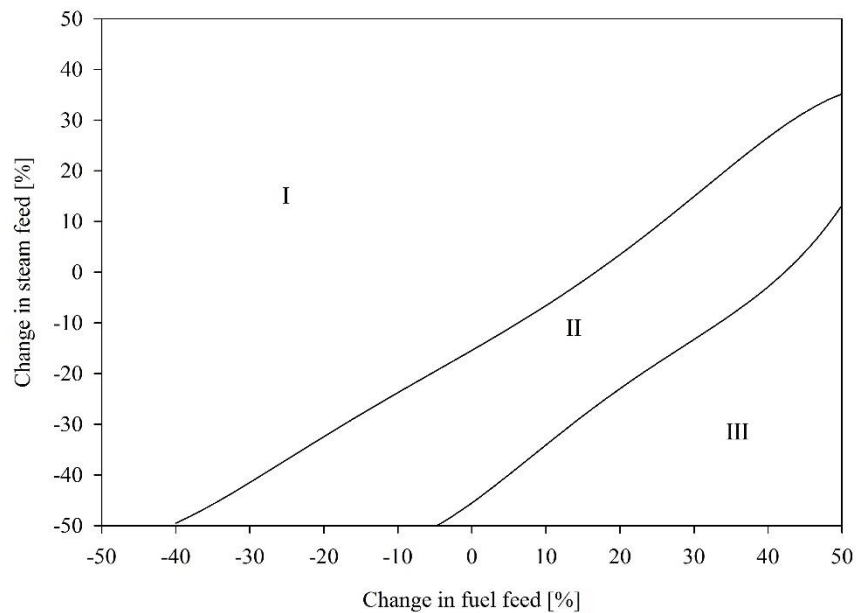
Figure 7.3 Actively constrained regions for the integrated system

Table 7.1 Active constraint in each region

Region	Active constraint	Number of remaining DOFs
I	$T_{0f,S}$, $T_{0a,S}$, $y_{O_2,M_{0a}}$, y_{H_2,M_f}	4
II	$T_{0f,S}$, $T_{0a,S}$, $y_{O_2,M_{0a}}$, y_{H_2,M_f}, $U_{f,M}$	3
III	$T_{0f,S}$, $T_{0a,S}$, $y_{O_2,M_{0a}}$, $U_{f,M}$	4

Further discussion on active constraints

At the nominal value of the disturbances, the system will be in region I and the following constraints are active: $T_{0f,S}$ (C1), $T_{0a,S}$ (C2), $y_{O_2,M_{0a}}$ (C11) and y_{H_2,M_f} (C13). Active constraints in three regions can be divided into two groups: always active and not always active.

Always active — The SOFC feed temperature constraints, $T_{0f,S}$ and $T_{0a,S}$ are active in all regions because power generation should be maximized (Jienkulsawad

and Arpornwichanop, 2016). The minimum constrained on $y_{O_2,M_{0a}}$ (C11) in the MCFC air channel feed is always active to avoid physical damage to the MCFC and CO_2 dilution in the MCFC air channel.

Not always active —The minimum MCFC H_2 concentration, y_{H_2,M_f} (C13) is active nominally (region I) even if there is a small change in fuel and steam feed (region II). However, it becomes inactive for a large increase in fuel feed and a large decrease in the steam feed (region III). This is because hydrogen is formed via the steam reforming and water-gas shift reactions and it is higher than what the MCFC requires for separating carbon dioxide as shown in Figure 7.4 (region III). Therefore, H_2 increases as the fuel and steam feeds increase. Even though the SOFC electrochemical reaction rate (Figure 7.4(c)) is increasing with an increase in the fuel feed and a decrease in the steam feed, SOFC fuel utilization (Figure 7.5(b)) dramatically drops in region III, which means the SOFC uses less hydrogen compared to the hydrogen content inside the SOFC unit, and y_{H_2,M_f} thus becomes inactive.

$U_{f,M}$ is inactive in region I. $U_{f,M}$ tells how much of the hydrogen in the MCFC is used to produce electricity or used to separate CO_2. It also implies hydrogen is not always completely used in the system. This system does not use pure hydrogen; the hydrogen is produced from the steam reforming and water-gas shift reaction. An increase in fuel feed also produces more carbon dioxide (Figure 7.6(b)). The MCFC will use more hydrogen to separate carbon dioxide. That results in $U_{f,M}$ being active.

The rate of the steam reforming and water-gas-shift reaction (Figure 7.4(a) and (b)) also shows that the MCFC acts as the second stage for hydrogen generation, and it increases the total power generation as shown in Figure 7.5(a). The power increases as the fuel feed increases but it also increases the cost (Figure 7.6(c)) because fuel cells have fuel utilization limitation. This corresponds with energy efficiency (Figure 7.6(a)) which shows that the system has less efficiency as the fuel feed increases.

The carbon dioxide emission coefficient (CEC) describes how much CO_2 is released from the power generation system, even though CEC does not directly appear in the cost function. CO_2 more releases when increasing in steam and fuel feed.
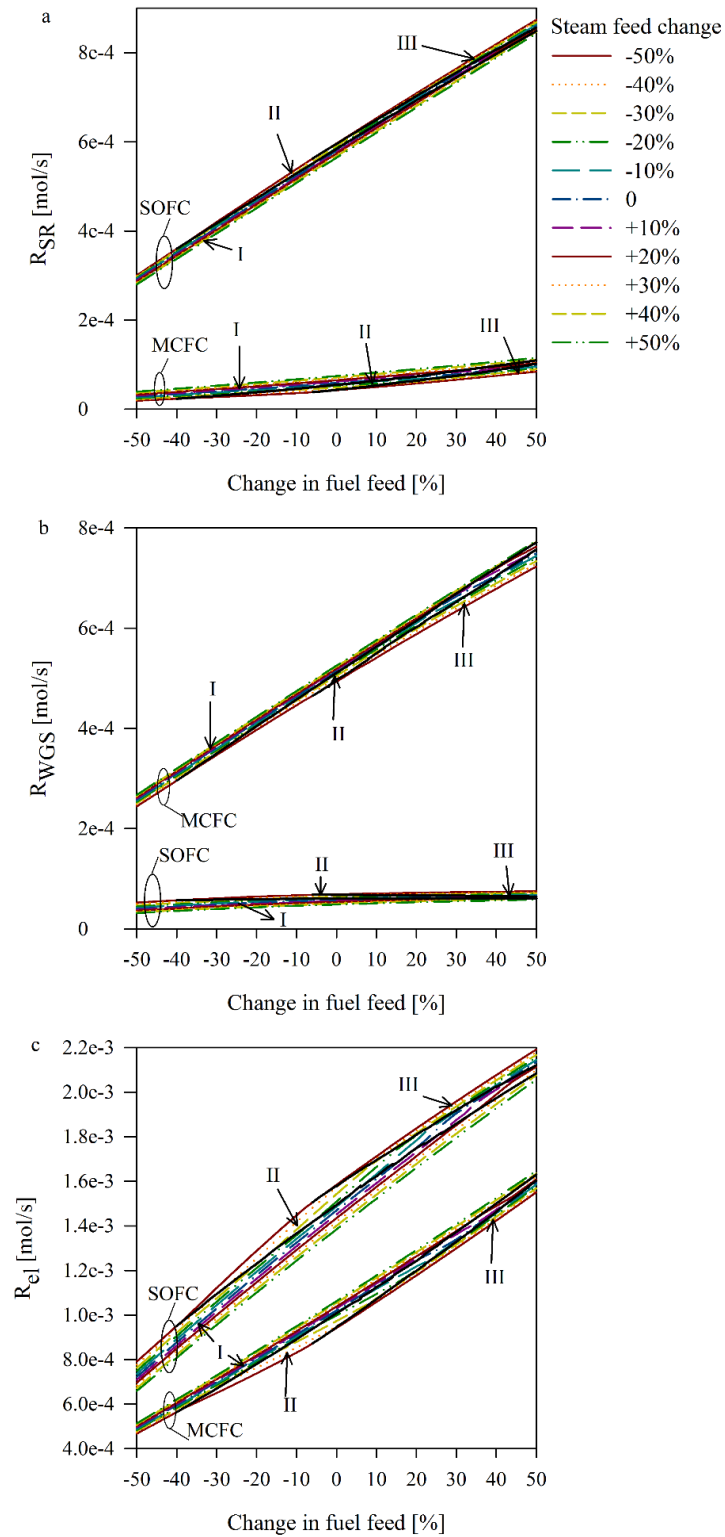
Figure 7.4 Rate of reactions for (a) steam reforming (i), (b) water-gas-shift (ii) and (c) electrochemical reaction (v, vii)
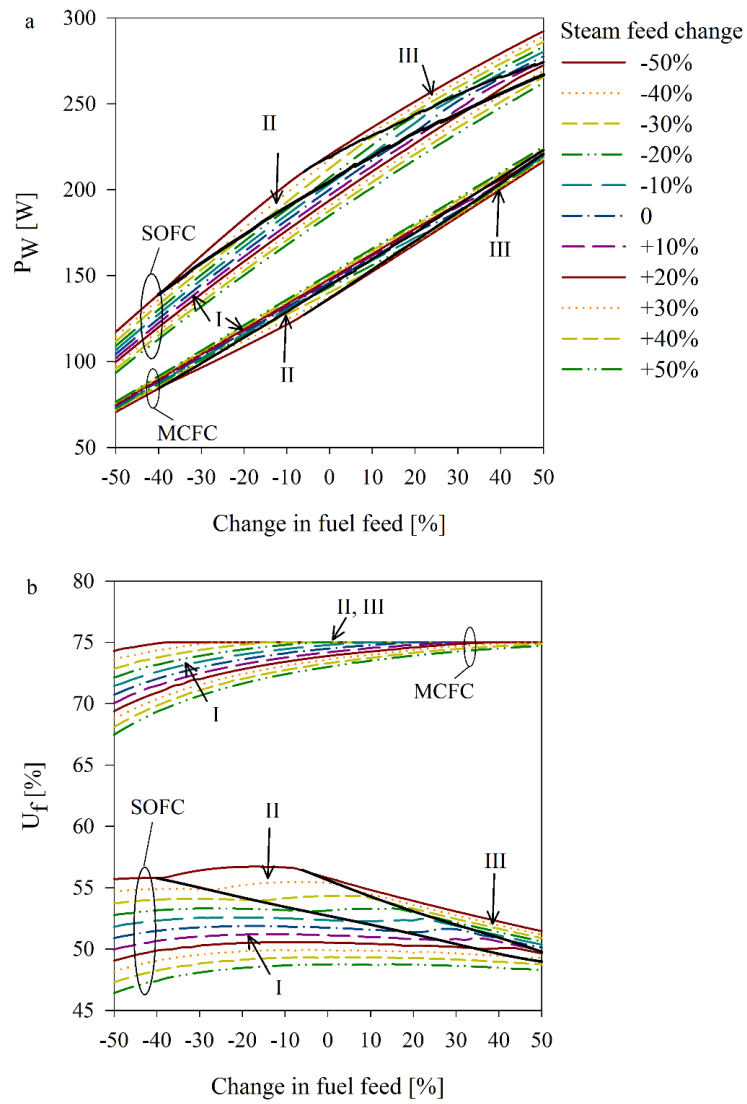
Figure 7.5 (a) Power ($P_{W,S}$, $P_{W,M}$) and (b) fuel utilization ($U_{f,S}$, $U_{f,M}$) of the SOFC

and MCFC
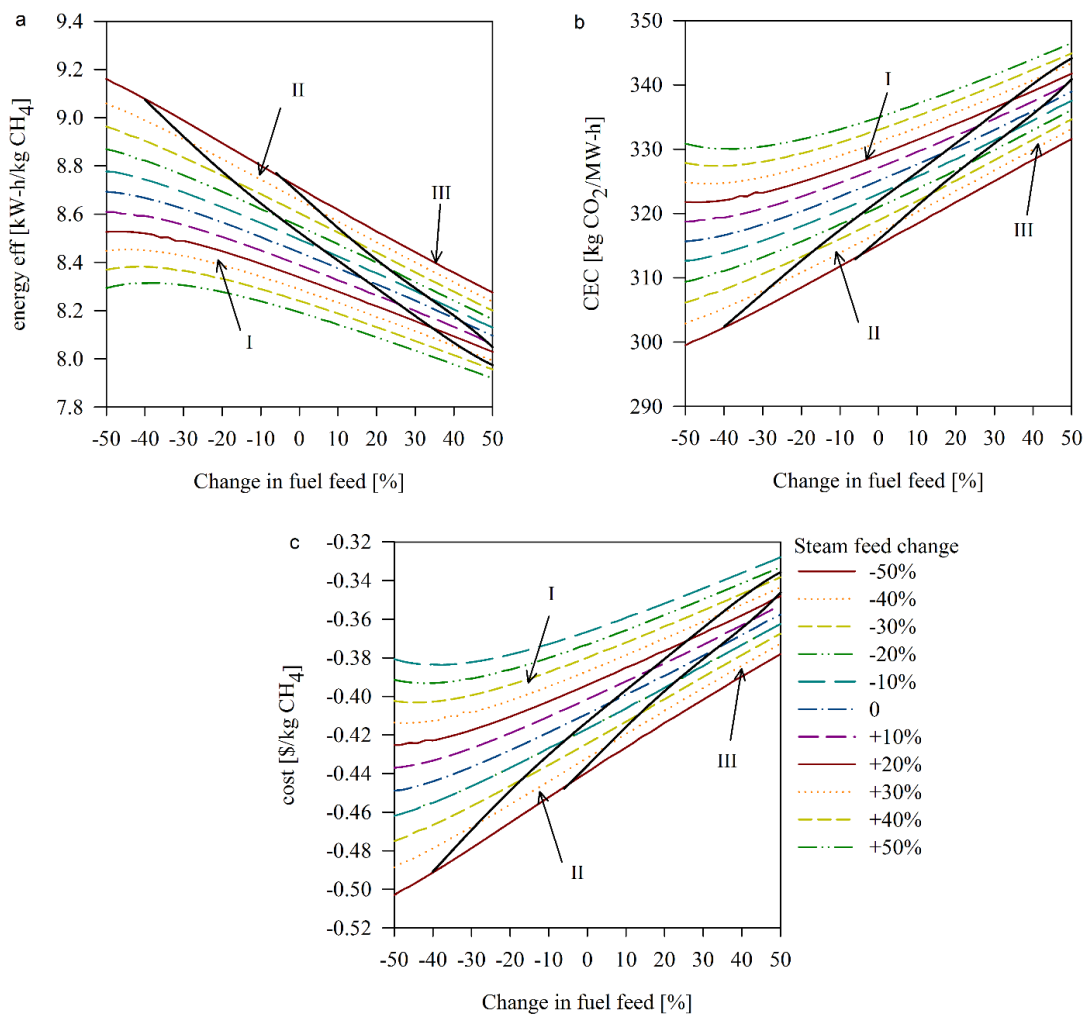
Figure 7.6 (a) Energy efficiency, (b) CEC and (c) cost function of the integrated system

Step S3. Select Economic CV$_1$

According to the simple rules for economic plant-wide control by Minasidis et al. (2015), active constraints should always be controlled (rule 1 of step S3). For the remaining unconstrained degrees of freedom, self-optimizing control (SOC) variables which give close-to-optimal operation when held at constant setpoints should be controlled, even when there are disturbances. Since there are 3 regions, three CV$_1$ sets must be theoretically identified. Table 7.2 shows the cost J and some other key variables for expected disturbances in each region. They are used as reference points for the selection of SOC variables. Note that active constraint values should be

considered as disturbances as well; see Table 7.3. Hence, four disturbances are considered to evaluate the choice of SOC variables. The choice of controlled variable candidates CV_1 should follow Skogestad's heuristic rules. Region II has fewer unconstrained DOFs than other regions. Here, the control structure needs to be simplified by using the control structure in region II as the base for the structure for all regions, if possible. In other words, the use of the same active constraint set for all regions is preferable. Note that three regions have different optimal active constraint sets. Candidates for self-optimizing variables (CV) will be focused on in the MCFC and combustion chamber. This is because $T_{0f,S}$, $T_{0a,S}$ and $y_{O_2,M_{0a}}$ are always active, the pressures of the fuel and air channels are specified and, moreover, because the MCFC is the bottleneck of the system. Some CV_1 candidates are temperatures (MCFC outlet, burner inlet and outlet), voltages and gas compositions (y_{CH_4,M_f}, y_{H_2,M_f}, $y_{H_2O,\{M_f,B_0,B,ex\}}$, $y_{CO_2,\{B,ex\}}$ and $y_{O_2,\{B,ex\}}$). Note that CH_4, H_2 and O_2 are key compositions for fuel cells. CO_2 is very important for the MCFC. H_2O can be measured by humidity sensors. The temperature ratios $T_{f,M}/T_{a,M}$, $T_{f,M}/T_{0f,M}$ and $T_{a,M}/T_{0a,M}$ are considered as candidates as well because these ratios are changed in the same manner to keep the MCFC at its constraints.

Table 7.2 Cost function and active constraint values in each region

Variables	Value at nominal operating point in region I	Region		
		I	II	III
Change in fuel feed [%]	0	0	15	35
Change in steam feed [%]	0	0	-15	-30
Cost function J [\$ (kg CH$_4$)$^{-1}$]	-0.4015	-0.4015	-0.3977	-0.3842
$U_{f,M}$ [%]	(74.48)*	(74.48)*	75	75
$T_{0f,S}$ [K]	1073	1073	1073	1073
$T_{0a,S}$ [K]	1073	1073	1073	1073
y_{H_2,M_f} [-]	0.0600	0.0600	0.0600	(0.0614)*
$y_{O_2,M_{0a}}$ [-]	0.0800	0.0800	0.0800	0.0800

*( ) indicate optimal unconstrained value.

Table 7.3 Main disturbances in Step S3

Disturbance	Region					
	I		II		III	
	Ref. point	Change	Ref. point	Change*	Ref. point	Change*
Change in fuel feed (d$_1$) [%]	0	±5%	15	±2.5%	35	±2.5%
Change in steam feed (d$_2$) [%]	0	±5%	-15	±2.5%	-30	±2.5%
$T_{0f,S}$ (d$_3$) [K]	1073	±5%	1073	±2.5%	1073	±2.5%
$T_{0a,S}$ (d$_4$) [K]	1073	±5%	1073	±2.5%	1073	±2.5%

*A small change is used to avoid entering regions I or III (evaluating the loss within the region).

As mentioned, the use of the same control structure in all regions is preferable, if possible. Hence, good candidate sets are first evaluated in region II. Because $U_{f,M}$ is active in regions II and III and $y_{\mathrm{H_2},M_f}$ is active in regions I and II, $U_{f,M}$ and $y_{\mathrm{H_2},M_f}$ are candidates in regions I and III, respectively. The loss from keeping a candidate CV at a constant value is evaluated by equation (7.4).

$$Loss = J(u,d) - J(u_{opt},d) \tag{7.4}$$

In region II, there are 3 remaining unconstrained DOFs thus 3 CV variables must be selected. The totals of the losses from the 4 disturbances for different CV candidates are shown in Figure 7.7(b) with respect to Table 7.4. As seen in Figure 7.7(b), there is a candidate set that provides the smallest total loss (RII1) given by selecting $T_{0a,M}$, $T_{f,M} / T_{0f,M}$ and $y_{\mathrm{H_2O},B_0}$ as CV candidates.
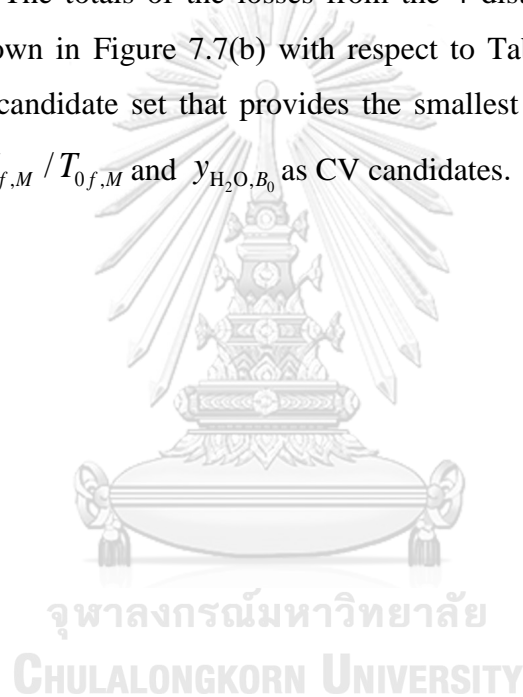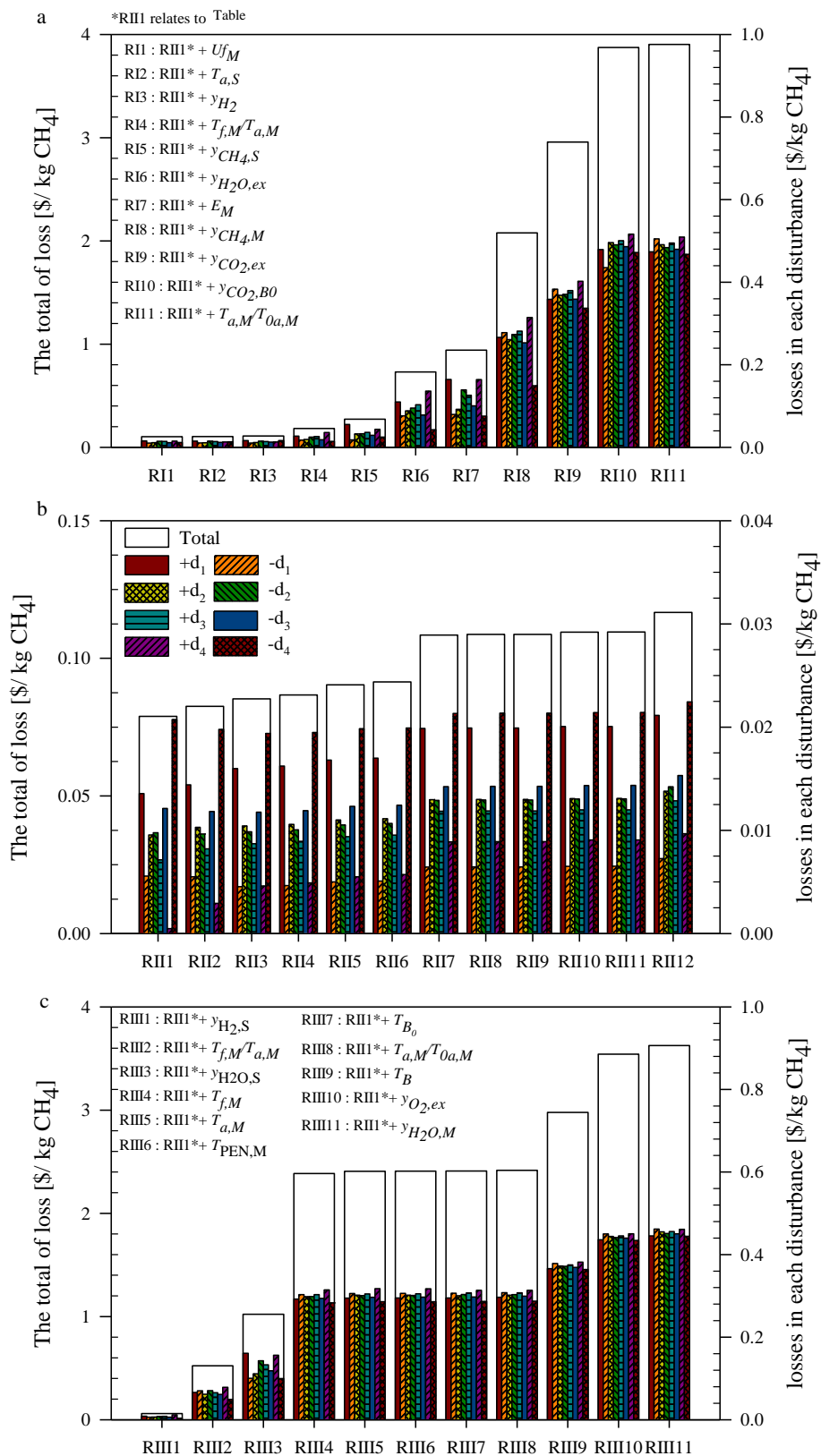
Figure 7.7 Losses from different candidate sets in Region I (a), II (b) and III (c)

Table 7.4 Candidate CV sets in region II with respect to Figure 7.7(b)

Set	Candidate CVs		
RII1	$T_{0a,M}$	$T_{f,M}/T_{0f,M}$	y_{H_2O,B_0}
RII2	$T_{0f,M}$	$T_{a,M}/T_{0a,M}$	$y_{O_2,B}$
RII3	$T_{0a,M}$	$T_{f,M}/T_{0f,M}$	$y_{O_2,B}$
RII4	$T_{0f,M}$	$T_{0a,M}$	$y_{O_2,B}$
RII5	$T_{0a,M}$	$T_{f,M}/T_{0f,M}$	$y_{O_2,ex}$
RII6	$T_{0f,M}$	$T_{0a,M}$	$y_{O_2,ex}$
RII7	$T_{0a,M}$	$T_{a,M}$	$y_{CO_2,B}$
RII8	$T_{a,M}$	$T_{f,M}/T_{0f,M}$	$y_{CO_2,B}$
RII9	$T_{0f,M}$	$T_{a,M}$	$y_{CO_2,B}$
RII10	$T_{0f,M}$	$T_{f,M}$	$y_{CO_2,B}$
RII11	$T_{0a,M}$	$T_{f,M}$	$y_{CO_2,B}$
RII12	$T_{0f,M}$	$T_{0a,M}$	$y_{CO_2,B}$

In region I, the total loss (Figure 7.7(a)) shows that the same control structure can be used as in region II, namely, structure A, which is also the same as set RII1 (Table 7.4) for region II, keeping $U_{f,M}$ constant. Note that $U_{f,M}$ is not an active constraint in region I but the loss is small when keeping it constant. Note there are only 11 candidate sets (RI1-RI11) that are possible from grouping the candidate set (RII1) from region II with another variable because the others give infeasible solutions for some disturbances. Figure 7.7(a) also shows that the disturbances chosen here are equally important, even though some changes in some disturbances of region II greatly affect the total loss. Unfortunately, using the active constraint for the region I, y_{H_2,M_f}, as a member of the CV set gives infeasible solutions. The smallest losses in region III are obtained by controlling $T_{0a,M}$, $T_{f,M}/T_{0f,M}$, y_{H_2O,B_0} and y_{H_2,S_f} (set RIII1 in Figure 8 (c)). This corresponds to set RII1 from region II (Table 7.4) plus the active constraint in region III (Table 7.1) and $y_{H_2,S}$. In summary, the CV sets as shown in

Table 7.5 are recommended. Note that $U_{f,M}$ cannot be measured directly but it is a direct function of the current density and the fuel feed flow rate of MCFC, which means that $F_{CH_4,M_{0f}}$, $F_{CO,M_{0f}}$, $F_{H_2,M_{0f}}$ and j_M for control $U_{f,M}$ have to be known. The results so far showed that the system requires different control structures to cover the high disturbance ranges leading to advance control (Model predictive control; MPC) is required; however, the active constrain region also show the limitation of the disturbance ranges (±20% covering region I and II) that the PID can be implemented into the system.

Table 7.5 Recommended control structure (CV_1) in the three actively constrained regions

Structure	Region	CV₁		
		Active constraint	Set RII1 in region II (Table 7.4)	From Figure 7.7(a) & (c)
A	I & II	$T_{0f,S}$, $T_{0a,S}$, $y_{O_2,M_{0a}}$, y_{H_2,M_f}	$T_{0a,M}$, $T_{f,M}/T_{0f,M}$, y_{H_2O,B_0}	$U_{f,M}$ *
B	III	$T_{0f,S}$, $T_{0a,S}$, $y_{O_2,M_{0a}}$, $U_{f,M}$	$T_{0a,M}$, $T_{f,M}/T_{0f,M}$, y_{H_2O,B_0}	$y_{H_2,S}$

*active in region II

Step S4. Select location of TPM

The throughput manipulator (TPM) location is important because it links the top-down and bottom-up parts of the procedure. To minimize losses for large throughputs, the TPM should be located close to the process bottleneck (Rule 4 (Minasidis et al., 2015)). In our case, the bottleneck is the MCFC. Thus, the current density of the MCFC (V-19) is selected as the TPM.

Step S5 Structure of stabilizing control layer

The system should not drift too far from its acceptable operation. Hence, it is important to control all drifting variables to ensure the system running under safe and stable operation. In this case, temperatures are controlled to avoid material stress and stabilizing controlled variables already found in previous step. Fuel cell voltage is also important and should be controlled, however, it is related to hydrogen

concentration which is selected to be controlled from the step S3. When the hydrogen concentration and temperature are well controlled, voltage will be indirectly controlled too. In this case, the economic controlled variables are acceptable to be stabilizing controlled variables (CV2 = CV1), thus a separate regulatory control layer is not necessary. Furthermore, the measurements of open-loop right half plane (RHP) zeros and poles is mapped in this step as shown in Figure 7.8. They are independent of the controller and the control configuration and therefore reflect the controllability of the plant. Poles can tell whether the system is stable or not whereas zeros has an impact on the system's transient characteristics. However, the closed-loop poles can change to unstable if the open-loop zeros are lying in RHP because unstable zeros affect the achievable transient performances of feedback loops resulting in serious control problems. Figure 7.8 shows the open-loop poles and zeros of the dynamic system that all the zeros are in LHP. Small stable zeros with stable poles show that a very large amount of overshoot will be predicted. It can notice that there are some poles and zeros locate at the same spot indicating that lead-lag behavior may be found in the response. The unstable zeros and poles do not appear here and thus, the open-loop RHP zeros and poles may not affect the closed loop performance.
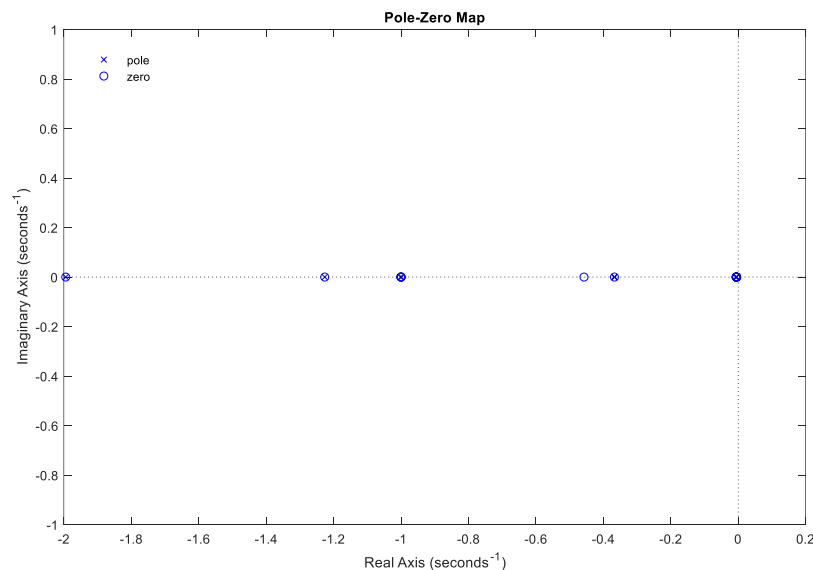
Figure 7.8 Pole and Zero map of the dynamic model of the integrated system.

Step 6. Select supervisory control layer.

In this step, controllers are implemented to keep controlled variables at their optimal setpoints. PID controller is a well-known controller in industry as it is simple, cheap, and feasible to be implemented. Decentralized control which may use simple PID controllers is the target of control strategy of this system. It is, however, preferred for non-interacting process. The relative gain array (RGA) is a controllability index for describing the interactions among inputs and outputs and is used for selecting the input-output pairings (see APPENDIX A.). In order to reduce the RGA size and difficulty in control design, Pair-close rule (Rule 9 (Minasidis et al., 2015)) revealed the manipulated variable should be close to the control variable is applied to reduce the time delay and loop interaction.

For the temperature controls, the pairings with manipulated variables (MV) are obvious. By-pass valves V-8, V-9, V-12 and V-13 are used to control $T_{0f,S}$, $T_{0a,S}$, $T_{f,M}/T_{0f,M}$, $T_{0a,M}$, respectively. However, the MCFC fuel utilization is less clear. It is influenced by how much fuel is used in the SOFC, which is a function of SOFC current density. The amount of consumed hydrogen depends on the rate of the electrochemical reaction (Equation (3.3)) and on the SOFC current density.Thus, 4 remaining CVs ($y_{O_2,M_{0a}}$, y_{H_2O,B_0}, $U_{f,M}$, y_{H_2,M_f}) will be considered to pair with MV by RGA. Considering pair-close rule around V-16 as an example, V-16 cannot be used to control y_{H_2,M_f} but it can be used to control y_{H_2O,B_0}. If V-16 is used to control y_{H_2O,B_0}, V-10 and V-6 will be used to control MCFC anode pressure and SOFC anode pressure, respectively. Hence, it is clearly seen that no MV to control y_{H_2,M_f} and that results in V-16 also cannot be used to control y_{H_2O,B_0}. V-15 is an only MV that can control y_{H_2O,B_0}. When pair-close rule is considered such as above example, the MVs sets that might control those CVs can be identified as shown in **Table 7.6** - **Table 7.9**. Firstly, paring with the negative RGA element is avoid causing instability with integral action in the loop. Next, aiming the RGA element which is closet to 1 in each control variable (no interaction from other loop). Thus, the bold RGA elements in each set indicate the pairing of that set. Set 1 (**Table 7.6**) and set 3 (**Table 7.8**) show the system provides large RGA elements indicating the system is fundamentally

difficult to control due to strong interactions. Set 4 (**Table 7.9**) contains RGA elements about 0.7 indicating the system has loop interactions. Set 2 (**Table 7.7**) provides the RGA elements close to 1, hence $F_{0a,S}$ (V-7) is used to control $y_{O_2,M_{0a}}$. j_S (V-18) is used to control y_{H_2,M_f}. $U_{f,M}$ is controlled by $F_{0f,M}$ (V-10) and $F_{0a,B}$ (V-15) is used to control y_{H_2O,B_0}.

Table 7.6 RGA of structure A: set 1

	$F_{0f,S}$ (V-6)	$F_{0a,S}$ (V-7)	j_S (V-18)	$F_{0a,B}$ (V-15)
$y_{O_2,M_{0a}}$	0.0077	**0.9960**	0.0002	-0.0040
y_{H_2O,B_0}	-0.0187	-0.0022	0.0164	**1.0045**
$U_{f,M}$	-4.3249	-0.0372	**5.3621**	0.0000
y_{H_2,M_f}	**5.3359**	0.0433	-4.3787	-0.0005

Table 7.7 RGA of structure A: set 2

	$F_{0a,S}$ (V-7)	j_S (V-18)	$F_{0f,M}$ (V-10)	$F_{0a,B}$ (V-15)
$y_{O_2,M_{0a}}$	**1.0030**	0.0013	-0.0002	-0.0041
y_{H_2O,B_0}	-0.0036	-0.0046	-0.0038	**1.0121**
$U_{f,M}$	0.0012	-0.0999	**1.0987**	0.0000
y_{H_2,M_f}	-0.0005	**1.1032**	-0.0947	-0.0079

Table 7.8 RGA of structure A: set 3

	$F_{0f,S}$ (V-6)	j_S (V-18)	$F_{0a,M}$ (V-11)	$F_{0a,B}$ (V-15)
$y_{O_2,M_{0a}}$	-0.1029	0.0112	**0.7574**	0.3343
y_{H_2O,B_0}	-0.0157	0.0140	0.2061	**0.7956**
$U_{f,M}$	-4.7440	**5.7440**	0.0000	0.0000
y_{H_2,M_f}	**5.8626**	-4.7693	0.0365	-0.1299

Table 7.9 RGA of structure A: set 4

	j_S (V-18)	$F_{0f,M}$ (V-10)	$F_{0a,M}$ (V-11)	$F_{0a,B}$ (V-15)
$y_{O_2,M_{0a}}$	-0.0026	0.0019	**0.6934**	0.3073
y_{H_2O,B_0}	-0.0032	-0.0029	0.3070	**0.6992**
$U_{f,M}$	-0.0957	**1.0957**	0.0000	0.0000
y_{H_2,M_f}	**1.1015**	-0.0946	-0.0004	-0.0065

จุฬาลงกรณ์มหาวิทยาลัย

CHULALONGKORN UNIVERSITY

Table 7.10 summarize MVs-CVs paring of the integrated system

MV	CV
By-pass valves (V-8)	$T_{0f,S}$
By-pass valves (V-9)	$T_{0a,S}$
By-pass valves (V-12)	$T_{f,M}\big/T_{0f,M}$
By-pass valves (V-13)	$T_{0a,M}$
$F_{0a,S}$ (V-7)	$y_{O_2,M_{0a}}$
$F_{0a,B}$ (V-15)	y_{H_2O,B_0}
$F_{0f,M}$ (V-10)	$U_{f,M}$
j_S (V-18)	y_{H_2,M_f}

จุฬาลงกรณ์มหาวิทยาลัย

CHULALONGKORN UNIVERSITY
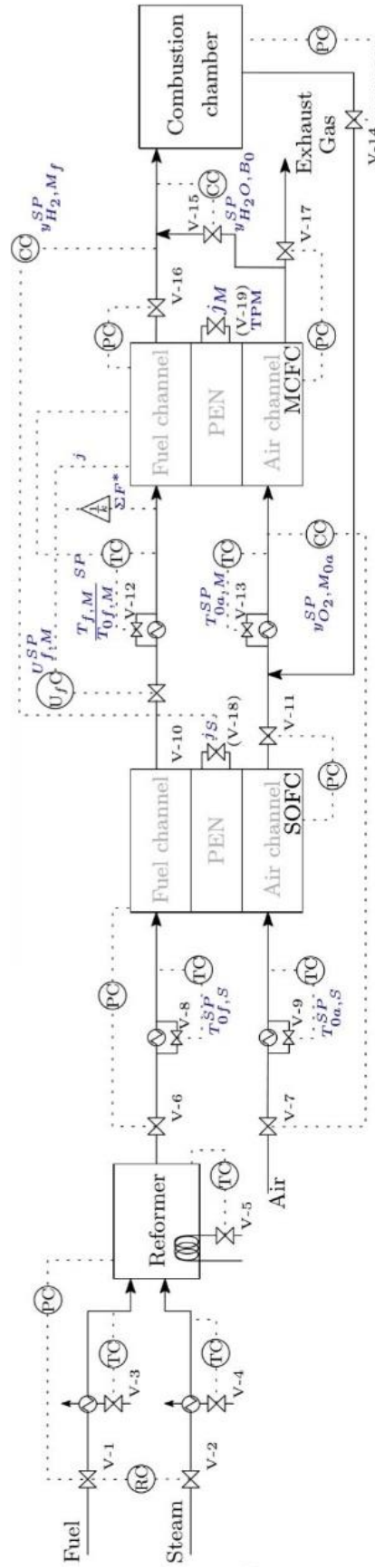
Figure 7.9 Control structure A for regions I and II

7.3   Closed-loop performance

From the Skogestad's control structure design method, the matching of MVs-CVs can be found as shown in Table 7.10. Temperatures are controlled by the by-pass valves which are very fast respond to the temperatures and thus temperatures in Table 7.10 are assumed to be well controlled and don't be considered here. Four proportional integral derivative (PID) controllers for controlling $y_{O_2,M_{0a}}$, y_{H_2O,B_0}, $U_{f,M}$ and y_{H_2,M_f} are implemented by SIMC tuning method because they are simple and easy to implement and work well on a wide range of processes (Skogestad, 2003) (see APPENDIX B.). The PID controller parameters for those controllers are showed in **Table 7.11**.

To evaluate the closed-loop performance, step setpoint changes and step input disturbances (the MCFC current density, methane feed flowrate and stream feed flowrate) are considered, and the integral absolute error (IAE) of the control error is used to evaluate the output control performance. IAE should be as small as possible.

$$\text{IAE} = \int_0^\infty |e(t)|\, dt \tag{7.5}$$

Table 7.11 The controller parameters for PID controllers

To control	K_c	τ_I	τ_D
$y_{O_2,M_{0a}}$	0.09	2.61	0.18
y_{H_2O,B_0}	-0.47	0.02	1.26
$U_{f,M}$	-0.11	2.31	0.17
y_{H_2,M_f}	-3.11E+05	3.91	1.52

7.3.1   Step setpoint changes

The closed-loop step response for set-point changes are performed in Figure 7.10 for CV signals and **Figure 7.11** is the MV signals responding to CV signals. Firstly, the simulation is performed under steady-state condition from the time of 0 s to 60 s (shown in area (0)). Secondly, set-point of $y_{O_2,M_{0a}}$ has been changed from 0.08

to 0.088 within the area (1). In the area (2), the set-point of $y_{O_2,M_{0a}}$ has been changed from 0.088 to 0.072. In conclusion, set-points of 4 CVs has been changed in both positive and negative direction from the normal set-points; area (1) and (2) for set-point of $y_{O_2,M_{0a}}$ changes, area (3) and (4) for set-point of y_{H_2O,B_0} changes, area (5) and (6) for set-point of $U_{f,M}$ changes, and area (7) and (8) for set-point of y_{H_2,M_f} changes. Notably, while one set-point has been changed, the others remains unchanged. All CVs can track the set-points well as shown as small IAE values. Even though the MV-CV pairing were selected at the RGA elements close to 1, the closed-loop response still shows that the system has loop interactions because when one set-point changed all controllers take the action to keep the CVs at their set-points. However, the result showed it was the right pairing and reasonable.

When $y_{O_2,M_{0a}}$ increases, the controller will decrease $F_{0a,S}$ (V-7), then oxygen that leaves the SOFC will be decreased and decreases in $y_{O_2,M_{0a}}$. The controller will increase $F_{0a,B}$ (V-15) in order to reduce y_{H_2O,B_0} when it is increased. For the MCFC fuel utilization $U_{f,M}$, the controller increases the MCFC fuel feed flow rate $F_{0f,M}$ (V-10) as $U_{f,M}$ increases. Increasing in fuel feed flow rate will reduce the fuel utilization when the reaction rate remains unchanged. The SOFC current density j_S (V-18) is decreased by the controller when hydrogen mole fraction of MCFC fuel channel outlet y_{H_2,M_f} decreases. Current density affects the fuel consumption of the fuel cell. When the SOFC current density decreases the SOFC anode-off gas will contain more fuel that feed to the MCFC anode that is akin to more fuel flow rate is fed to MCFC resulting in y_{H_2,M_f} increases.

7.3.2 Step input disturbances

When the system was perturbed by the disturbances, the system responded to the disturbances as shown in **Figure 7.12**-**Figure 7.13**. The MCFC current density j_M changed from 615.29 A/m² to 676.82 A/m² at the time 60 s to 360 s and then it

had changed to 553.76 A/m^2 till the time was 660 s, area (2). MCFC use more fuel to generate power as its current density increases resulting in a drop in oxygen at MCFC cathode inlet, a drop in hydrogen at MCFC anode outlet, hence the controllers have to increase the air feed flow rate $F_{0a,S}$ (V-7) and decrease the SOFC current density. As a result of increasing of fuel consumption the stream is more generated via reactions inside the MCFC resulting in increasing of stream mole fraction fed in burner y_{H_2O,B_0} and MCFC fuel utilization $U_{f,M}$. When y_{H_2O,B_0} increase, the controller will increase $F_{0a,B}$ (V-15) to get it back to the set-point. $F_{0f,M}$ (V-10) is increased by the controller to get more fuel feed in the MCFC to satisfy the fuel that is used more when the MCFC current density increases. Notably, all the controllers take actions at the same time.

Area (3) and (4) are the areas that methane feed flow rate disturbed the system by+10% of the normal value and by -10% of the normal value, respectively (normal value of methane feed is 0.0007 mol/s). When the fuel feed increases with the stream feed is unchanged, oxygen and stream in the MCFC exit gas drop (affect to burner feed) as they are used to generate hydrogen, the controller increases the air feed $F_{0a,S}$ (V-7) to fulfill the oxygen and the controller also decreases the oxygen source of the burner $F_{0a,B}$ (V-15) as it dilutes the stream concentration at the burner feed y_{H_2O,B_0}. When the fuel feed increases, more unused hydrogen leaves the fuel cell. The controller has to adjust the SOFC current density in order for the fuel will be more used in the SOFC. Consequently, fuel utilization $U_{f,M}$, it is suddenly increased, then the controller must increase the $F_{0f,M}$ (V-10).

For the stream feed flow rate disturbed the system by+10% and -10% of normal value in area (5) and (6), respectively (normal value of stream feed is 0.0014 mol/s). the +10% step change of stream feed flow rate has no significant impact on the CVs. However, negative step change of stream feed flow rate affects the CVs. Decreasing of stream feed flow rate is akin to system with increasing of methane feed flow rate.
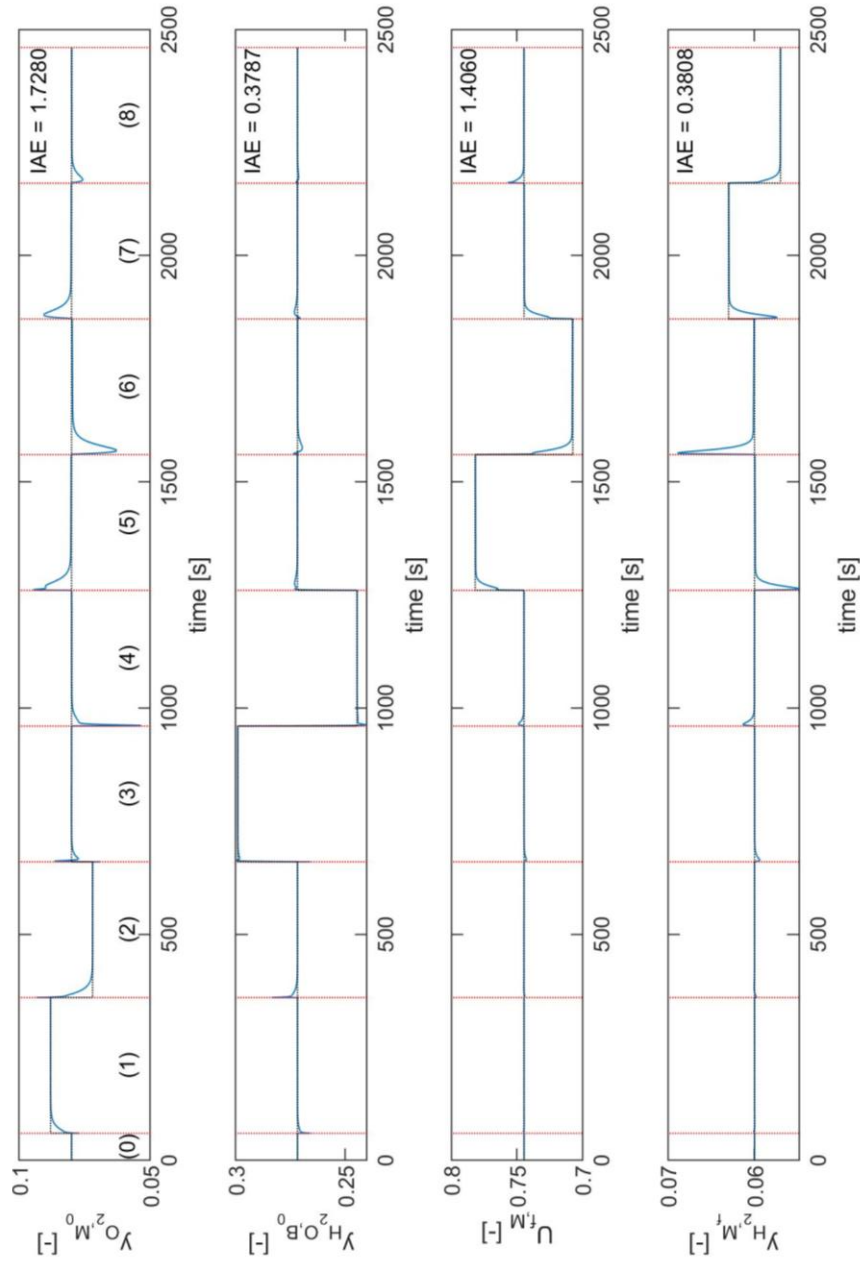
Figure 7.10 The CV signals of closed-loop step response for set-point changes; steady-state in (0), $y_{O_2,M_{0a}}^{SP}$ changed to 0.088 in (1), $y_{O_2,M_{0a}}^{SP}$ changed to 0.072 in (2), y_{H_2O,B_0}^{SP} changed to 0.299 in (3), y_{H_2O,B_0}^{SP} changed to 0.2447 in (4), $U_{f,M}^{SP}$ changed to 0.7819 in (5), $U_{f,M}^{SP}$ changed to 0.7074 in (6), y_{H_2,M_f}^{SP} changed to 0.063 in (7), and y_{H_2,M_f}^{SP} changed to 0.057 in (8)
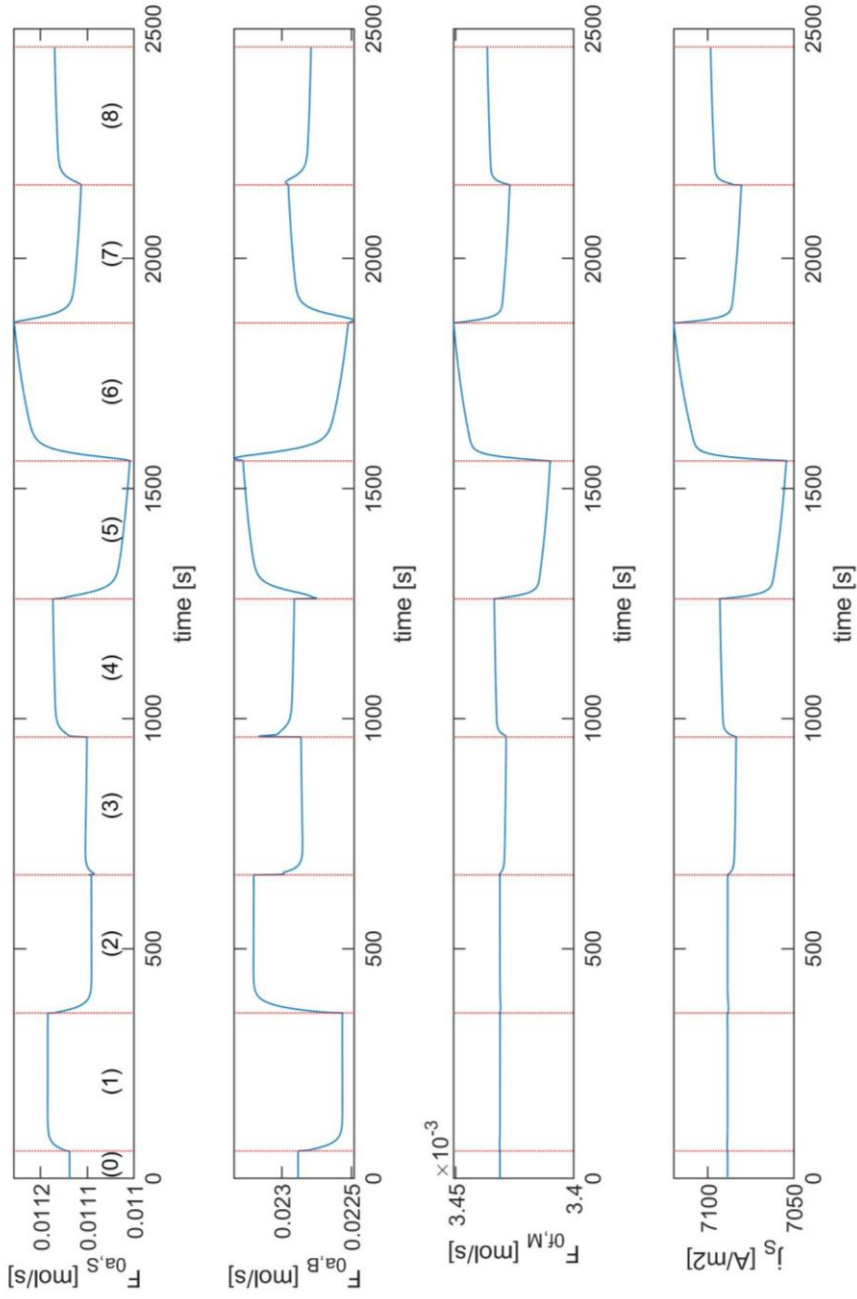
Figure 7.11 The MV signals of closed-loop step response for set-point changes; steady-state in (0), $y^{SP}_{O_2,M_{0a}}$ changed to 0.088 in (1), $y^{SP}_{O_2,M_{0a}}$ changed to 0.072 in (2), $y^{SP}_{H_2O,B_0}$ changed to 0.299 in (3), $y^{SP}_{H_2O,B_0}$ changed to 0.2447 in (4), $U^{SP}_{f,M}$ changed to 0.7819 in (5), $U^{SP}_{f,M}$ changed to 0.7074 in (6), $y^{SP}_{H_2,M_f}$ changed to 0.063 in (7), and $y^{SP}_{H_2,M_f}$ changed to 0.057 in (8)

132
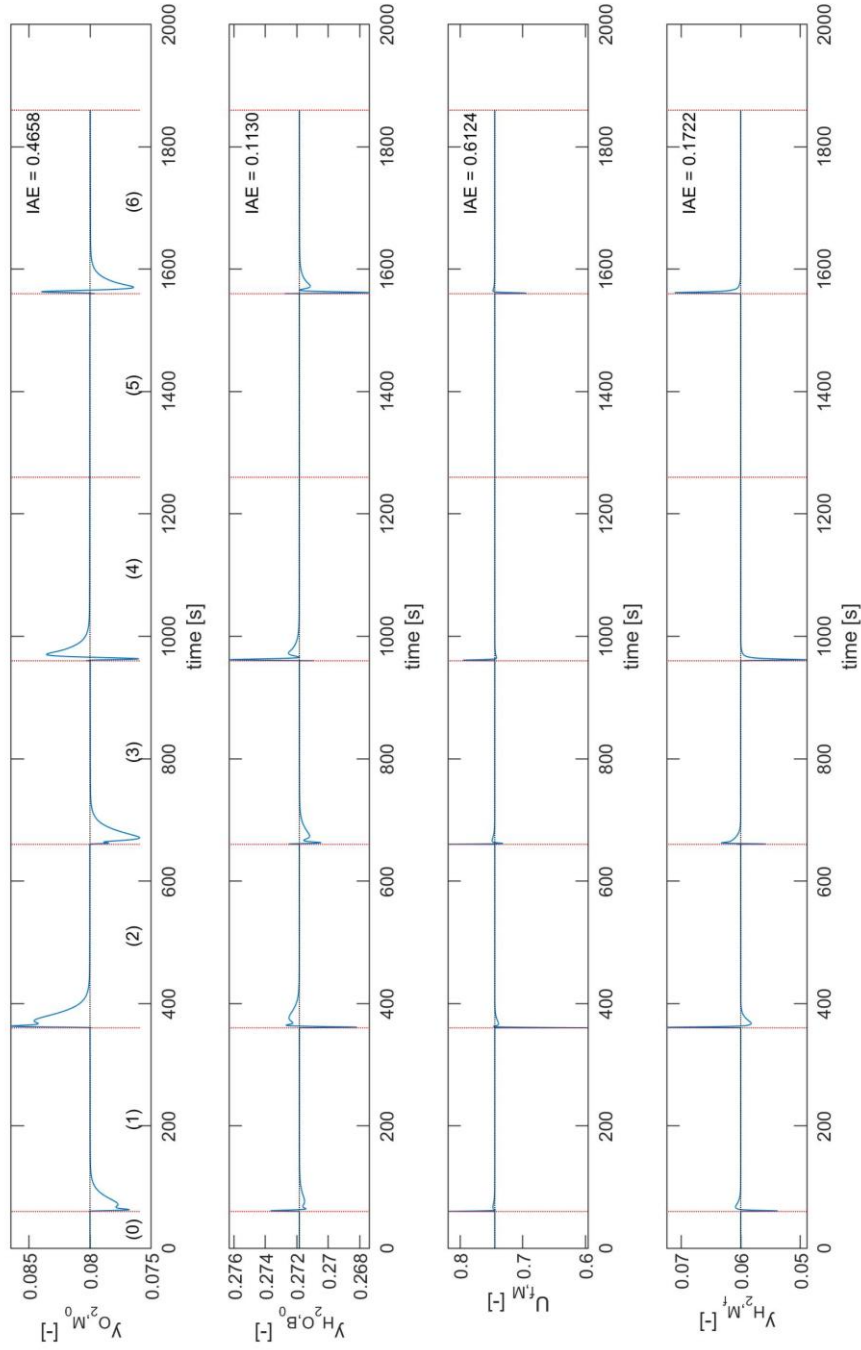
Figure 7.12 The CV signals of closed-loop step response for disturbance rejection; steady-state in (0), +10% of j_M change in (1), -10% of j_M change in (2), +10% of F_{0,CH_4} change in (3), -10% of F_{0,CH_4} change in (4), +10% of F_{0,H_2O} change in (5), and -10% of F_{0,H_2O} change in (6)
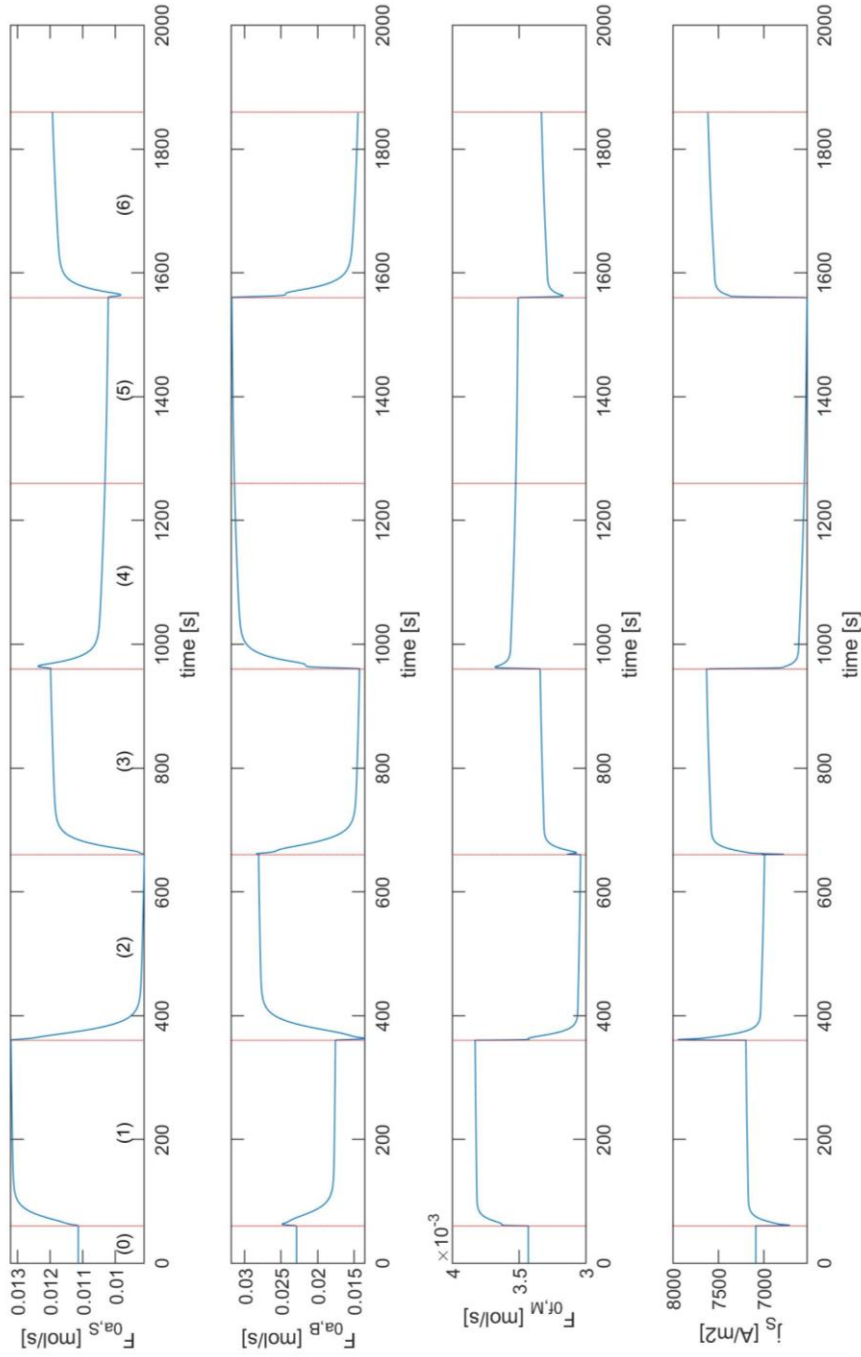
Figure 7.13 The MV signals of closed-loop step response for disturbance rejection; steady-state in (0), +10% of j_M change in (1), -10% of j_M change in (2), +10% of F_{0,CH_4} change in (3), -10% of F_{0,CH_4} change in (4), +10% of F_{0,H_2O} change in (5), and -10% of F_{0,H_2O} change in (6)
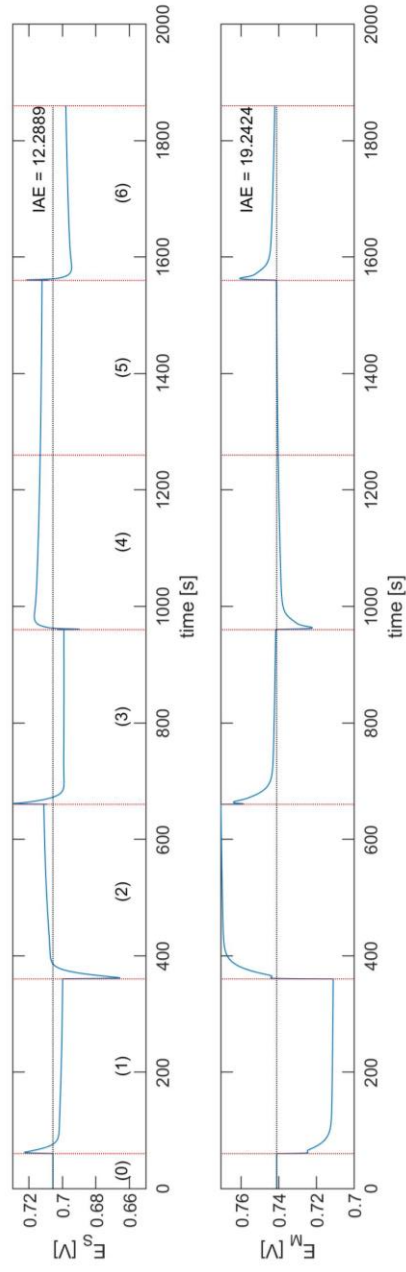
Figure 7.14 The interested output of closed-loop step response for disturbance rejection; steady-state in (0), +10% of j_M change in (1), -10% of j_M change in (2), +10% of F_{0,CH_4} change in (3), -10% of F_{0,CH_4} change in (4), +10% of F_{0,H_2O} change in (5), and -10% of F_{0,H_2O} change in (6)

Recall our assumption in step S5 *"When the hydrogen concentration and temperature are well controlled, voltage will be indirectly controlled too"*, it's not always true as seen in **Figure 7.14**. it can notice that it clearly depends on the considered disturbance.

It is noted that the recommended CVs in this study are slightly different from the proposed control system by others (Huang et al., 2011), in which the air flow rate was used to control either temperature or fuel utilization. Based on our study, it is suggested to use the air flow rate to control the MCFC oxygen feed concentration instead. In addition, the H_2 composition needs to be controlled in the proposed control structure, which is similar to that of Chatrattanawet et al. (2015) in that the H_2 composition outlet of a fuel cell system is controlled to achieve high power generation. In addition, fuel cell feed temperatures are normally considered disturbances for a fuel cell; however, they are considered to be controlled in our case instead. Based on the self-optimizing control variable, it is found that among those candidates, voltages have lost to minimize the loss, but rather an H_2 composition outlet is recommended to be controlled. As described in step S2, the proposed control structures are based on an actively constrained region resulting from the presence of disturbances. Thus, some controlled variables might be changed.

7.4   Conclusions

In this work, a control structure based on Skogestad's procedure was designed for the SOFC-MCFC integrated system. The aim of this control structure was to achieve close-to-optimal power generation while reducing carbon dioxide emission and achieving safe operation. Three actively constrained regions were found by varying two feed disturbances. The nominal operating point was in the region I where $T_{0f,S}$, $T_{0a,S}$, $y_{O_2,M_{0a}}$ and y_{H_2,M_f} were active constraints. The self-optimizing method was used to select the best CVs for the remaining unconstrained degree of freedom. Region II has fewer unconstrained DOFs, and thus, it was used as the base for the control structure of other regions. The fuel utilization $U_{f,M}$ was one of the CVs because it

was active in region II and III. However, it could not be measured so, $F_{\text{CH}_4,M_{0f}}$, $F_{\text{CO},M_{0f}}$, $F_{\text{H}_2,M_{0f}}$ and j_M are measured for control of $U_{f,M}$. The MCFC was found to be the bottleneck of this system. Thus, j_M was selected as the TPM of the system. An evaluation of the losses with various disturbances showed that regions I and II could use the same control structure. In addition, active constrain region also indicates the limitation ($\pm20\%$) in the disturbance changes when PID controllers are implemented. However, the purposed control structure can't control fuel cell voltages which are also important. The recommendation for correcting this issue either using cascade control (repeat the step S5; select voltages as additional CV2 and MV of supervisory control layer as their set-points) or using MPC. MPC implementation can gain an additional benefit, enable control structure change.

CHAPTER 8

Design of a hybrid SOFC-MCFC-GT system with compressed air energy storage

This chapter presents the implementing of a gas turbine in the SOFC-MCFC fuel cell integrated system. The advanced adiabatic compressed air energy storage (AA-CAES) system is designed to enhance the system flexibility. The investigation is performed by using steady-state model of mass, energy and electrochemical model. Simulations of the proposed power system are performed to demonstrate the amount of power it can supply to the loads during normal and peak modes of operation. This chapter is in progress of the reviewing.

8.1   Introduction

The need for electrical power is currently on the rise (Klein, 2016). As power plants are the largest source of carbon dioxide (CO_2) emissions, the use of renewable energy and alternative clean power generation technology is attracting increasing attention in many countries. Solid oxide (SOFCs) and molten carbonate (MCFCs) fuel cells as high-temperature fuel cells have been considered as alternative reliable power generators exhibiting high electrical efficiency and low environmental impact.

A stand-alone SOFC is normally operated at moderate fuel utilization to avoid nickel oxide (NiO) formation at the anode, a process that leads to long-term cell degradation (Nehter, 2007; Parhizkar and Roshandel, 2017). Therefore, SOFCs should be integrated with other systems so that the fuel remaining in the anode as off-gas can also be utilized. The exhaust gas from SOFCs can be directly used in MCFCs without any additional purification (McPhail et al., 2011). Furthermore, CO_2 in the SOFC anode off-gas is used to react with oxygen to promote carbonate ion (CO_3^{2-}) formation and carry electrons. Hence, a system integrated with an MCFC can utilize CO_2 and generate more power (Wee, 2014). When the MCFC is integrated in series with an SOFC, most of the power is generated by the SOFC, while the MCFC generates additional power by using the remaining fuel from the SOFC and the carbon dioxide from the afterburner. CO is also more converted to H_2 inside the MCFC.

Thus, an SOFC and MCFC integrated system is a promising system that can increase fuel and carbon dioxide utilization as well as power generation (Jienkulsawad and Arpornwichanop, 2016; Jienkulsawad et al., 2018).

In general, power requirement depends on the load, which varies with the electricity demand. However, fuel cells can be operated safely in a steady-state mode and thus, energy storage should be integrated within the fuel cell system for use in load-following applications (Nease et al., 2016). In our previous studies on the SOFC and MCFC integrated system (Jienkulsawad et al., 2017), the exhaust gas from the MCFC still contained a small amount of fuel. This was burned in an afterburner to recover the useful energy and increase the CO_2 concentration before it was recycled to the MCFC cathode. Alternatively, the afterburner can be replaced with the combustion chamber of a gas turbine (GT) to generate more electrical energy, which is captured by energy storage for later use. This approach maintains constant power generation from the integrated fuel cell system during operation.

Among the different types of energy storage technology, the compressed air energy storage (CAES) system shows great potential for applying to GT technology. This system provides many benefits such as large power and energy capacities, a long life cycle, and a fast response time (Guney and Tepe, 2017; Nease and Adams Ii, 2014). In addition, CAES is the cheapest energy storage system available to date (Sheng et al., 2017). Recently, CAES technology has been optimized to an "advanced adiabatic compressed air energy storage (AA-CAES)" system, which eliminates the need for fuels during the discharging phase (Mozayeni et al., 2017). Thermal energy storage (TES) technology is adopted to extract heat from the compressed air during the charging phase and to release this heat to the compressed air during the discharging phase. Hence, in an AA-CAES system, the use of fossil fuels to heat up the compressed air is avoided. The concept of using carbon dioxide, instead of air, as a working fluid in energy storage systems (ESSs) has been proposed (Wang et al., 2015). Based on the thermodynamic analysis by Zhang et al. (2016), a comparison of the AA-CAES, compressed CO_2 energy storage (CCES), and liquid CO_2 systems revealed that the AA-CAES system provided the highest system efficiency. However, the energy density of the CCES system was ~2.8-fold higher than that of the AA-CAES system that affects the volume requirement to store the energy. Although air

requires more space than CO_2, the AA-CAES system seems to be more suitable for application to an SOFC and MCFC integrated system because air is used in both the fuel cell systems and in the combustion process. Moreover, the extraction of CO_2 from the N_2-containing exhaust gas becomes difficult and requires additional units and energy. In addition, the heated air from the AA-CAES system can be used in the integrated fuel cell system to reduce the heat duty of the preheater unit.

In this study, the integrated fuel cell system is modified by replacing the afterburner with the GT combustion chamber, and the power generated by the GT is captured using an AA-CAES system for future power supply. The system is investigated to elucidate the amount of energy that can be further generated by using only the remaining fuel from the system to supply the load during high power demand. Additional GT and AA-CAES air feed and pressure ratios are the key parameters for designing this system.

8.2   Description of the hybrid system

As mentioned in the introduction section, the afterburner of the SOFC-MCFC integrated system is replaced by the GT combustion chamber to increase electrical generation (hybrid system). However, a hybrid system without additional air feed (**Figure 8.1**(a)) is inept because the MCFC cathode off-gas, with low O_2 content, would be used for the complete combustion process in the GT combustion chamber. Thus, the energy required for the GT compression process would be higher than the power generated from its expansion process. Besides reducing the energy usage in the GT compression process by condensing out the H_2O, air is free, with less energy requirement during the compression process. Hence, the MCFC anode off-gas and part of the cathode off-gas are mixed and the remaining H_2 and CO gases are burned with the additional fed air in a combustion chamber to form CO_2 before being recirculated back to the MCFC cathode. This increases the energy for power generation via the GT (**Figure 8.1**(b)). However, it must remark that the energy that used to pre-heat the air (heat exchanger no.4) in the previous design (without a GT) is used to drive the turbine of GT, instead. Hence, the system might require the heat from the outsource to pre-heat the air. Note that the injector power consumption for injecting fuel to the combustion chamber is not considered in this study. The GT

power generation is, therefore, slightly overestimated. The proposed system design is based on the use of power generated from the integrated fuel cell system as a based load. The system can therefore be described by two phases, namely the charging and discharging phases.

Figure 8.1 Hybrid system without (a) and with (b) additional air feed.
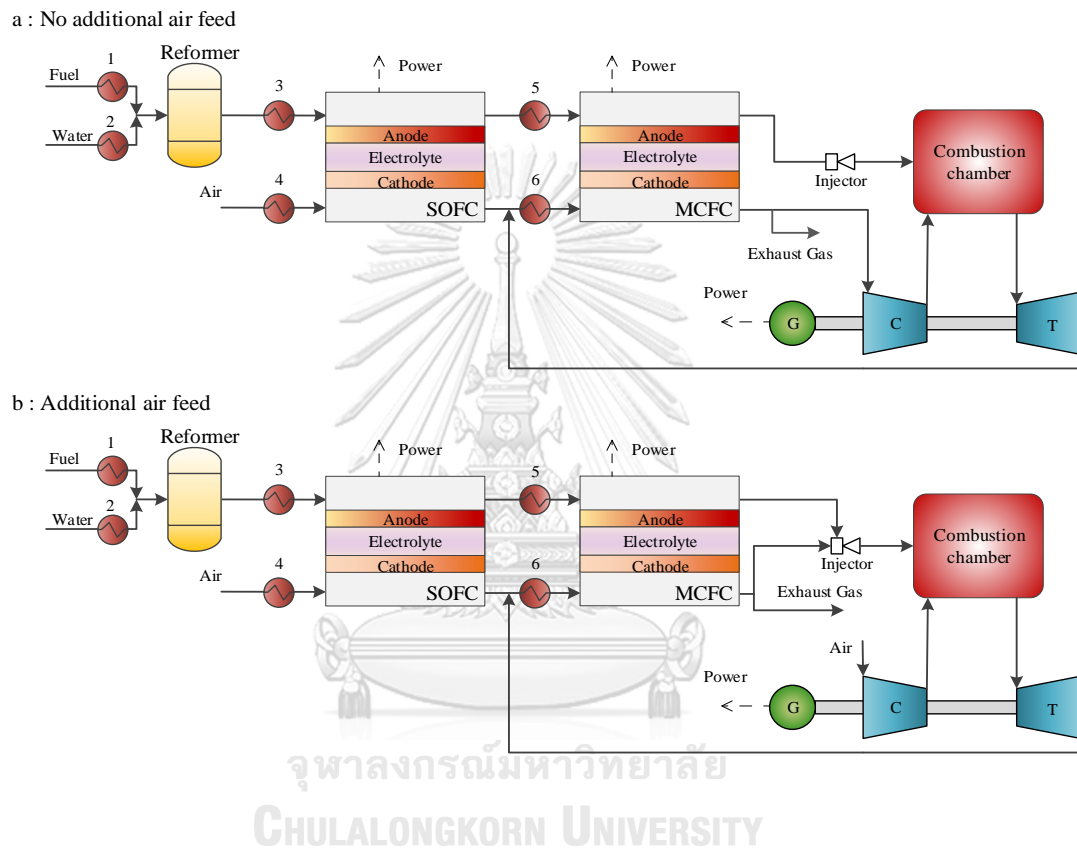
The charging phase (**Figure 8.2**(a)) occurs when the power requirement from the loads is in low demand. In the worst-case scenario, all generated power from the GT will be used to drive the air compressor to compress air to the storage. The compressed air will pass through a heat exchanger to extract the heat to the thermal energy storage (TES). In this way, no additional fuel is required to heat the compressed air from storage before it expands in the turbine during the discharging phase.

The discharging phase (**Figure 8.2**(b)) occurs when the power requirement from the loads is higher than the based load power. The generated power from the GT will no longer be used to drive the air compressor but as additional power generation. The compressed air from the storage exchanges the heat from the TES and is expanded in the turbine for further power generation. This air is fed to the SOFC cathode, instead of fresh air, to reduce the heat duty in the heat exchanger at the SOFC cathode feed.

In conclusion, there are three power generator sources: an integrated fuel cell system, GT, and AA-CAES. The integrated fuel cell system is a power generator that only supplies power to the load when the power is in low demand.
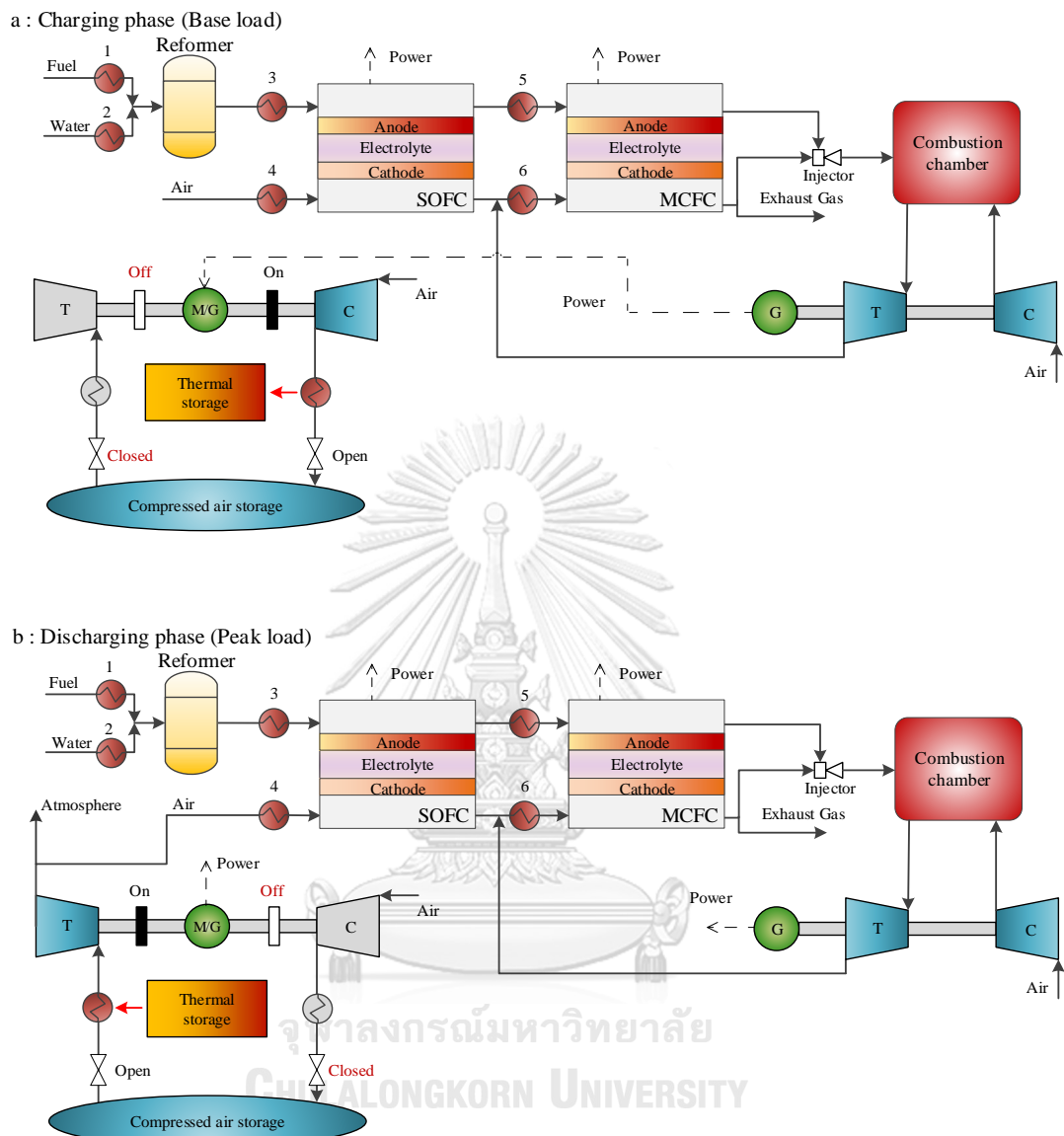
Figure 8.2 Charging (a) and discharging (b) phases of the hybrid system during normal and peak modes of operation, respectively.

8.3   Results and discussion

Simulations of the proposed fuel cell hybrid system are performed to illustrate how much electrical energy can be further generated by the exhaust gas of the fuel cell system (**Figure 8.1**(b)). The integrated fuel cell system is designed to operate at 1 atm as in the previous design (Jienkulsawad et al., 2017). The additional air fed to the system and the pressure ratios of the GT and compressor in the CAES are the key parameters for performance improvement during peak and normal loads. In this study, a single cell (SOFC and MCFC) is used as a base to design a hybrid system that can stack cells to generate the required design power. Therefore, the power ratio is used to illustrate the amount power the system can generate.

8.3.1   Effect of the added air and GT pressure ratios (performance improvement by integrating with a GT)

In the hybrid system, additional air is compressed to the combustion chamber to burn the exhaust gas from the integrated fuel cell system. The ratio of additional air to fuel fed to the system defined as added air ratio is used to illustrate the amount of air. Thus, the CO_2 concentration is lower in the recycle stream and MCFC cathode, resulting in a decrease in power generation by the fuel cell in the hybrid system (**Figure 8.3**(a)). It is considered as a loss in power generation of fuel cell due to implemented with GT when the power is compared with the power of the fuel cell system without a GT. However, power generation from the GT is higher than the loss from fuel cell power generation in the hybrid system (**Figure 8.3**) and thus, the low fuel content in the MCFC exhaust gas can still be further used in the GT. Higher GT pressure ratios improve the power generation of the hybrid system as more GT power

is generated (**Figure 8.3**(b) and (c)). However, the generated power from the fuel cell in the hybrid system (**Figure 8.3**(a)) is dramatically lower than the optimal power generation of a conventional integrated fuel cell system (dotted grey line in **Figure 8.3**(a)).

Because the fuel is limited and set, an increase in the GT pressure ratio does not significantly affect the combustion chamber temperature, as illustrated in the turbine inlet temperature of the GT (**Figure 8.4**(a)). Thus, the outlet temperature of the turbine decreases significantly with an increase in the GT pressure ratio during the expansion process. This results in a lower mixing temperature at the MCFC cathode feed (constant MCFC cathode feed temperature is assumed (well-controlled); **Figure 8.4**(b)). Temperature of mixing streams that is higher than MCFC cathode feed temperature indicating the heat is extracted via exchanger no. 6, blue lines. Whereas the red lines are indicated the heat is needed to warm up the gas to the MCFC cathode temperature. Additional air feed to the hybrid system via GT increases the power generation from the hybrid system as a result of very small loss in the MCFC when implemented with the GT. The CO_2 concentration in the MCFC cathode is therefore further diluted by the increase of additional air, resulting in an increase in the MCFC cathode resistance (electricity loss). **Figure 8.3** demonstrates that an increase in the added air ratio enhances power generation; however, the power generated from the GT in the hybrid system is compared to the loss in MCFC power generation in the new design (**Figure 8.5**). This loss is the difference in MCFC power generation between the previous integrated system and the proposed hybrid system. The power ratio in **Figure 8.5** indicates by how much the GT power generation exceeds the loss in MCFC power generation in the new design. The proposed integrated design is not feasible when the power ratio = 1. Notably, the additional air feed should be very small to minimize the loss in MCFC power generations and gain high power ratio. When the heat exchanger no. 6 is designed to cool down the gas as being in the previous design, the GT pressure ratio about 6 is recommended to obtain high power generation. In addition, it can be operated in the range of micro gas turbine (MGT) pressure ratio operation.
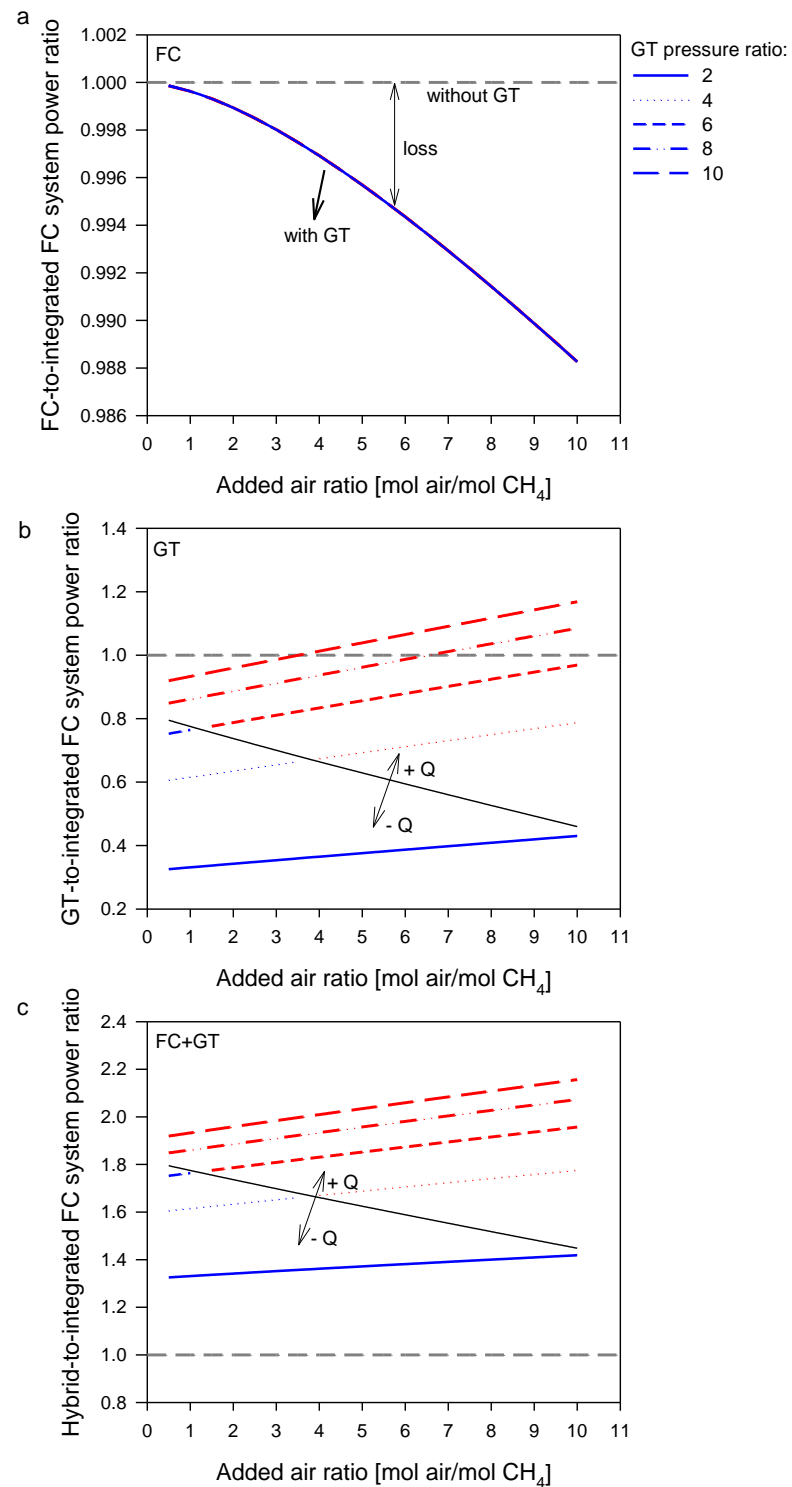
Figure 8.3 Effect of the added air feed and gas turbine (GT) pressure ratio on the ratio of the generated power of the fuel cell system (a), GT (b), and hybrid system (c) to the generated power of the integrated fuel cell (FC) system from a previous design (Jienkulsawad et al., 2017)
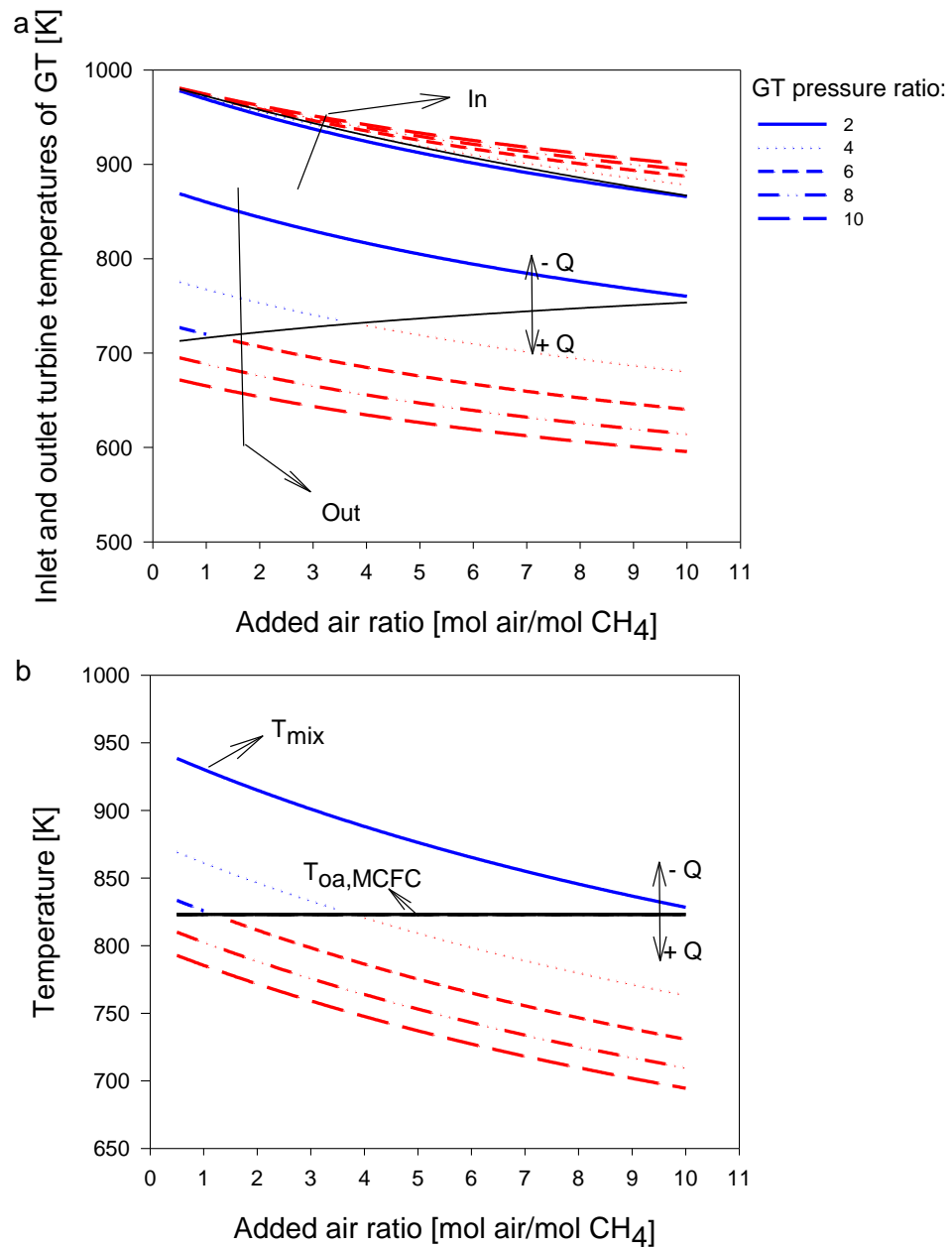
Figure 8.4 Effect of additional air feed and gas turbine (GT) inlet and outlets (a), mixing, and MCFC cathode feed (b) temperatures
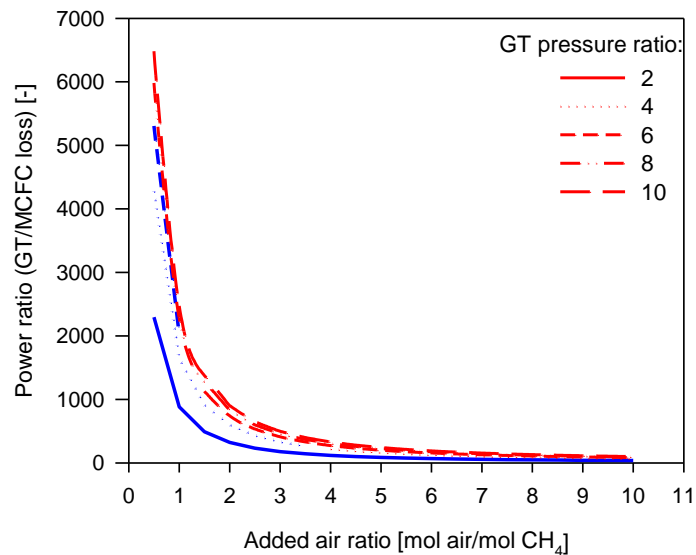
Figure 8.5 Effect of the gas turbine (GT) pressure ratio on the GT generated power-to-loss in MCFC power generation ratio due to GT integration.

8.3.2 Effect of the compressor pressure ratio (charging phase to discharging phase)

In the worst-case scenario of the hybrid system, all the power generated from the GT is designed to drive the air compressor during a low electricity demand and store the energy for use during a high electricity demand. From the charging phase to the discharging phase, the electrical energy produced from the GT is transformed into mechanical energy and converted back to electrical energy. **Figure 8.6**(a) illustrates that significant energy loss occurs in the AA-CAES due to this conversion of energy. Thus, the power generated by the turbine in the AA-CAES system is much lower than the power generated by the GT. However, this loss can be lowered by increasing the compressor pressure ratio. Notably, the loss is not directly reduced by an increase in the compressor pressure ratio. However, the CAES generates more power with higher pressure ratios at a certain power input (fixed GT power).

The storage volumes (**Figure 8.6**(b)) drop rapidly as the compressor pressure ratio increases. The volumes become smaller, as the air requirement reduces (**Figure 8.6**(c)). **Figure 8.6**(c) also illustrates that the air fed to the storage is higher than that fed to the FC system, except for the significantly high-pressure AA-CAES ratio,

indicating that the air storage is never empty at low pressure ratio. The TES volume is bigger than the CAES volume. A way to reduce the volume requirement of the TES is to change the exchange medium to a higher heat capacity medium. Since the compressed air cools down to room temperature (298 K) in the TES and the TES temperature is assumed to be constant, the air from the storage is heated by the TES as show as the inlet temperature of the turbine (red solid line in **Figure 8.7**(a)). The outlet temperatures of the compressor and turbine (dotted line in **Figure 8.7**(a)) therefore increase and decrease because of the compression and expansion processes, respectively.

During the charging phase, the air fed to the SOFC is heated from 373 K to 1073 K (black lines in **Figure 8.7**(b)). The air exiting the turbine is used to feed the SOFC during the peak load. As illustrated in **Figure 8.7**(b), the air temperature that exits the turbine of the AA-CAES system is > 373 K. This implies that the heat duty of exchanger 4 can be reduced to heat the air to the desired temperature (1073 K). An increase in the AA-CAES pressure ratio results in a lower exit temperature of the turbine and a higher temperature gradient in the exchanger. As previously mentioned (Section 8.2), the air from the AA-CAES is fed to the SOFC and thus, the power generated from the AA-CAES presented herein is in good agreement with the air flow rate required in the FC system. Hence, if the electricity demand is significantly high, the air flow rate of the turbine can be raised to satisfy the demand. However, some of the air must be released to the atmosphere to maintain the amount of air required by the FC system and prevent a performance drop in the FC system.

As mentioned in the system description section (Section 8.2), the generated power from the FC system is the only energy supply during low demand because the generated power from the GT charges the air to the storage (worst-case scenario design). Hence, the power generation in the based load refers to the FC system. The energy stored in the AA-CAES will supply the load when the demand is high; therefore, the power generated from the FC, GT, and CAES are supplied to the loads during peak demand. Figure 8(c) reveals that the power generation (FC, GT, and CAES) at the peak load with a given specific GT operation (added air ratio = 0.5 and GT pressure ratio = 6) grows with an increase in the CAES compressor pressure ratio. The storage volumes (**Figure 8.6**(b)) also suggest that CAES pressure ratios ≥ 8 are

necessary to achieve the required small volume. A comparison of the air flow entering and exiting the AA-CAES, reveals that the CAES pressure ratio should not be too high to spare some air in the storage. When the power demand is extremely high, the spare air can be released to the atmosphere to increase the power, with constant air fed to the hybrid system. Hence, we recommend the CAES pressure ratio range 8–15. At an added air ratio of 0.5, GT pressure ratio of 6, and CAES pressure ratio of 15, the power generation of the hybrid system during the peak load is 2.18 times higher than that of the based load when the air flow rate released from the AA-CAES is the total FC system air feed.

It is usually designed to handle different power demands of ≤ 50 % of the based load at normal power operation mode. Based on our design, whereby the FC power is designed as the based load in the worst-case scenario, significant power can be generated during the peak load compared to that observed at the based load. Therefore, power from the FC system and partial power from the GT can be supplied during low demand to reduce the size of the FC system. When a portion of the power from the GT is supplied to the load and less power is stored, the power can increase to 1.75 times of the based load (Maximum power supply to the load during charging phase; dotted line in **Figure 8.7**(c)). However, the power produced by AA-CAES is lower too.
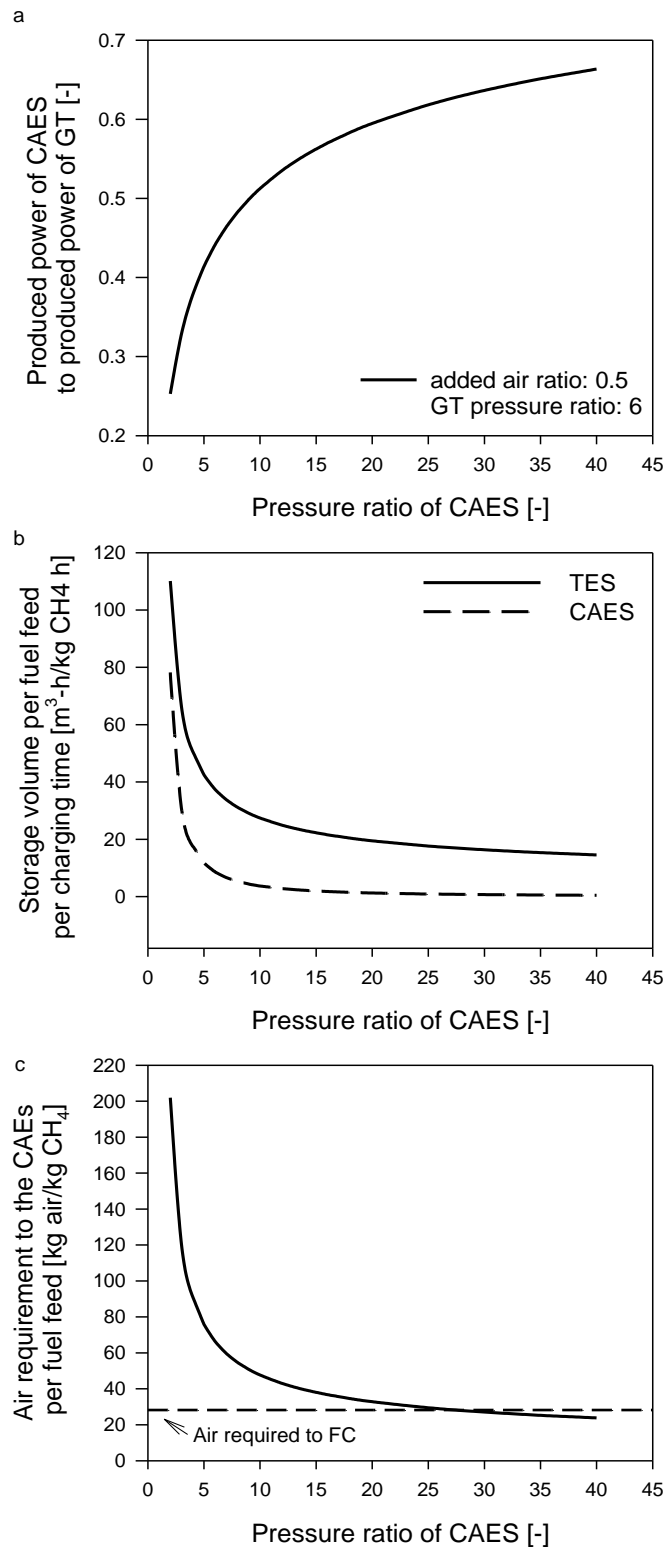
Figure 8.6 Effect of the compressor pressure ratio on the turbine-to-gas turbine (GT) generated power ratio (a), air and energy storage volume (b), and storage air requirement (c).
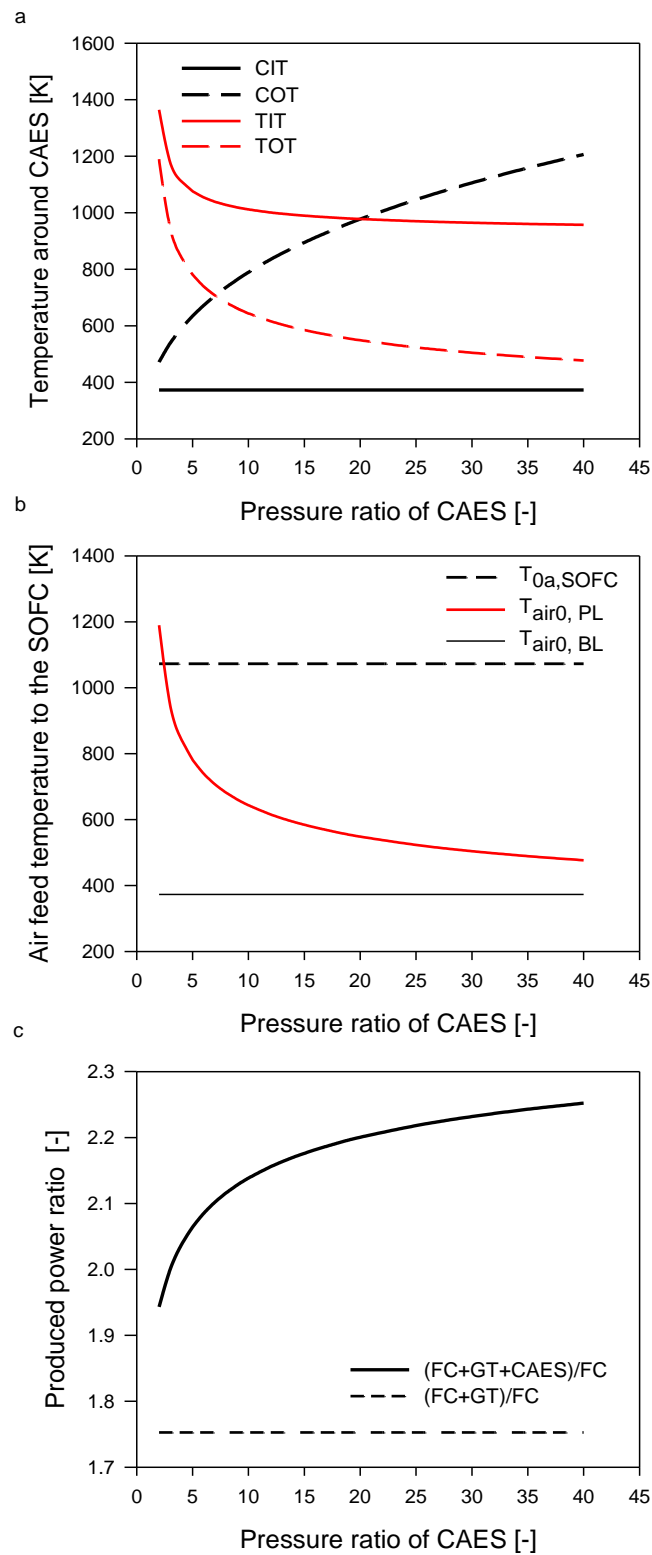
Figure 8.7 Effect of the compressor pressure ratio on the temperature around the compressed air energy storage (CAES; a), air feed temperature to the solid oxide fuel cell (SOFC; b), and peak-to-based load ratio (c).

8.4   Conclusions

During practical operation, power generation varies with different loads. The integrated fuel cell system is a potential high-performance power generation system; however, its power generation should not vary with a change in load. This study proposed the possibility of implementing a GT and AA-CAES into an integrated fuel cell system. In the proposed system, the GT power is stored in the AA-CAES (energy storage) to cope with the variation in power demand. The simulation results indicated that the remaining fuel from the fuel cell system is valuable and can be further used in the GT. Moreover, the proposed system can effectively handle the power variation. The ratios of the added air and GT and AA-CAES pressures are the key parameters to design this hybrid system. This study revealed that the addition of a GT to the integrated fuel cell system also slightly reduces the power generation of the fuel cell system. This was attributed to the additional air fed to the hybrid system to dilute the carbon dioxide in the MCFC cathode; however, the power from the GT can compensate for this loss. The results also illustrated that the added air ratio must be very small to reduce the loss in the power generation of the MCFC and contain high power generation ratio. The power generation of the hybrid system increases with an increase in GT pressure. However, the GT pressure ratio of 6 is recommended when the same action of heat exchanger no. 6 (extract the heat) is preferred. The AA-CAES pressure ratio range 8–15 is recommended because the storage volume of the AA-CAES can be minimized at pressure ratios of 8 and 15. This guarantees that some air remains in the storage, which can be released to the atmosphere via the turbine to supply the power during very high demands. Please keep in mind that the remaining energy that used to pre-heat the air in the integrated fuel cell without a GT is used to drive the turbine of GT, instead. Hence, the system might require the outsource heat to pre-heat the air. In addition, more detail on the physical limitations of the system must be considered before it can be used in a practical power plant.

CHAPTER 9
CONCLUSIONS

9.1 Conclusions

This research proposes the potential option to handle the exhaust gas from a solid oxide fuel cell (SOFC) with a molten carbonate fuel cell (MCFC). The simulation study was performed in Matlab to investigate the system performance and to study the control structure design. Steady-state conditions is performed to study parameters and system configurations that can possibly improve the overall performance (CHAPTER 5, CHAPTER 6 and CHAPTER 8). Only the control structure design study (CHAPTER 7) was running in the dynamic condition. To illustrate that the proposed system provides a better performance, the system was fed with the same amount of fuel, steam and air flow rate.

9.1.1 Effect of operating parameters to the system performance

The performance of the SOFC and MCFC integrated system was studied and compared to a single system (SOFC or MCFC) for each operating condition; temperature, fuel utilization, degree of pre-reforming and CO_2 feed. For the single system, reformed gas from the pre-reformer was used as a fuel for the SOFC or the MCFC. For the integrated system, reformed gas from the pre-reformer was fed to the SOFC, and the exhaust gas from the SOFC was directly fed into the MCFC. The remaining gas from the fuel cell is mixed and burned in an afterburner in all of the systems and used in preheating units. The results showed that fuel utilization of both fuel cells, temperature of the SOFC and reformer dramatically affect the performance of the integrated system. Whereas a change in the degree of reforming, temperature of the MCFC and CO_2 feed ratio insignificantly affect the performance of the integrated system. It is also shown that the integrated system provides a higher electrical efficiency than the single SOFC or the single MCFC; however, the thermal efficiency of both of the single fuel cells is better than that of the integrated system. At the selected operating conditions (10% degree of reforming, 973 K reformer temperature,

1073 K SOFC temperature, 973 K MCFC temperature, 70% SOFC fuel utilization, 90% MCFC fuel utilization and fully recycled), the electrical efficiency of the integrated system is 55.22%.

9.1.2 Effect of system configuration on the performance

As the configuration of the SOFC-MCFC integrated system is important and affects the system performance. Four configurations; (A) an adding the MCFC on existing an SOFC, (B) a series, (C) a parallel and (D) a series-parallel combination configuration, were proposed to be investigated and compared the performance of the integrated systems in terms of power generation, CO_2 utilization, heat duty and NiO formation possibility. To investigate the effect of different configurations, each unit was operated at their normal operation. The results showed that all proposed configurations can improve the power generation and carbon dioxide utilization. At the optimal operation in each design showed two interesting configurations that are series (B) and series-parallel combination (D). System (B) is suitable for power generation improvement consideration with no NiO formation possibility found whereas system (D) is the one of the most suitable for carbon dioxide utilization but operating conditions should be carefully selected to avoid NiO.

9.1.3 Control structure of the SOFC and MCFC integrated system.

The integrated fuel cell system has shown an improved overall efficiency, the MCFC operation depends on the SOFC operation and their operating points were changed to maximize total power. Thus, the control of such a system could require a different control structure to achieve the best profit. In this study use the control structure design of Skogestad (2004) was used to select suitable manipulated variables and controlled variables. The cost function was defined to maximize power generation per fuel usage including carbon tax consideration with safe operational constraints. Three actively constrained regions were found by varying two feed disturbances. The self-optimizing method was used to select the best CVs for the remaining unconstrained degree of freedom. An evaluation of the losses with various disturbances showed that regions I and II could use the same control structure

(structure A). $T_{0f,S}$, $T_{0a,S}$, $y_{O_2,M_{0a}}$, y_{H_2,M_f} , $T_{0a,M}$, $T_{f,M}/T_{0f,M}$, y_{H_2O,B_0} and $U_{f,M}$ were found to be the control variables for structure A. For structure B, y_{H_2,M_f} was replaced with $y_{H_2,S}$. The MCFC was found to be the bottleneck of this system. Thus, $\dot{j}_M$ was selected as the TPM of the system. Structure A can be used without switching the control structure with limitation of feed disturbances range (±20%). Four temperature controls are clearly noticed the related MVs. However, the others are paired with MVs using RGA and were found that $F_{0a,S}$ (V-7) is used to control $y_{O_2,M_{0a}}$. $\dot{j}_S$ (V-18) is used to control y_{H_2,M_f} . $U_{f,M}$ is controlled by $F_{0f,M}$ (V-10) and $F_{0a,B}$ (V-15) is used to control y_{H_2O,B_0} . Those controllers using SIMC PID tuning method were able to control those CVs in both step set-point changes and step disturbances cases. Without additional voltage controllers the system cannot indirect control voltages. To control the voltages, it is recommended to repeat step S5 either using cascade control or MPC. However, MPC is more suitable as it able to deal with structure switching.

9.1.4 Design of the integrated SOFC and MCFC integrated system for coping with power demand by implementing a GT and AA-CAES.

Because fuel cells can be operated safely in a steady-state mode and thus, energy storage should be integrated within the fuel cell system to cope with the electricity demand variation. The afterburner was replaced with the combustion chamber of a gas turbine (GT) to generate more electrical energy, which was captured by advanced adiabatic compressed air energy storage (AA-CAES) for later use. This approach maintains constant power generation from the integrated fuel cell system during operation. The simulation results showed that the remaining fuel from the integrated fuel cell system was enough for additional power generation by GT. The result also revealed that the implementation of a GT into the integrated fuel cell system also slightly reduces; however, the total generating power was enhanced. The proposed system showed it can effectively handle the power variation without an additional fuel requirement. Pressure ratio of compressor part of GT and AA-CAES,

and additional air feed to the system are design parameters in this study. The added air ratio must be very small to reduce the loss in the power generation of the MCFC. The power generation of the hybrid system increases with an increase in GT pressure. However, pressure ratio of 6 is preferred for keeping the action of the heat exchanger no. 6 (cool down the stream). The AA-CAES pressure ratio range 8–15 is recommended for minimizing the storage volume and maintaining some air in the storage, which can be released to the atmosphere via the turbine to supply the power during very high demands. However, more detail on the physical limitations of the system must be considered before it can be practical used.

9.2   Future work recommendations

The more detail studies about the control structure design of the integrated SOFC-MCFC system and the design of the hybrid SOFC-MCFC-GT system with the AA-CAES should be further investigated due to the limitations found in these studies. The interesting topics are shown as follow;

1. In the control structure design study, it had shown the limitation of the control structure according to active constraints changes that the system needs a switch in control structure when the disturbances are too high. The switching in control structures cannot be provided by PID controllers which are implemented in this study. Hence, the advance controller such as MPC should be further investigated to cover the case of these switch.

2. To control fuel cell voltages, the result from the control structure design study also recommended that voltages should be directly controlled by considered as CV2.

3. The net heat requirement of the system should be considered to avoid using outsource heat to pre-heat the air feed.

4. To track the power demand in the design of the hybrid SOFC-MCFC-GT system with the AA-CAES study, the optimization for the AA-CAES operation that releases the energy to supply to power variation is interesting to be considered

To improve the accuracy of the model, other species in air, i.e., argon should be taken into account. In addition, pressure loss inside the units should be considered especially for the hybrid SOFC-MCFC-GT system study.

NOMENCLATURES

A	reaction area (L×W; m^2)
C	controlled variable
CEC	carbon dioxide emission coefficient (kg CO_2/kW-h)
Cp	heat capacity (kJ kg^{-1} K^{-1}, kJ $kmol^{-1}$ K^{-1})
d	disturbance
$D_{eff,i}$	effective diffusivity coefficient (m^2 s^{-1})
D_h	channel hydraulic diameter (m)
E	operating voltage (V)
E_i	activation energy (kJ mol^{-1})
E^0	open-circuit voltage at the standard pressure (V)
En	generated power per fuel feed ()
E_{OCV}	open-circuit voltage (V)
e	error
F	Faraday constant (C mol^{-1})
F	state feedback gains
F_i	molar flow rate of component i (mol s^{-1})
G	non-singular square complex matrix
g_{ij}	ij th element of G
H	enthalpy flow (kW)
h_a	Air channel height (m)
$\dot{h}_i$	enthalpy of component i (kJ mol^{-1})
j	current density (A m^{-2})
J	cost function
$j_{0, electrode}$	exchange current density of electrode (A m^{-2})
K_c	proportional gain
k_i	pre-exponential factor of electrode (A m^{-2})
k	plant gain
k	thermal conductivity (kW m^{-1} K^{-1})
L	cell length (m)
LHV_i	low heating value of component i (kJ $kmol^{-1}$, kJ kg^{-1})

loss L	loss due to self-optimizing control implementation
$\dot{m}_f$	mass flow rate (kg s^{-1})
N_i	Mole of component i
N_{ss}	number of steady-state degrees of freedom
N_{valves}	numbers of dynamic DOFs
N_{0y}	numbers of controlled variables
$N_{0,valves}$	numbers of purely dynamic control DOFs
Nu	Nusselt number, 3.09 (-)
n	number of electrons transferred
P_i	partial pressure of component i (atm)
P	pressure (atm)
$P_{D,W}$	power density of fuel cell W (W cm^{-2})
P_W	power of unit W (W)
Q_i	enthalpy flow of component i (kW)
Q_i	heat required or obtained (kW)
$\Re$	gas constant (kJ mol^{-1} K^{-1})
R_j	rate of reaction j (mol s^{-1} m^{-2})
R_i	equivalent global resistances (Ω cm^2)
R_{Ohm}	internal resistance of the cell (Ω m^{-2})
t	time (s)
T	temperature (K)
T^0	standard temperature (298.15 K)
u	degrees of freedom
u_j	control input
U_f	fuel utilization factor
V	Volume (m^3)
E	fuel cell voltage (V)
W	cell width (m)
x	state variables
y_j	plant output
y_i	molar fraction of component i

Greek symbols

α	transfer coefficient
γ	polytrophic factor
$\in$	emissivity
β	pressure ratio
ΔG	Gibbs free energy change (kJ mol^{-1})
ΔH	heat of reaction (kJ mol^{-1})
η_{act}	activation overpotentials (V)
η_{conc}	concentration overpotentials (V)
η_{ohm}	ohmic loss (V)
η_{loss}	total loss (V)
η_i	efficiency (%)
λ_{air}	excess air ratio
λ_{ij}	relative gain
θ	time delay
ρ	density (kg m^{-3})
σ_i	electronic conductivity of layer i (Ω^{-1} m^{-1})
σ	Stefan-Boltzmann constant (W m^{-2} K^{-4})
τ_1	time constant
τ_2	second-order lag time constant
τ_i	thickness of layer i (m)
τ_c	response time constant
τ_D	derivative gain
τ_I	integral gain
$\upsilon_{i,k}$	stoichiometric coefficient of component i in reaction k

Superscripts

0	standard conditions
-1	inverse of matrix
SP	setpoint
T	transpose of matrix

Subscripts

0	feed conditions (fuel and air channel inlet)
a	air channel
act	activation
an	anode
B	afterburner
C	charge
ca	cathode
com	compressor
con	concentration
D	discharge
E	electro chemical reaction
el	eletrolyte
ele	electrical
f	fuel channel
GT	gas turbine
i	chemical component
I	Interconnect
ir	internal resistance
K	reaction
M	molten carbonate fuel cell
OCV	open-circuit voltage
Ohm	Ohmic
Opt	optimal value
P	PEN structure
R	reformer
ref	reference
S	solid oxide fuel cell
SR	steam reforming reaction
ss	steady state condition
TES	Thermal energy storage
th	thermal

TPB	three-phase boundary
tur	turbine
WGS	water-gas-shift reaction

จุฬาลงกรณ์มหาวิทยาลัย
CHULALONGKORN UNIVERSITY

REFERENCES

Achenbach, E. (1994). Three-dimensional and time-dependent simulation of a planar solid oxide fuel cell stack. *Journal of Power Sources, 49*(1), 333-348. doi:https://doi.org/10.1016/0378-7753(93)01833-4

Adams II, T. A., Nease, J., Tucker, D., & Barton, P. I. (2013). Energy conversion with solid oxide fuel cell systems: A review of concepts and outlooks for the short- and long-term. *Industrial and Engineering Chemistry Research, 52*(9), 3089-3111. doi:10.1021/ie300996r

Adamson, K.-A. (2007). 2 - Fuel cell basics. In K.-A. Adamson (Ed.), *Stationary Fuel Cells* (pp. 7-28). Oxford: Elsevier.

Aghaie, M., Mehrpooya, M., & Pourfayaz, F. (2016). Introducing an integrated chemical looping hydrogen production, inherent carbon capture and solid oxide fuel cell biomass fueled power plant process configuration. *Energy Conversion and Management, 124*, 141-154. doi:10.1016/j.enconman.2016.07.001

Aguiar, P., Adjiman, C. S., & Brandon, N. P. (2004). Anode-supported intermediate temperature direct internal reforming solid oxide fuel cell. I: model-based steady-state performance. *Journal of Power Sources, 138*(1), 120-136. doi:https://doi.org/10.1016/j.jpowsour.2004.06.040

Aguiar, P., Adjiman, C. S., & Brandon, N. P. (2005). Anode-supported intermediate-temperature direct internal reforming solid oxide fuel cell: II. Model-based dynamic performance and control. *Journal of Power Sources, 147*(1-2), 136-147. doi:10.1016/j.jpowsour.2005.01.017

Aguiar, P., Chadwick, D., & Kershenbaum, L. (2002). Modelling of an indirect internal reforming solid oxide fuel cell. *Chemical Engineering Science, 57*(10), 1665-1677. doi:https://doi.org/10.1016/S0009-2509(02)00058-1

Antolini, E. (2011). The stability of molten carbonate fuel cell electrodes: A review of recent improvements. *Applied Energy, 88*(12), 4274-4293. doi:https://doi.org/10.1016/j.apenergy.2011.07.009

Araki, T., Ohba, T., Takezawa, S., Onda, K., & Sakaki, Y. (2006). Cycle analysis of planar SOFC power generation with serial connection of low and high temperature SOFCs. *Journal of Power Sources, 158*(1), 52-59. doi:10.1016/j.jpowsour.2005.09.003

Arpornwichanop, A., Chalermpanchai, N., Patcharavorachot, Y., Assabumrungrat, S., & Tade, M. (2009). Performance of an anode-supported solid oxide fuel cell with direct-internal reforming of ethanol. *International Journal of Hydrogen Energy, 34*(18), 7780-7788. doi:10.1016/j.ijhydene.2009.07.006

Arpornwichanop, A., Patcharavorachot, Y., & Assabumrungrat, S. (2010). Analysis of a proton-conducting SOFC with direct internal reforming. *Chemical Engineering Science, 65*(1), 581-589. doi:10.1016/j.ces.2009.06.066

Bakalis, D. P., & Stamatis, A. G. (2014). Optimization methodology of turbomachines for hybrid SOFC-GT applications. *Energy, 70*, 86-94. doi:10.1016/j.energy.2014.03.093

Baldinelli, A., Barelli, L., & Bidini, G. (2015). Performance characterization and modelling of syngas-fed SOFCs (solid oxide fuel cells) varying fuel composition. *Energy, 90*, 2070-2084. doi:10.1016/j.energy.2015.07.126

Baldinelli, A., Cinti, G., Desideri, U., & Fantozzi, F. (2016). Biomass integrated

gasifier-fuel cells: Experimental investigation on wood syngas tars impact on NiYSZ-anode Solid Oxide Fuel Cells. *Energy Conversion and Management, 128*, 361-370. doi:https://doi.org/10.1016/j.enconman.2016.09.048

Bavarian, M., Soroush, M., Kevrekidis, I. G., & Benziger, J. B. (2010). Mathematical modeling, steady-state and dynamic behavior, and control of fuel cells: A review. *Industrial and Engineering Chemistry Research, 49*(17), 7922-7950. doi:10.1021/ie100032c

Bizon, N., Oproescu, M., & Raceanu, M. (2015). Efficient energy control strategies for a standalone Renewable/Fuel Cell Hybrid Power Source. *Energy Conversion and Management, 90*, 93-110. doi:10.1016/j.enconman.2014.11.002

Braun, R. J., Vincent, T. L., Zhu, H., & Kee, R. J. (2012) Analysis, Optimization, and Control of Solid-Oxide Fuel Cell Systems. In*: Vol. 41. Advances in Chemical Engineering* (pp. 383-446).

Bristol, E. H. (1966). On a new measure of interaction for multivariable process control. *IEEE Transactions on Automatic Control, 11*(1), 133-134. doi:10.1109/TAC.1966.1098266

Budt, M., Wolf, D., Span, R., & Yan, J. (2016). A review on compressed air energy storage: Basic principles, past milestones and recent developments. *Applied Energy, 170*, 250-268. doi:https://doi.org/10.1016/j.apenergy.2016.02.108

Campanari, S. (2002). Carbon dioxide separation from high temperature fuel cell power plants. *Journal of Power Sources, 112*(1), 273-289. doi:https://doi.org/10.1016/S0378-7753(02)00395-6

Campanari, S., Mastropasqua, L., Gazzani, M., Chiesa, P., & Romano, M. C. (2016). Predicting the ultimate potential of natural gas SOFC power cycles with CO2 capture - Part B: Applications. *Journal of Power Sources, 325*, 194-208. doi:10.1016/j.jpowsour.2016.05.134

Caprile, L., Passalacqua, B., & Torazza, A. (2011). Carbon capture: Energy wasting technologies or the MCFCs challenge? *International Journal of Hydrogen Energy, 36*(16), 10269-10277. doi:https://doi.org/10.1016/j.ijhydene.2010.10.028

Carapellucci, R., Saia, R., & Giordano, L. (2014). Study of Gas-steam Combined Cycle Power Plants Integrated with MCFC for Carbon Dioxide Capture. *Energy Procedia, 45*, 1155-1164. doi:https://doi.org/10.1016/j.egypro.2014.01.121

Carter, D., & Wing, J. (2013, September 2013). The Fuel Cell Industry Review 2013. *FuelCellToday, 50*.

Chaisantikulwat, A., Diaz-Goano, C., & Meadows, E. S. (2008). Dynamic modelling and control of planar anode-supported solid oxide fuel cell. *Computers and Chemical Engineering, 32*(10), 2365-2381. doi:10.1016/j.compchemeng.2007.12.003

Chan, S. H., Khor, K. A., & Xia, Z. T. (2001). A complete polarization model of a solid oxide fuel cell and its sensitivity to the change of cell component thickness. *Journal of Power Sources, 93*(1), 130-140. doi:https://doi.org/10.1016/S0378-7753(00)00556-5

Chatrattanawet, N., Skogestad, S., & Arpornwichanop, A. (2015). Control structure design and dynamic modeling for a solid oxide fuel cell with direct internal reforming of methane. *Chemical Engineering Research and Design, 98*, 202-211. doi:10.1016/j.cherd.2015.04.029

Chen, H., Wang, C., & Ye, M. (2016). An uncertainty analysis of subsidy for carbon capture and storage (CCS) retrofitting investment in China's coal power plants using a real-options approach. *Journal of Cleaner Production, 137*, 200-212. doi:10.1016/j.jclepro.2016.07.074

Chien, A. C., & Irvine, J. T. S. (2013). 19 - Hybrid Molten Carbonate/Solid Oxide Direct Carbon Fuel Cells. In F. Lantelme & H. Groult (Eds.), *Molten Salts Chemistry* (pp. 403-414). Oxford: Elsevier.

Choudhury, A., Chandra, H., & Arora, A. (2013). Application of solid oxide fuel cell technology for power generation—A review. *Renewable and Sustainable Energy Reviews, 20*, 430-442. doi:https://doi.org/10.1016/j.rser.2012.11.031

Cocco, D., & Tola, V. (2009a). Externally reformed solid oxide fuel cell–micro-gas turbine (SOFC–MGT) hybrid systems fueled by methanol and di-methyl-ether (DME). *Energy, 34*(12), 2124-2130. doi:https://doi.org/10.1016/j.energy.2008.09.013

Cocco, D., & Tola, V. (2009b). Use of alternative hydrogen energy carriers in SOFC-MGT hybrid power plants. *Energy Conversion and Management, 50*(4), 1040-1048. doi:10.1016/j.enconman.2008.12.019

Curletti, F., Gandiglio, M., Lanzini, A., Santarelli, M., & Maréchal, F. (2015). Large size biogas-fed Solid Oxide Fuel Cell power plants with carbon dioxide management: Technical and economic optimization. *Journal of Power Sources, 294*, 669-690. doi:10.1016/j.jpowsour.2015.06.091

da Rosa, A. (2009). *Fundamentals of Renewable Energy Processes*.

Davis, W., & Martín, M. (2014). Optimal year-round operation for methane production from CO2 and water using wind and/or solar energy. *Journal of Cleaner Production, 80*, 252-261. doi:10.1016/j.jclepro.2014.05.077

Della Pietra, M., McPhail, S. J., Prabhakar, S., Desideri, U., Nam, S. W., & Cigolotti, V. (2016). Accelerated test for MCFC button cells: First findings. *International Journal of Hydrogen Energy, 41*(41), 18807-18814. doi:10.1016/j.ijhydene.2016.07.021

Dicks, A. L., Fellows, R. G., Martin Mescal, C., & Seymour, C. (2000). A study of SOFC–PEM hybrid systems. *Journal of Power Sources, 86*(1), 501-506. doi:https://doi.org/10.1016/S0378-7753(99)00492-9

Discepoli, G., Cinti, G., Desideri, U., Penchini, D., & Proietti, S. (2012). Carbon capture with molten carbonate fuel cells: Experimental tests and fuel cell performance assessment. *International Journal of Greenhouse Gas Control, 9*, 372-384. doi:https://doi.org/10.1016/j.ijggc.2012.05.002

Discepoli, G., Milewski, J., & Desideri, U. (2016). Off-design operation of coal power plant integrated with natural gas fueled molten carbonate fuel cell as CO2reducer. *International Journal of Hydrogen Energy, 41*(8), 4773-4783. doi:10.1016/j.ijhydene.2016.01.065

Doyle, T. S., Dehouche, Z., Aravind, P. V., Liu, M., & Stankovic, S. (2014). Investigating the impact and reaction pathway of toluene on a SOFC running on syngas. *International Journal of Hydrogen Energy, 39*(23), 12083-12091. doi:10.1016/j.ijhydene.2014.05.148

EG&G Technical Services, I. (2004). *Fuel Cell Handbook* (Seventh ed.). United States: U.S. Department of Energy.

El-Emam, R. S., & Dincer, I. (2011). Energy and exergy analyses of a combined molten

carbonate fuel cell – Gas turbine system. *International Journal of Hydrogen Energy, 36*(15), 8927-8935. doi:https://doi.org/10.1016/j.ijhydene.2011.04.228

Frangini, S., & Masi, A. (2016). Molten carbonates for advanced and sustainable energy applications: Part II. Review of recent literature. *International Journal of Hydrogen Energy, 41*(42), 18971-18994. doi:10.1016/j.ijhydene.2016.08.076

Freni, S., Aquino, M., & Passalacqua, E. (1994). Molten carbonate fuel cell with indirect internal reforming. *Journal of Power Sources, 52*(1), 41-47. doi:https://doi.org/10.1016/0378-7753(94)01930-4

Georgis, D., Jogwar, S. S., Almansoori, A. S., & Daoutidis, P. (2011). Design and control of energy integrated SOFC systems for in situ hydrogen production and power generation. *Computers & Chemical Engineering, 35*(9), 1691-1704. doi:https://doi.org/10.1016/j.compchemeng.2011.02.006

Gil, A., Medrano, M., Martorell, I., Lázaro, A., Dolado, P., Zalba, B., & Cabeza, L. F. (2010). State of the art on high temperature thermal energy storage for power generation. Part 1—Concepts, materials and modellization. *Renewable and Sustainable Energy Reviews, 14*(1), 31-55. doi:https://doi.org/10.1016/j.rser.2009.07.035

Greppi, P., Bosio, B., & Arato, E. (2013). Membranes and molten carbonate fuel cells to capture CO2 and increase energy production in natural gas power plants. *Industrial and Engineering Chemistry Research, 52*(26), 8755-8764. doi:10.1021/ie302725a

Guney, M. S., & Tepe, Y. (2017). Classification and assessment of energy storage systems. *Renewable and Sustainable Energy Reviews, 75*, 1187-1197. doi:https://doi.org/10.1016/j.rser.2016.11.102

Haberman, B. A., & Young, J. B. (2004). Three-dimensional simulation of chemically reacting gas flows in the porous support structure of an integrated-planar solid oxide fuel cell. *International Journal of Heat and Mass Transfer, 47*(17), 3617-3629. doi:https://doi.org/10.1016/j.ijheatmasstransfer.2004.04.010

Hajimolana, S. A., & Soroush, M. (2009). *Dynamic behavior and control of a tubular solid-oxide fuel cell system.* Paper presented at the Proceedings of the American Control Conference.

Haseli, Y., Dincer, I., & Naterer, G. F. (2008). Thermodynamic modeling of a gas turbine cycle combined with a solid oxide fuel cell. *International Journal of Hydrogen Energy, 33*(20), 5811-5822. doi:https://doi.org/10.1016/j.ijhydene.2008.05.036

Hosseinpour, J., Sadeghi, M., Chitsaz, A., Ranjbar, F., & Rosen, M. A. (2017). Exergy assessment and optimization of a cogeneration system based on a solid oxide fuel cell integrated with a Stirling engine. *Energy Conversion and Management, 143*, 448-458. doi:10.1016/j.enconman.2017.04.021

Hu, Q., Wang, S., & Wen, T.-L. (2008). Analysis of processes in planar solid oxide fuel cells. *Solid State Ionics, 179*(27), 1579-1587. doi:https://doi.org/10.1016/j.ssi.2008.02.007

Huang, B., Qi, Y., & Murshed, M. (2011). Solid oxide fuel cell: Perspective of dynamic modeling and control. *Journal of Process Control, 21*(10), 1426-1437. doi:10.1016/j.jprocont.2011.06.017

Ibrahim, H., Ilinca, A., & Perron, J. (2008). Energy storage systems—Characteristics and comparisons. *Renewable and Sustainable Energy Reviews, 12*(5), 1221-

1250. doi:https://doi.org/10.1016/j.rser.2007.01.023

Janardhanan, V. M., Heuveline, V., & Deutschmann, O. (2007). Performance analysis of a SOFC under direct internal reforming conditions. *Journal of Power Sources, 172*(1), 296-307. doi:10.1016/j.jpowsour.2007.07.008

Jienkulsawad, P., & Arpornwichanop, A. (2016). Investigating the performance of a solid oxide fuel cell and a molten carbonate fuel cell combined system. *Energy, 107*, 843-853. doi:10.1016/j.energy.2016.04.072

Jienkulsawad, P., Saebea, D., Patcharavorachot, Y., & Arpornwichanop, A. (2015). Design of the integrated solid oxide fuel cell and molten carbonate fuel cell system to reduce carbon dioxide emissions. *Chemical Engineering Transactions, 43*, 2191-2196. doi:10.3303/CET1543366

Jienkulsawad, P., Saebea, D., Patcharavorachot, Y., Kheawhom, S., & Arpornwichanop, A. (2018). Analysis of a solid oxide fuel cell and a molten carbonate fuel cell integrated system with different configurations. *International Journal of Hydrogen Energy, 43*(2), 932-942. doi:10.1016/j.ijhydene.2017.10.168

Jienkulsawad, P., Skogestad, S., & Arpornwichanop, A. (2017). Control structure design of a solid oxide fuel cell and a molten carbonate fuel cell integrated system: Top-down analysis. *Energy Conversion and Management, 152*, 88-98. doi:10.1016/j.enconman.2017.09.033

Kakaç, S., Pramuanjaroenkij, A., & Zhou, X. Y. (2007). A review of numerical modeling of solid oxide fuel cells. *International Journal of Hydrogen Energy, 32*(7), 761-786. doi:https://doi.org/10.1016/j.ijhydene.2006.11.028

Kandepu, R., Imsland, L., Foss, B. A., Stiller, C., Thorud, B., & Bolland, O. (2007). Modeling and control of a SOFC-GT-based autonomous power system. *Energy, 32*(4), 406-417. doi:https://doi.org/10.1016/j.energy.2006.07.034

Kaneko, T., Brouwer, J., & Samuelsen, G. S. (2006). Power and temperature control of fluctuating biomass gas fueled solid oxide fuel cell and micro gas turbine hybrid system. *Journal of Power Sources, 160*(1), 316-325. doi:https://doi.org/10.1016/j.jpowsour.2006.01.044

Klein, D. E. (2016). CO2 emission trends for the US and electric power sector. *The Electricity Journal, 29*(8), 33-47. doi:https://doi.org/10.1016/j.tej.2016.09.008

Klein, D. E. (2016). CO2 emission trends for the US and electric power sector. *Electricity Journal, 29*(8), 33-47. doi:10.1016/j.tej.2016.09.008

Kulikovsky, A. A. (2009). A model for SOFC anode performance. *Electrochimica Acta, 54*(26), 6686-6695. doi:https://doi.org/10.1016/j.electacta.2009.06.054

Laosiripojana, N., & Assabumrungrat, S. (2007). Catalytic steam reforming of methane, methanol, and ethanol over Ni/YSZ: The possible use of these fuels in internal reforming SOFC. *Journal of Power Sources, 163*(2), 943-951. doi:10.1016/j.jpowsour.2006.10.006

Laurencin, J., Lefebvre-Joud, F., & Delette, G. (2008). Impact of cell design and operating conditions on the performances of SOFC fuelled with methane. *Journal of Power Sources, 177*(2), 355-368. doi:https://doi.org/10.1016/j.jpowsour.2007.11.099

Liu, A., & Weng, Y. (2010). Modeling of molten carbonate fuel cell based on the volume-resistance characteristics and experimental analysis. *Journal of Power Sources, 195*(7), 1872-1879. doi:10.1016/j.jpowsour.2009.10.040

Mahdy, A., Mendez, L., Ballesteros, M., & González-Fernández, C. (2014). Enhanced

methane production of Chlorella vulgaris and Chlamydomonas reinhardtii by hydrolytic enzymes addition. *Energy Conversion and Management, 85*, 551-557. doi:10.1016/j.enconman.2014.04.097

Martín, M., & Davis, W. (2015). Optimal integration of the year-round operation for methane production from CO2 and water using wind, solar and biomass. In K. V. Gernaey, J. K. Huusom, & R. Gani (Eds.), *Computer Aided Chemical Engineering* (Vol. 37, pp. 2261-2266): Elsevier.

McLarty, D., Brouwer, J., & Samuelsen, S. (2014). Fuel cell–gas turbine hybrid system design part I: Steady state performance. *Journal of Power Sources, 257*, 412-420. doi:https://doi.org/10.1016/j.jpowsour.2013.11.122

McPhail, S. J., Aarva, A., Devianto, H., Bove, R., & Moreno, A. (2011). SOFC and MCFC: Commonalities and opportunities for integrated research. *International Journal of Hydrogen Energy, 36*(16), 10337-10345. doi:10.1016/j.ijhydene.2010.09.071

Mehmeti, A., Santoni, F., Della Pietra, M., & McPhail, S. J. (2016). Life cycle assessment of molten carbonate fuel cells: State of the art and strategies for the future. *Journal of Power Sources, 308*, 97-108. doi:10.1016/j.jpowsour.2015.12.023

Milewski, J., Wołowicz, M., Miller, A., & Bernat, R. (2013). A reduced order model of Molten Carbonate Fuel Cell: A proposal. *International Journal of Hydrogen Energy, 38*(26), 11565-11575. doi:10.1016/j.ijhydene.2013.06.002

Minasidis, V., Skogestad, S., & Kaistha, N. (2015) Simple Rules for Economic Plantwide Control. In*: Vol. 37. Computer Aided Chemical Engineering* (pp. 101-108).

Morita, H., Komoda, M., Mugikura, Y., Izaki, Y., Watanabe, T., Masuda, Y., & Matsuyama, T. (2002). Performance analysis of molten carbonate fuel cell using a Li/Na electrolyte. *Journal of Power Sources, 112*(2), 509-518. doi:10.1016/S0378-7753(02)00468-8

Mozayeni, H., Negnevitsky, M., Wang, X., Cao, F., & Peng, X. (2017). Performance Study of an Advanced Adiabatic Compressed Air Energy Storage System. *Energy Procedia, 110*, 71-76. doi:https://doi.org/10.1016/j.egypro.2017.03.108

Muñoz De Escalona, J. M., Sánchez, D., Chacartegui, R., & Sánchez, T. (2011). A step-by-step methodology to construct a model of performance of molten carbonate fuel cells with internal reforming. *International Journal of Hydrogen Energy, 36*(24), 15739-15751. doi:10.1016/j.ijhydene.2011.08.094

Murshed, A. M., Huang, B., & Nandakumar, K. (2007). Control relevant modeling of planer solid oxide fuel cell system. *Journal of Power Sources, 163*(2), 830-845. doi:https://doi.org/10.1016/j.jpowsour.2006.09.080

Musa, A., & De Paepe, M. (2008). Performance of combined internally reformed intermediate/high temperature SOFC cycle compared to internally reformed two-staged intermediate temperature SOFC cycle. *International Journal of Hydrogen Energy, 33*(17), 4665-4672. doi:https://doi.org/10.1016/j.ijhydene.2008.05.093

Mustapha, N. A., Sharuddin, S. S., Mohd Zainudin, M. H., Ramli, N., Shirai, Y., & Maeda, T. (2017). Inhibition of methane production by the palm oil industrial waste phospholine gum in a mimic enteric fermentation. *Journal of Cleaner Production, 165*, 621-629. doi:https://doi.org/10.1016/j.jclepro.2017.07.129

Nabae, Y., Pointon, K. D., & Irvine, J. T. S. (2008). Electrochemical oxidation of solid

carbon in hybrid DCFC with solid oxide and molten carbonate binary electrolyte. *Energy and Environmental Science, 1*(1), 148-155. doi:10.1039/b804785e

Nease, J., & Adams Ii, T. A. (2014). Coal-fuelled systems for peaking power with 100% CO2 capture through integration of solid oxide fuel cells with compressed air energy storage. *Journal of Power Sources, 251*, 92-107. doi:10.1016/j.jpowsour.2013.11.040

Nease, J., Monteiro, N., & Adams, T. A. (2016). Application of a Multiple Time-Scale Rolling Horizon Optimization Technique for Improved Load-Following of an Integrated SOFC/CAES Plant with Zero Emissions. In Z. Kravanja & M. Bogataj (Eds.), *Computer Aided Chemical Engineering* (Vol. 38, pp. 1725-1730): Elsevier.

Nehter, P. (2007). A high fuel utilizing solid oxide fuel cell cycle with regard to the formation of nickel oxide and power density. *Journal of Power Sources, 164*(1), 252-259. doi:10.1016/j.jpowsour.2006.08.037

Ni, M. (2009). Computational fluid dynamics modeling of a solid oxide electrolyzer cell for hydrogen production. *International Journal of Hydrogen Energy, 34*(18), 7795-7806. doi:https://doi.org/10.1016/j.ijhydene.2009.07.080

Nishikawa, H., Sasou, H., Kurihara, R., Nakamura, S., Kano, A., Tanaka, K., . . . Ogami, Y. (2008). High fuel utilization operation of pure hydrogen fuel cells. *International Journal of Hydrogen Energy, 33*(21), 6262-6269. doi:10.1016/j.ijhydene.2008.07.019

O'Hayre, R. P., Cha, S.-W., Colella, W. G., & Prinz, F. B. (2009). *Fuel Cell Fundamentals* (2 edition ed.). United States of America: John Wiley & Sons.

Obara, S. (2010). Power generation efficiency of an SOFC-PEFC combined system with time shift utilization of SOFC exhaust heat. *International Journal of Hydrogen Energy, 35*(2), 757-767. doi:10.1016/j.ijhydene.2009.11.032

Orecchini, F., Bocci, E., & Di Carlo, A. (2006). MCFC and microturbine power plant simulation. *Journal of Power Sources, 160*(2), 835-841. doi:https://doi.org/10.1016/j.jpowsour.2006.04.094

Ovrum, E., & Dimopoulos, G. (2012). A validated dynamic model of the first marine molten carbonate fuel cell. *Applied Thermal Engineering, 35*(1), 15-28. doi:10.1016/j.applthermaleng.2011.09.023

Panahi, M., Karimi, M., Skogestad, S., Hillestad, M., & Svendsen, H. F. (2010). Self-Optimizing and Control Structure Design for a CO2 Capturing Plant. In F. Benyahia & F. T. Eljack (Eds.), *Proceedings of the 2nd Annual Gas Processing Symposium* (Vol. 2, pp. 331-338). Amsterdam: Elsevier.

Papurello, D., Lanzini, A., Tognana, L., Silvestri, S., & Santarelli, M. (2015). Waste to energy: Exploitation of biogas from organic waste in a 500 Wel solid oxide fuel cell (SOFC) stack. *Energy, 85*, 145-158. doi:10.1016/j.energy.2015.03.093

Parhizkar, T., & Roshandel, R. (2017). Long term performance degradation analysis and optimization of anode supported solid oxide fuel cell stacks. *Energy Conversion and Management, 133*, 20-30. doi:10.1016/j.enconman.2016.11.045

Pastorino, R., Budinis, S., Currò, F., Palazzi, E., & Fabiano, B. (2011). Syngas fuel cells: From process development to risk assessment. *Chemical Engineering Transactions, 24*, 1081-1086. doi:10.3303/CET1124181

Patcharavorachot, Y., Arpornwichanop, A., & Chuachuensuk, A. (2008).

Electrochemical study of a planar solid oxide fuel cell: Role of support structures. *Journal of Power Sources, 177*(2), 254-261. doi:https://doi.org/10.1016/j.jpowsour.2007.11.079

Patcharavorachot, Y., Paengjuntuek, W., Assabumrungrat, S., & Arpornwichanop, A. (2010). Performance evaluation of combined solid oxide fuel cells with different electrolytes. *International Journal of Hydrogen Energy, 35*(9), 4301-4310. doi:https://doi.org/10.1016/j.ijhydene.2010.02.057

Paul, A., Beasley, B., & Palmer, K. (2013). Taxing Electricity Sector Carbon Emissions at Social Cost. *Resources for the Future*

Peters, R., Deja, R., Blum, L., Pennanen, J., Kiviaho, J., & Hakala, T. (2013). Analysis of solid oxide fuel cell system concepts with anode recycling. *International Journal of Hydrogen Energy, 38*(16), 6809-6820. doi:https://doi.org/10.1016/j.ijhydene.2013.03.110

Rinaldi, G., McLarty, D., Brouwer, J., Lanzini, A., & Santarelli, M. (2015). Study of CO2 recovery in a carbonate fuel cell tri-generation plant. *Journal of Power Sources, 284*, 16-26. doi:10.1016/j.jpowsour.2015.02.147

Rochedo, P. R. R., Costa, I. V. L., Império, M., Hoffmann, B. S., Merschmann, P. R. D. C., Oliveira, C. C. N., . . . Schaeffer, R. (2016). Carbon capture potential and costs in Brazil. *Journal of Cleaner Production, 131*, 280-295. doi:10.1016/j.jclepro.2016.05.033

Rokni, M. (2013). Thermodynamic analysis of SOFC (solid oxide fuel cell)-Stirling hybrid plants using alternative fuels. *Energy, 61*, 87-97. doi:10.1016/j.energy.2013.06.001

Saebea, D., Authayanun, S., Patcharavorachot, Y., Paengjuntuek, W., & Arpornwichanop, A. (2013). Use of different renewable fuels in a steam reformer integrated into a solid oxide fuel cell: Theoretical analysis and performance comparison. *Energy, 51*, 305-313. doi:https://doi.org/10.1016/j.energy.2012.12.014

Saebea, D., Patcharavorachot, Y., & Arpornwichanop, A. (2012). Analysis of an ethanol-fuelled solid oxide fuel cell system using partial anode exhaust gas recirculation. *Journal of Power Sources, 208*, 120-130. doi:10.1016/j.jpowsour.2012.02.023

Saebea, D., Patcharavorachot, Y., Assabumrungrat, S., & Arpornwichanop, A. (2013). Analysis of a pressurized solid oxide fuel cell-gas turbine hybrid power system with cathode gas recirculation. *International Journal of Hydrogen Energy, 38*(11), 4748-4759. doi:10.1016/j.ijhydene.2013.01.146

Samanta, S., & Ghosh, S. (2017). Techno-economic assessment of a repowering scheme for a coal fired power plant through upstream integration of SOFC and downstream integration of MCFC. *International Journal of Greenhouse Gas Control, 64*, 234-245. doi:https://doi.org/10.1016/j.ijggc.2017.07.020

Sarmah, P., & Gogoi, T. K. (2017). Performance comparison of SOFC integrated combined power systems with three different bottoming steam turbine cycles. *Energy Conversion and Management, 132*, 91-101. doi:10.1016/j.enconman.2016.11.009

Sheng, L., Zhou, Z., Charpentier, J. F., & Benbouzid, M. E. H. (2017). Stand-alone island daily power management using a tidal turbine farm and an ocean compressed air energy storage system. *Renewable Energy, 103*, 286-294.

doi:10.1016/j.renene.2016.11.042

Singhal, S. C. (2002). Solid oxide fuel cells for stationary, mobile, and military applications. *Solid State Ionics, 152-153*, 405-410. doi:https://doi.org/10.1016/S0167-2738(02)00349-1

Skogestad, S. (2000). Plantwide control: the search for the self-optimizing control structure. *Journal of Process Control, 10*(5), 487-507. doi:https://doi.org/10.1016/S0959-1524(00)00023-8

Skogestad, S. (2003). Simple analytic rules for model reduction and PID controller tuning. *Journal of Process Control, 13*(4), 291-309. doi:https://doi.org/10.1016/S0959-1524(02)00062-8

Skogestad, S. (2004). Control structure design for complete chemical plants. *Computers and Chemical Engineering, 28*(1-2), 219-234. doi:10.1016/j.compchemeng.2003.08.002

Skogestad, S., & Postlethwaite, I. (2005). *MULTIVARIABLE FEEDBACK CONTROL: Analysis and Design* (2nd Edition ed.).

Spinelli, M., Romano, M. C., Consonni, S., Campanari, S., Marchi, M., & Cinti, G. (2014). Application of Molten Carbonate Fuel Cells in Cement Plants for CO2 Capture and Clean Power Generation. *Energy Procedia, 63*, 6517-6526. doi:https://doi.org/10.1016/j.egypro.2014.11.687

Tomczyk, P. (2006). MCFC versus other fuel cells—Characteristics, technologies and prospects. *Journal of Power Sources, 160*(2), 858-862. doi:https://doi.org/10.1016/j.jpowsour.2006.04.071

Wang, M., Zhao, P., Wu, Y., & Dai, Y. (2015). Performance analysis of a novel energy storage system based on liquid carbon dioxide. *Applied Thermal Engineering, 91*, 812-823. doi:https://doi.org/10.1016/j.applthermaleng.2015.08.081

Wee, J.-H. (2010). Contribution of fuel cell systems to CO2 emission reduction in their application fields. *Renewable and Sustainable Energy Reviews, 14*(2), 735-744. doi:https://doi.org/10.1016/j.rser.2009.10.013

Wee, J. H. (2014). Carbon dioxide emission reduction using molten carbonate fuel cell systems. *Renewable and Sustainable Energy Reviews, 32*, 178-191. doi:10.1016/j.rser.2014.01.034

Williams, M. C., & Maru, H. C. (2006). Distributed generation—Molten carbonate fuel cells. *Journal of Power Sources, 160*(2), 863-867. doi:https://doi.org/10.1016/j.jpowsour.2006.05.019

Xi, H., Varigonda, S., & Jing, B. (2010). *Dynamic modeling of a solid oxide fuel cell system for control design.* Paper presented at the Proceedings of the 2010 American Control Conference, ACC 2010.

Xin, X., Lü, Z., Huang, X., Sha, X., Zhang, Y., & Su, W. (2006). Anode-supported solid oxide fuel cell based on dense electrolyte membrane fabricated by filter-coating. *Journal of Power Sources, 159*(2), 1158-1161. doi:https://doi.org/10.1016/j.jpowsour.2005.12.015

Yang, Y., Du, X., Yang, L., Huang, Y., & Xian, H. (2009). Investigation of methane steam reforming in planar porous support of solid oxide fuel cell. *Applied Thermal Engineering, 29*(5), 1106-1113. doi:https://doi.org/10.1016/j.applthermaleng.2008.05.027

Yang, Y., Du, X., Yang, L., Huang, Y., & Xian, H. (2009). Investigation of methane steam reforming in planar porous support of solid oxide fuel cell. *Applied*

Thermal Engineering, 29(5-6), 1106-1113.
doi:10.1016/j.applthermaleng.2008.05.027

Yang, Y., Zhang, Y., Li, Z., Zhao, Z., Quan, X., & Zhao, Z. (2017). Adding granular activated carbon into anaerobic sludge digestion to promote methane production and sludge decomposition. *Journal of Cleaner Production, 149*, 1101-1108. doi:10.1016/j.jclepro.2017.02.156

Yokoo, M., & Take, T. (2004). Simulation analysis of a system combining solid oxide and polymer electrolyte fuel cells. *Journal of Power Sources, 137*(2), 206-215. doi:10.1016/j.jpowsour.2004.06.007

Zhang, H., Kong, W., Dong, F., Xu, H., Chen, B., & Ni, M. (2017). Application of cascading thermoelectric generator and cooler for waste heat recovery from solid oxide fuel cells. *Energy Conversion and Management, 148*, 1382-1390. doi:10.1016/j.enconman.2017.06.089

Zhang, L., Xing, Y., Xu, H., Wang, H., Zhong, J., & Xuan, J. (2017). Comparative study of solid oxide fuel cell combined heat and power system with Multi-Stage Exhaust Chemical Energy Recycling: Modeling, experiment and optimization. *Energy Conversion and Management, 139*, 79-88. doi:10.1016/j.enconman.2017.02.045

Zhang, Y., Yang, K., Hong, H., Zhong, X., & Xu, J. (2016). Thermodynamic analysis of a novel energy storage system with carbon dioxide as working fluid. *Renewable Energy, 99*, 682-697. doi:https://doi.org/10.1016/j.renene.2016.07.048

Zhao, F., & Virkar, A. V. (2005). Dependence of polarization in anode-supported solid oxide fuel cells on various cell parameters. *Journal of Power Sources, 141*(1), 79-95. doi:10.1016/j.jpowsour.2004.08.057

จุฬาลงกรณ์มหาวิทยาลัย

CHULALONGKORN UNIVERSITY

APPENDICES

APPENDIX A.
RELATIVE GAIN ARRAY (RGA)

The relative gain array (RGA) is considered a controllability index for the selection of input-output pairings, to describe the interactions among inputs and outputs, and to determine the optimal control structure of multi input multiple output (MIMO).

The RGA of a non-singular square complex matrix (G) is defined as indicated in Equation (A.1), where x denotes element by element multiplication (the Hadamard or Schur product).

$$RGA(G) = \Lambda(G) = G \times \left(G^{-1}\right)^{T} \tag{A.1}$$

The RGA of a transfer matrix is generally computed as a function of frequency. For a 2x2 matrix with elements g_{ij}, the RGA can be shown as:

$$\Lambda(G) = \begin{bmatrix} \lambda_{11} & \lambda_{12} \\ \lambda_{21} & \lambda_{22} \end{bmatrix}; \quad \lambda_{11} = \cfrac{1}{1 - \cfrac{g_{12}g_{21}}{g_{11}g_{22}}} \tag{A.2}$$

Using RGA as an interaction measure was originally performed by Bristol (1966). Let u_j and y_i denote a particular input-output pair for multivariable plant $G(s)$, and the task is to use u_j to control y_i. He argued that there will be two extreme cases:

- All other loops open: $u_k = 0, \forall k \neq j$

- All other loops closed with perfect control: $y_k = 0, \forall k \neq i$

Thus, gain $\partial y_i / \partial u_j$ for two extreme cases:

$$\text{Other loop open:} \left(\frac{\partial y_i}{\partial u_j} \right)_{u_k = 0, k \neq j} = g_{ij} = \left[G \right]_{ij} \tag{A.3}$$

$$\text{Other loop closed:} \left(\frac{\partial y_i}{\partial u_j} \right)_{y_k = 0, k \neq i} \triangleq g_{ij} = 1 \Big/ \left[G^{-1} \right]_{ji} \tag{A.4}$$

where g_{ij} is the ij' th element of G and g_{ij} is the inverse of the ji' th element of G^{-1}. They can be derived as following:

When $y = Gu$; $\quad \left(\dfrac{\partial y_i}{\partial u_j} \right)_{u_k = 0, k \neq j} = [G]_{ij}$ (A.5)

Then, interchange the role of G and G^{-1}, of u and y, and of i and j to get

$u = G^{-1}y$; $\quad \left(\dfrac{\partial u_j}{\partial y_i} \right)_{y_k = 0, k \neq i} = \left[G^{-1} \right]_{ji}$ (A.6)

Hence, Equation (A.4) follows. Bristrol defined the ratio between the gain in (A.3) and (A.4) as the ij' th relative gain as following:

$\lambda_{ij} \triangleq \dfrac{g_{ij}}{g_{ij}} = [G]_{ij}[G^{-1}]_{ji}$ (A.7)

When the relative gain element λ_{ij} is close to 1, it means that the gain from u_j to y_i is unaffected by closing the other loops. It thus leads to pairing rule, select the pairings of input-output with the RGA elements close to 1. However, the pairing with negative RGA elements should be avoid because of instability with integral action in the loop. In addition, large RGA elements (typical 5-10 or larger) should not be selected because the plant is fundamentally difficult to be controlled.

จุฬาลงกรณ์มหาวิทยาลัย

CHULALONGKORN UNIVERSITY

APPENDIX B.

SKOGESTAD'S IMC (SIMC) PID TUNING

The cascade (series) PID controller as shown in Equation (B.1) is used by the reason of PID rules with derivative action are simpler and the corresponding settings for the ideal (parallel) PID controller are easily obtained[1] but the reverse translation is not always possible (Skogestad, 2003). Figure B. 1 shows the block diagram of feedback control system.
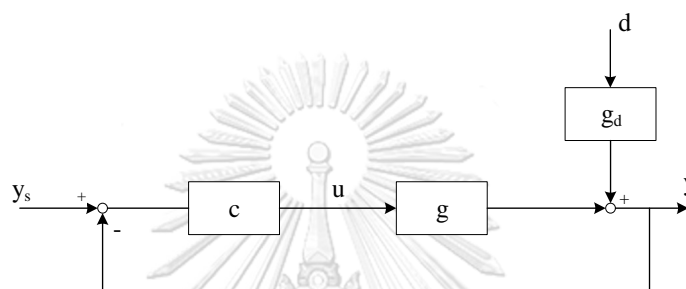

Figure B. 1 Block diagram of feedback control system

Cascade PID: $c(s) = K_c \left(\dfrac{\tau_I s + 1}{\tau_I s} \right) (\tau_D s + 1) = \dfrac{K_c}{\tau_I s} \left(\tau_I \tau_D s^2 + (\tau_I + \tau_D) s + 1 \right)$ (B.1)

where K_c is the controller gain, τ_I is the integral time, and τ_D is the derivative time.

The first step is approximate the second-order time delay model g(s) from the original model $g_0(s)$ using half rule:

From $g_0(s) = \dfrac{k \prod_j \left(-T_{j0}^{inv} s + 1 \right)}{\prod_i (\tau_{i0} s + 1)} e^{-\theta_0 s}$ (B.2)

To $g(s) = \dfrac{k}{(\tau_1 s + 1)(\tau_2 s + 1)} e^{-\theta s}$ (B.3)

Where the lags τ_{i0} are ordered according to their magnitude, $T_{j0}^{inv} > 0$ denote the inverse response time constants corresponding to the RHP-zeros located at $s = z_{j0}$,

---

[1] Translation to Ideal PID form: $c'(s) = K'_c \left(1 + \dfrac{1}{\tau'_I s} + \tau'_D s \right)$ using $K'_c = K_c \alpha$, $\tau'_I = \tau_I \alpha$, $\tau'_D = \tau_D / \alpha$, and $\alpha = 1 + \tau_D / \tau_I$

k is the plant gain, θ is the effective time delay, τ_1 is the dominant lag time constant, and τ_2 is the second-order lag time constant (optional).

To obtain second-order model Equation (B.3), following approximations are applied:

$$\tau_1 = \tau_{10}; \quad \tau_2 = \tau_{20} + \tau_{30}/2; \quad \theta = \theta_0 + \tau_{30}/2 + \sum_{i \geq 4} \tau_{i0} + \sum_j T_{j0}^{inv} \tag{B.4}$$

The recommended SIMC PID setting are

$$K_c = \frac{1}{k} \frac{\tau_1}{\tau_c + \theta} \tag{B.5}$$

$$\tau_I = \min \left\{ \tau_1, 4(\tau_c + \theta) \right\} \tag{B.6}$$

$$\tau_D = \tau_2 \tag{B.7}$$

Here τ_c is the only tuning parameter. In this thesis, active constrains are controlled which require tight control ($\tau_c = \theta$).

The recommendation (B.5) and (B.6) can be applied for PI setting ($\tau_D = 0$). It is however the approximations (B.4) are changed to

$$\tau_1 = \tau_{10} + \tau_{20}/2; \quad \theta = \theta_0 + \tau_{20}/2 + \sum_{i \geq 3} \tau_{i0} + \sum_j T_{j0}^{inv} \tag{B.8}$$

APPENDIX C.
LIST OF PUBLICATIONS

International publications

1. **Jienkulsawad, P.**, and A. Arpornwichanop. 2016. 'Investigating the performance of a solid oxide fuel cell and a molten carbonate fuel cell combined system', Energy, 107: 843-53.

2. **Jienkulsawad, P.**, S. Skogestad, and A. Arpornwichanop. 2017. 'Control structure design of a solid oxide fuel cell and a molten carbonate fuel cell integrated system: Top-down analysis', Energy Conversion and Management, 152: 88-98.

3. **Jienkulsawad, P.**, D. Saebea, Y. Patcharavorachot, S. Kheawhom, and A. Arpornwichanop. 2018. 'Analysis of a solid oxide fuel cell and a molten carbonate fuel cell integrated system with different configurations', International Journal of Hydrogen Energy, 43: 932-42.

International conferences

1. **Jienkulsawad, P.**, D. Saebea, Y. Patcharavorachot, and A. Arpornwichanop. 2015. 'Design of the integrated solid oxide fuel cell and molten carbonate fuel cell system to reduce carbon dioxide emissions', 12th International Conference on Chemical & Process Engineering (ICheaP-12 Conference), 19 – 22 May 2015, Milan, Italy

2. **Jienkulsawad, P.**, D. Saebea, Y. Patcharavorachot, and A. Arpornwichanop. 2016. 'Performance Analysis of the Solid Oxide Fuel Cell and Molten Carbonate Fuel Cell Combined System', 23rd International Symposium on Chemicla Reaction Energineering 7th Asia-Pacific Chemical Reaction Engineering Symposium (ISCRE 23 & APCRE 7), 7-10 September 2014, Bangkok, Thailand.

3. **Jienkulsawad, P.**, S. Skogestad, and A. Arpornwichanop. 2017. 'Control of the integrated solid oxide fuel cell and molten carbonate fuel cell', the 2nd International Conference on Alternative Fuels and Energy (ICAFE 2017), 23 - 25 October 2017, Daegu, South Korea.

4. **Jienkulsawad, P.**, and A. Arpornwichanop. 2018. 'Design of the compressed air energy storage in the hybrid SOFC-MCFC-GT system', 10th International Conference on Applied Energy (ICAE2018), 22-25 August 2018, Hong Kong, China.

National conference

Jienkulsawad, P., and A. Arpornwichanop. 2016. 'Design of Hybrid SOFC-MCFC-GT System with Compressed Air Energy Storage for Normal and Peak Load', The Eighteenth RGJ-Ph.D. Congress (RGJ-Ph.D. Congress 18), 8-10 June 2017, Nonthaburi, Thailand.

VITA

NAME   Prathak Jienkulsawad

DATE OF BIRTH   1st February 1989

PLACE OF BIRTH   Songkhla, Thailand

INSTITUTIONS ATTENDED   2011-present: Graduate studies in Control and Systems Engineering Research Center, Department of Chemical Engineering, Faculty of Engineering, Chulalongkorn University.

2015-2016: Joined 11 months of research in Department of Chemical Engineering, Norwegian University of Science and Technology (NTNU), Norway

2007-2010: Bachelor of Engineering Degree (with first-class honors) in Chemical Engineering from Prince of Songkla University.

จุฬาลงกรณ์มหาวิทยาลัย

CHULALONGKORN UNIVERSITY